DYNAMICS OF KICKED LASER COOLED RUBIDIUM ATOMS

By

BRIAN P. TIMMONS

Bachelor of Science
Northeastern State University
Tahlequah, Oklahoma
2000

Submitted to the Faculty of the
Graduate College of the
Oklahoma State University
in partial fulfillment of
the requirements for
the Degree of
DOCTOR OF PHILOSOPHY
July, 2006

DYNAMICS OF KICKED LASER COOLED
RUBIDIUM ATOMS

Thesis Approved:

Dr. Gil Summy
Thesis Advisor

Dr. Paul Westhaus

Dr. Al Rosenberger

Dr. Dan Grischkowsky

Dr. A. Gordon Emslie
Dean of the Graduate College

ACKNOWLEDGMENTS

I would like to thank my advisor Dr. Gil Summy for his technical expertise. His encouragement and belief in me has helped develop my skills as a scientist grow everyday. I would like to thank Dr. Paul Westhaus for providing me the opportunity to achieve my goals at OSU.

I would like to acknowledge my committee members, Dr. G. Summy, Dr. P. Westhaus, Dr. A.T. Rosenberger, and Dr. D. Grischkowsky for their help and guidance.

The physics faculty has been very supportive throughout my 6 years at OSU. I thank them for providing the time and knowledge on teaching me the theoretical skills necessary on becoming a physicist.

The physics office staff, Susan, Cindy, and Stephanie, deserve a huge thank you for delivering a relatively stress free work enviornment. Thank you to Mike and Larry in the machine shop for making the necessary equipment and for allowing me to use the machine shop.

I would like to thank my colleague's Peyman, Ghazal, and Vijay for making the basement a fun place to work. Peyman's unreachable wealth of knowledge has provided me with a human text book, which will sadly be missed. It was a pleasure working in the BEC Lab.

All of the graduate students who have been a part of my stay at OSU, I thank them for the help and support. I would like to thank Mahmudur Rahman, a fellow graduate student and a personal friend, for the financial and moral support.

I would like to thank my mother and father for the love and support they have given me throughout the years. I especially want to thank my wife and daughter,

without them none of this would be possible. Their love and support has guided me to places I never thought were reachable.

TABLE OF CONTENTS

LIST OF FIGURES

CHAPTER 1

INTRODUCTION

1.1 Overview

The idea of wave-particle duality has been in existence for centuries. In the 1600's, a major contributor to the wave nature of light was Christiaan Huygens through his manuscript "Treatise on Light". This work explained light as a wave propagating in the *ether* and derived formulas for reflection and refraction[1]. Around the same time, Isaac Newton developed a theory that light was made up of discrete particles called "corpusculs"[2]. Due to Newton's fame, "The Corpuscular Theory" was the belief until the early 1800's. In 1801 Thomas Young performed experiments with light entering a double slit which produced an interference pattern[3]. These experiments verified the theories of Huygens, that light was a wave. A century later, Einstein explained the photoelectric effect, where a metallic object was exposed to photons at a certain threshold frequency. This caused electrons to be ejected from the object and produced a current.[4]. In Einstein's theory the energy of a photon was related to its frequency, ν, by $E = h\nu$, where h was Planck's constant. Einstein was awarded the Nobel Prize for the details of the photoelectric effect in 1921. Three years later deBroglie hypothesized that all matter could be treated as a wave with wavelength[5],

$$\lambda = \frac{h}{p}, \tag{1.1}$$

where p is the momentum of the matter. The wave nature of particles was observed in 1927 by Davisson and Germer[6] using electron diffraction from a single nickel crystal.

This was experimental verification that wave-particle duality included matter as well as light.

In 1933 Kapitza and Dirac predicted that electrons could be diffracted by a standing light wave[7]. Later, in 1966 Altshuler[8] extended the idea to include any particle with the ability to scatter photons, even neutral atoms. Using the ideas of Kapitza and Dirac and the wave nature of particles, this type of interaction was first observed in 1983 using a sodium atomic beam sent through a near-resonant standing wave[9,10]. These experiments were performed with fast atoms (velocities $\sim 10^3$cm/s) and consequently, the diffracted angles were very small. Instead of using high velocity atomic beams, atoms could be slowed down by having their temperature lowered. This would increase both the flux of atoms available for diffraction as well as the diffraction angles.

The idea of laser cooling atoms was introduced in 1975 by Hänsch and Schawlow[11]. Atoms moving in a near-resonant standing wave light field would (depending on their direction of motion) see the light frequency Doppler shifted closer or further away from resonance. When the light frequency was tuned slightly below resonance, atoms would absorb photons propagating in a direction opposite to their motion. Subsequently the atoms would emit photons in random directions. Over many cycles, the atom would feel a pressure in the direction of the absorbed photon. The first observation of this was in 1985 by S. Chu[12] *et al.* and was given the name "Optical Molasses" (due to the atoms being in a viscous "fluid" of photons). A spatially dependent force could also be realized in a modified version of the optical molasses by applying a linear inhomogeneous magnetic field to atoms with several Zeeman sublevels. If the laser light was detuned below an atomic resonance, the light interacted with the atoms such that it pushed them towards where the magnetic field was zero. The combination of the laser light pressure and the inhomogeneous magnetic field led to the first observation of the magneto-optical trap (MOT) in 1987 by Raab[13] *et al.*

The advent of laser cooling and trapping of atoms has led to the creation of new fields of physics such as nano-fabrication (atom lithography[14]), and atom interferometers[15] (atoms optics) and has given researchers tools to carry out precise measurements of fundamental physical constants. Also, a new form of matter, a Bose-Einstein Condensate (BEC), was observed[16–18] opening up entirely new avenues of investigation.

The ability to manipulate laser cooled atoms is of great interest in developing atom lasers[19], atom interferometers[15], and for studying quantum chaos[20]. This thesis presents details of an experiment for transferring large amounts of momentum to a sample of laser cooled neutral atoms. A source of cold atoms was created using a MOT. The cold atoms were subjected to short pulses by an off-resonant standing wave of light[10,21] in the vertical direction. Treating the atoms as atomic deBroglie waves, it was possible to see the standing wave potential as a thin phase grating which diffracted the atom into a series of momentum states. With the proper initial conditions, atoms could receive a gain in momentum each time a pulse of this grating was applied. A linear increase in momentum of some of the atoms with each pulse defined a quantum accelerator mode[22] (QAM). The classical dynamics of this system were quite similar to the δ-kicked rotor[23], but the quantum dynamics were markedly different near the primary quantum resonances[24]. These resonances occurred at half-integer multiples of the Talbot time[22] and represent a ballistic growth with a quadratic increase in kinetic energy of the atoms. Gravity introduced an additional phase to the atoms in between the pulses, a necessity for obtaining QAM's. The initial velocities of the atoms needed to be on the order of a recoil velocity from a photon in the standing wave. Laser cooling was required to slow the atoms down to meet this condition. Although the QAM's are a beautiful demonstration of fundamental quantum mechanics, they may also provide some of the tools necessary to build an atom beamsplitter and ultimately an atom interferometer.

1.2 Outline of Thesis

This section will give an overview of the organization of my thesis. Since it was necessary to establish a detailed theoretical background before experimenting on laser cooled atoms, in Chapter 2, the theory necessary to understand laser cooling and trapping of neutral atoms is developed. This is achieved by first defining an optical force on an atom in order to cool the atoms. Then, by applying a linear inhomogeneous magnetic field to the system under study, it is shown how a MOT can be formed. Chapter 2 also covers the theory for QAMs. A phase model[25] is introduced, which relies on the phase evolution of an atom between each pulse. Then we move to an ϵ-classical theory[22] which is able to describe higher order accelerator modes. In both cases, a momentum equation is derived which will be compared to the experimental data in Chapter 4.

A vacuum system was needed to minimize the collision of background gases with the rubidium atoms. The lasers, acousto-optical modulators (AOM), waveplates, and many more components were part of the optical system to provide the proper frequencies and polarizations of light. All of these component are discussed in Chapter 3. Appendix A gives details of the amount of programming code required to perform the experiments.

The kicking experiments we have performed using laser cooled atoms are presented in Chapter 4. By applying an off-resonant standing wave of light in pulses separated by near integer multiples of the half-Talbot time, some of the laser cooled atoms could receive a linear gain in momentum with each pulse. This is the signature of QAMs. The observation of quantum accelerator modes (QAM) and a comparison to previous experiments[26] with a different atomic species will be presented. It will be seen that the experimental data agrees with the theory presented in Chapter 2, although there are some significant differences between QAMs in rubidium and cesium.

In particular new dynamics were seen away from the quantum resonances at half-integer multiples of the Talbot time. This was an important observation since much of the recent work on quantum chaos has *only* concentrated on understanding the behavior of systems near such primary resonances. Other higher order resonances have just started to be investigated in the δ-kicked rotor[27]. These results have only touched the surface of the intricate dynamics of the higher order resonances. We expect that the new QAM dynamics seen in our experiments are also the result of higher order quantum resonances. Normally, QAMs are asymptotically centered around the primary resonances, but our observations include resonances centered far from the primary resonances. Furthermore, the detailed theory (ϵ-classical) is only capable of treating QAMs that occur near the primary quantum resonances. Thus there is a wide discrepancy between our results and theoretical predictions. A recent publication by Bach[28] *et al.* gives some theoretical insight to this new type of QAM dynamics, although this work is still very preliminary. It is anticipated that our results will give impetus for further developments to theory.

The thesis concludes with a summary of the main achievements of this work and some suggestions for the future directions of the research. Appendix B contains my publications[17,18] which were performed on the BEC chamber.

CHAPTER 2

OPTICAL FORCES ON ATOMS: FROM LASER COOLING TO QUANTUM ACCELERATOR MODES

The first part of this chapter covers the theory of a magneto-optical trap (MOT). A MOT, as the name implies, has a magnetic component and an optical component. The optical component uses an optical force to cool down the atoms. This force arises due to the induced dipole moment on the atom from the spatially varying light field. With the light frequency near the atomic transition of the atom, the absorption of light in one direction, followed by spontaneous emission in random directions, averages to a net force in the direction of the light. If the atom has an internal structure with several Zeeman magnetic substates, the application of a linear, inhomogeneous magnetic field can produce a spatially dependent force. The combination of the optical force and the magnetic field induced Zeeman shift allows for the trapping of atoms in a MOT. Atoms trapped in a MOT give us a source of cold atoms for experiments.

The theory for quantum accelerator modes (QAM) is presented in the second part of the chapter. A phase model for QAM's from Godun[25] is discussed as well as an ϵ-classical theory[22]. The phase model looks at the phase evolution of the atoms from pulse-to-pulse and leads to the derivation of an equation describing the momentum of the QAM's. This model works well, but fails to explain higher order QAM's[29]. The ϵ-classical theory also provides a method of calculating the momentum of the high order QAM's, but this theory can be used under a wider range of circumstances.

2.1 Light Force on a Two Level Atom

In general, a force is defined as the expectation value of the quantum mechanical force operator,

$$\hat{F} = -\frac{\partial \hat{H}}{\partial z}. \tag{2.1}$$

where $\hat{H}$ is the total Hamiltonian of the system. Taking the expectation value of $\hat{F}$ gives,

$$< \hat{F} >= \mathrm{Tr}(\hat{\rho}\hat{F}), \tag{2.2}$$

where $\hat{\rho}$ is the density matrix, and its time evolution is given by,

$$\frac{d\hat{\rho}}{dt} = -\frac{i}{\hbar}[\hat{H}, \hat{\rho}]. \tag{2.3}$$

To calculate the force in our particular case we first need to see what interactions are involved with an atom in a light field. We can write the Hamiltonian, $\hat{H}$, for our system as the sum of a field-free time independent operator, $\hat{H}_0$ and a time dependent radiation field operator, $\hat{H}'(t)$. Thus

$$\hat{H}(t) = \hat{H}_0 + \hat{H}'(t). \tag{2.4}$$

where the $\hat{H}_0$ operator has eigenvalues $E_n = \hbar\omega_n$ and eigenfunctions ϕ_n. So, $\hat{H}_0\phi_n(\vec{r}) = E_n\phi_n(\vec{r})$ and the eigenfunctions are linearly independent and form a complete set. Therefore, the solution for the time dependent Schrödinger equation $\hat{H}\psi(\vec{r},t) = i\hbar\frac{\partial\psi(\vec{r},t)}{\partial t}$ can be expanded in terms of $\phi_n(\vec{r})$

$$\hat{H}(t)\Psi(\vec{r},t) = [\hat{H}_0 + \hat{H}'(t)]\sum_k c_k(t)\phi_k(\vec{r}). \tag{2.5}$$

Applying this solution to the Schrödinger equation, multiplying by $\phi_j^*(\vec{r})$, and integrating over spatial coordinates $(\vec{r})$ one arrives at,

$$i\hbar\frac{dc_j(t)}{dt} = c_j(t)E_j + \sum_k c_k(t)\hat{H}'_{jk}(t), \tag{2.6}$$

where$\hat{H}'_{jk}(t) \equiv \langle\phi_j|\hat{H}'(t)|\phi_k\rangle$. For a two level atom, the sum in Eq. (2.6) is just two terms, a ground state term and an excited state term labeled g and e, respectively.

This problem is known as the *Rabi Two-Level Problem*[30]. This leads to two coupled differential equations.

$$i\hbar\frac{dc_g(t)}{dt} = c_g(t)(E_g + \hat{H}'_{gg}) + c_e(t)\hat{H}'_{ge}(t), \tag{2.7}$$

$$i\hbar\frac{dc_e(t)}{dt} = c_e(t)(E_e + \hat{H}'_{ee}(t)) + c_g(t)\hat{H}'_{eg}(t), \tag{2.8}$$

where $\hat{H}'_{ge} = \hat{H}'^{*}_{eg}$.

We would now like to evaluate the interaction term, $\hat{H}'_{eg}(t)$. We can use the fact that a spatially varying electric field induces a dipole moment on the atom. Then the interaction term becomes[31],

$$\hat{H}'_{eg}(t) = -\mu\mathcal{E}(\vec{r}, t) \tag{2.9}$$

where $\mathcal{E}(\vec{r}, t)$ is the electric field and $\mu = q\langle e|\vec{\epsilon}\cdot\vec{\mathrm{r}}|g\rangle$, is the induced dipole moment in the direction of $\mathcal{E}(\vec{r}, t)$ of an electron with charge q at position $\vec{r}$, and $\vec{\epsilon}$ is the light polarization unit vector. For our two-level atom, the dipole moment is parallel to the polarization $\hat{\epsilon}$. A discussion on the light's polarization will be given later. Due to the odd parity of $\hat{H}'$ only opposite parity atomic states can couple through the dipole interaction. Therefore, this sets the matrix elements $\hat{H}'_{gg}(t)$ and $\hat{H}'_{ee}(t)$ to zero. Also, we can set $E_g = 0$ which implies $\omega_g = 0$ and $\omega_a = \omega_e$. Then Eqs. (2.7) and (2.8) become

$$i\hbar\frac{dc_g(t)}{dt} = -c_e(t)\mu\mathcal{E}(\vec{r}, t), \tag{2.10}$$

and

$$i\hbar\frac{dc_e(t)}{dt} = c_e(t)\hbar\omega_e - c_g(t)\mu\mathcal{E}(\vec{r}, t). \tag{2.11}$$

Now we can get the final Hamiltonian from Eq. (2.4) by forming a matrix of the c coefficients. The result is

$$\hat{H} = \begin{pmatrix} 0 & -\mu\mathcal{E}^*(\vec{r}, t) \\ -\mu\mathcal{E}(\vec{r}, t) & \hbar\omega_e \end{pmatrix}, \tag{2.12}$$

This matrix is also used in developing the force on the atoms in the off-resonant standing wave in the next section. Now that we have the total Hamiltonian for the

system, we can find the force in Eq. (2.1). But first let us apply Eq. (2.12) to Eq. (2.3) and find the time evolution of the density operator. This gives,

$$\begin{pmatrix} \dot{\rho}_{gg} & \dot{\rho}^*_{eg} \\ \dot{\rho}_{eg} & \dot{\rho}_{ee} \end{pmatrix} = i \begin{pmatrix} \Omega^*(\vec{r},t)\rho_{eg} - \Omega(\vec{r},t)\rho^*_{eg} & \omega_e\rho^*_{eg} - \Omega^*(\vec{r},t)w \\ -\omega_e\rho_{eg} + \Omega(\vec{r},t)w & -\Omega^*(\vec{r},t)\rho_{eg} + \Omega(\vec{r},t)\rho^*_{eg} \end{pmatrix}, \quad (2.13)$$

where $\rho_{ge} = \rho^*_{eg}$, $w = (\rho_{gg} - \rho_{ee})$ is the population difference, and $\Omega(\vec{r},t) = \mu\mathcal{E}(\vec{r},t)/\hbar$ is the Rabi frequency. Using population conservation, $\rho_{ee} + \rho_{gg} = 1$, we can reduce Eq. (2.13) to

$$\dot{\rho}_{eg} = -\frac{\gamma}{2}\rho_{eg} - i\omega_e\rho_{eg} + i\Omega(\vec{r},t)w \quad (2.14)$$

and

$$\dot{w} = \gamma(1-w) + i2(\Omega^*(\vec{r},t)\rho_{eg} - \Omega(\vec{r},t)\rho^*_{eg}) \quad (2.15)$$

where γ is the spontaneous emission rate (see Metcalf [32]). From here we can apply a form for the electric field in $\Omega(\vec{r},t)$ such that it has a spatial part and a time dependant harmonic part. That is,

$$\mathcal{E}(\vec{r},t) = \mathcal{E}(\vec{r})\cos(\omega_l t) = \frac{\mathcal{E}(\vec{r})}{2}(e^{i\omega_l t} + e^{-i\omega_l t}), \quad (2.16)$$

where ω_l is the on resonant laser frequency. As mentioned before, the force is from photon absorption followed by spontaneous emission. With no electric field, Eq. 2.14 would have slowly varying solutions with $\omega_l \approx \omega_e$. Thus, a transformation to remove the time oscillations of Eqs. (2.14) and (2.15) can be written as

$$\rho_{eg} = \sigma_{eg}e^{-i\omega_l t} \quad (2.17)$$
$$\rho^*_{eg} = \sigma^*_{eg}e^{i\omega_l t}.$$

Substituting Eq. (2.16) into Eqs. (2.14) and (2.15) and applying the transformation, the result is

$$\dot{\sigma_{eg}} = (-\frac{\gamma}{2} + i\delta)\sigma_{eg} + \frac{iw\Omega(\vec{r})}{2} \quad (2.18)$$

and

$$\dot{w} = \gamma(1-w) + i(\Omega^*(\vec{r})\sigma_{eg} - \Omega(\vec{r})\sigma^*_{eg}), \quad (2.19)$$

where $\delta = \omega_l - \omega_e$ is the laser frequency detuning from the atomic resonance. The rotating wave approximation[33] (RWA), which neglects terms oscillating at $2\omega_l$, as well as the conservation of the population was used to find Eqs. (2.18) and (2.19). We find the steady state solutions of Eqs. (2.18) and (2.19) by setting their respective time derivatives to zero. After manipulation, we get

$$\sigma_{eg} = \frac{2\Omega(-\delta + i\frac{\gamma}{2})}{\gamma^2(1 + (\frac{2\delta}{\gamma})^2 + 2\frac{\Omega^2}{\gamma^2})} \tag{2.20}$$

and

$$w = \frac{1 + (\frac{2\delta}{\gamma})^2}{1 + (\frac{2\delta}{\gamma})^2 + 4\frac{\Omega^2}{\gamma^2}}, \tag{2.21}$$

where $\Omega = \Omega(\vec{r}) = \mu\mathcal{E}(\vec{r})/\hbar$ is the Rabi frequency. Using the conservation of population in Eq. (2.21), we can find the individual populations of ρ_{ee} and ρ_{gg}. Here we can use a special case of a traveling wave in the z-direction for the electric field $\mathcal{E}(\vec{r})$. Using

$$\mathcal{E}(z) = \mathcal{E}_0 \cos(kz - \omega_l t) = \frac{\mathcal{E}_0}{2}(e^{i(kz-\omega_l t)} + c.c) \tag{2.22}$$

in Eq. (2.12) and substituting into Eq. (2.1), the result for the force operator is

$$\hat{F} = \begin{pmatrix} 0 & \mu\frac{\partial\mathcal{E}^*(z)}{\partial z} \\ \mu\frac{\partial\mathcal{E}(z)}{\partial z} & 0 \end{pmatrix}, \tag{2.23}$$

Now we are ready to find the force on an atom in a traveling wave light field. Using Eq. (2.2) to get $F = Tr(\hat{\rho}\hat{F}) = \mu\frac{\partial\mathcal{E}}{\partial z}\sigma^*_{eg}e^{i\omega_l t} + \mu\frac{\partial\mathcal{E}^*}{\partial z}\sigma_{eg}e^{-i\omega_l t}$. After substitution of Eqs. (2.20) and (2.22) and applying the RWA the force becomes

$$F = \frac{\hbar k\gamma s}{2(1 + (\frac{2\delta}{\gamma})^2 + s)}, \tag{2.24}$$

where $s = 2\Omega^2/\gamma^2 = I/I_0$ is the on-resonant saturation parameter defining the ratio of laser light intensity, I, to saturation intensity, I_0. Now we have the spontaneous force on a stationary atom. We can see that $\hbar k$ is the momentum of the absorbed photon, γ is the rate of spontaneous emission, and the other factor is the upper state population, ρ_{ee}. Since the emission process is averaged over many cycles, the net average force would be in the direction of the absorbed photon.

Now we can expand the possibilities of Eq. (2.24) to moving atoms. An atom moving in the direction of propagation of the light field would see a Doppler shift in the frequency of $-kv$. Thus, the atom would see the light detuned by $\delta - kv$. An opposite effect for an atom moving against the light field would occur so that it would see the detuning as $\delta + kv$. We can write the force equation for a moving atom as

$$F_{\pm} = \pm \frac{\hbar k \gamma s}{2(1 + (\frac{2(\delta \mp kv}{\gamma})^2 + s)}, \tag{2.25}$$

where the plus (minus) sign refers to the force on the atom moving with (against) the light field. A MOT contains counterpropagating beams so we can generalize the force on a moving atom in this situation as $F = F_+ + F_-$. The result is a velocity dependent force $F = -\beta v$, where β is a damping coefficient given by

$$\beta = \frac{8\hbar k^2 s \delta}{\gamma(1 + (\frac{2(\delta - kv)}{\gamma})^2 + s)(1 + (\frac{2(\delta + kv)}{\gamma})^2 + s)}. \tag{2.26}$$

This is a damping force because $m\dot{v} = -\beta v$ has solutions $v = v_0 e^{-(\beta/m)t}$. Thus, with light detuned below resonance, $\delta < 0$, atoms moving toward the laser beam see the light Doppler shifted closer to resonance. For the counterpropagating beam the light is shifted further out of resonance. Therefore, atoms moving against the light scatter more photons and their velocity will be decreased. Ultimately a large negative detuning or positive velocity results in a large dissipative force. This is important during the final cooling phase of the experiment where we set the detuning to be much larger than is typically used to trap atoms in the MOT. Now we have found the force on the atoms in a standing light wave, it should be possible to extend this analysis to three orthogonal directions so that atoms can be slowed no matter the direction of their velocity. This 3-dimensional (3D) cooling was done by Chu and co-workers[12] and was given the name optical molasses (OM) to describe the atoms being in a viscous fluid of photons. With this damping force, one would think of obtaining a velocity of zero and violating the third law of thermodynamics. Of course, this can not be true so there are limits to which atoms can be cooled using laser light. A

Doppler temperature, T_D, corresponding to the energy associated with the natural linewidth of the cooling transition, γ, arises from the heating due to the recoil effect from the absorption and emission process. We look at the rate of the kinetic energy lost from the atom due to the damping force and the rate of kinetic energy gained by the recoil effect. For the kinetic energy loss rate, we have

$$\dot{E}_{loss} = Fv = \frac{8\hbar k^2 s\delta v^2}{\gamma(1+(\frac{2\delta}{\gamma})^2)^2}. \tag{2.27}$$

The atomic momentum changes by $\hbar k$ during the process and leads to an average kinetic energy change by at least the recoil energy, $E_r = (\hbar k)^2/2m$. This energy change occurs at a rate of $2\gamma\rho_{ee}$, where the 2 factor accounts for the use of two beams and ρ_{ee} is found from Eq. (2.21) using the conservation of population. Taking the product of kinetic energy gained and the rate gives,

$$\dot{E}_{gain} = \frac{\gamma(\hbar k)^2 s}{m(1+(\frac{2\delta}{\gamma})^2)} \tag{2.28}$$

In steady state Eqs. (2.27) and (2.28) are equal so that a value for the velocity squared can be obtained. Hence,

$$v^2 = \frac{\hbar\gamma^2(1+(\frac{2\delta}{\gamma})^2)}{8m\delta} \tag{2.29}$$

Substituting Eq. (2.29) into $k_B T = mv^2$ a temperature can be found,

$$T = \frac{\hbar\gamma^2(1+(\frac{2\delta}{\gamma})^2)}{8k_B\delta}. \tag{2.30}$$

This temperature has a minimum at $2\delta/\gamma = 1$ which leads to the Doppler temperature limit,

$$T_D = \frac{\hbar\gamma}{2k_B} \tag{2.31}$$

The Doppler limit is about 140 μK for rubidium 87. Surprisingly, the initial laser cooling experiments produced temperatures considerably lower than was thought to be possible from the theory of the Doppler temperature. The first observation of laser cooling below the Doppler limit was made by Lett[34] using a different method[35] than what was proposed[36,37] at the time. In fact, a lower limit than the Doppler limit is the

so-called recoil limit. The recoil limit is associated with the emission or absorption of a single recoil photon from an atom. Thereby, the atom receives a recoil velocity $v_r = \hbar k/m$, where m is the atoms mass. The recoil temperature, T_r, is given by

$$k_B T_r = \frac{\hbar^2 k^2}{m} \tag{2.32}$$

The recoil temperature for rubidium 87 is 400 nK.

2.2 Magneto-optic Trap

The previous section detailed a method of cooling a sample of neutral atoms using laser light. Now the method used to produce a magneto-optic trap (MOT) to collect the cold atoms will be discussed. A MOT is formed by placing the slowly moving atoms in a linear inhomogeneous magnetic field. For simplicity, consider atomic transitions where $J_g = 0$ and $J_e = 1$ so that the transition will split into three Zeeman components in the magnetic field. Figure 2.1 shows two counterpropagating opposite circularly polarized, $\sigma_+ - \sigma_-$ configuration[38], laser beams detuned below the atomic resonance and the Zeeman sub-levels. Due to the Zeeman shift, for a positive magnetic field the $M_e = +1$ state is shifted up and the $M_g = -1$ is shifted down. Therefore an atom at position z in Figure 2.1 will be pushed toward the center of the trap by scattering more light from the σ^- beam. A force in the opposite direction occurs with a negative magnetic field, that is on the left side of Fig. 2.1.

2.3 Quantum Accelerator Mode Theory

We want to subject the laser cooled rubidium 87 atoms to pulses of a standing wave of off-resonant light. The standing wave has a spatially varying intensity, and consequently the atom-field interaction energy depends upon the position. When the standing wave is turned on, atoms can have their momentum changed due to the gradient in this energy. With an additional gravitational potential and the right initial conditions (pulse period and initial velocity of the atoms) the atoms can be

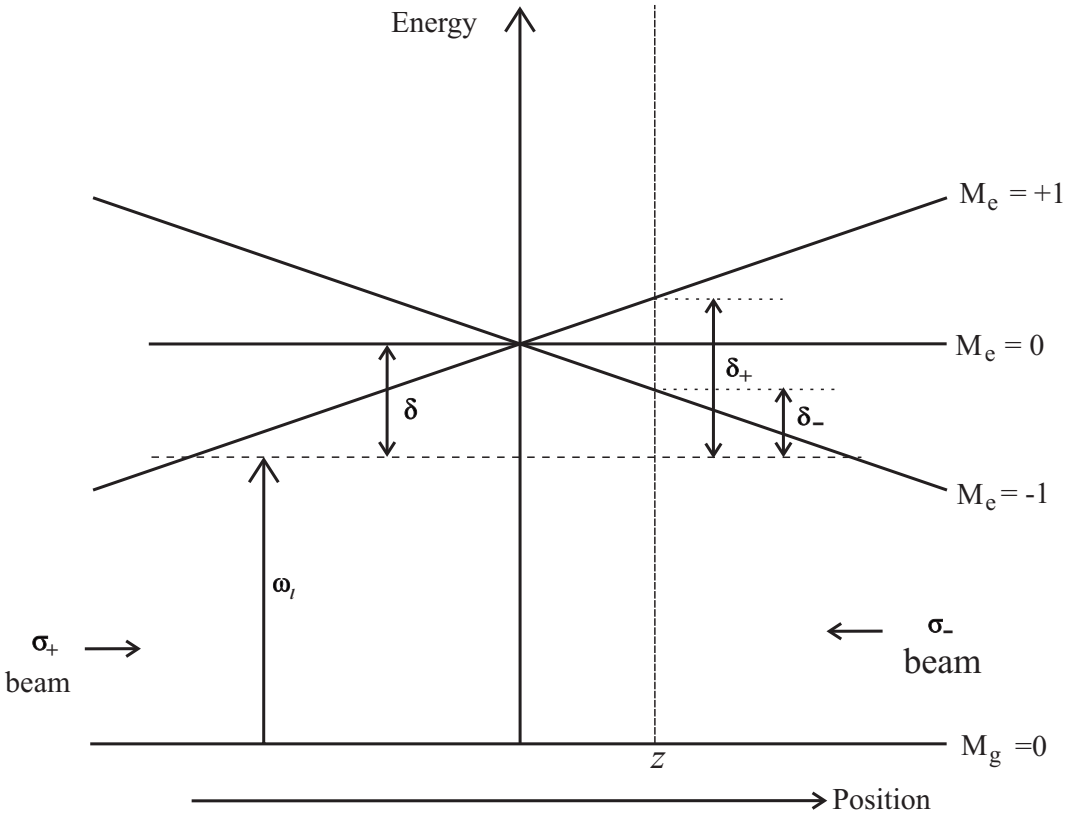

Figure 2.1. A one-dimensional (1D) MOT scheme. Where the horizontal dashed line is the laser frequency seen by a stationary atom in the center of the trap (i.e. where B=0).

given the same gain in momentum with each pulse. For such a case, a linear increase in the momentum of the atoms is seen and the atoms are in what is known as an accelerator mode[22]. We now examine this situation in detail.

The Hamiltonian for the system described above is given by

$$\hat{H} = \frac{\hat{p}^2}{2m} + mg\hat{x} - \frac{U_{max}}{2}[1 + \cos(G\hat{x})] \sum_{N_p} \delta(t - N_p T), \tag{2.33}$$

where m is the particles mass, $\hat{x}$ and $\hat{p}$ are the position and momentum operators respectively, g is the acceleration due to gravity, t is the continuous time variable, T is the pulse period, $G = 2\pi/\lambda_{spat}$, where λ_{spat} is the spatial period of the applied potential, U_{max} is the maximum value of the potential due to the standing wave and was calculated by finding the energy eigenvalues of Eq. (2.12) for a standing wave. The resulting equations for the *change* in energy of ground and excited states are,

$$\Delta E_g = \frac{\hbar\Omega_0^2 \cos^2(\frac{G}{2}z)}{4\delta} \tag{2.34}$$

and

$$\Delta E_e = -\frac{\hbar\Omega_0^2 \cos^2(\frac{G}{2}z)}{4\delta}, \tag{2.35}$$

where $\Omega_0 = \mu\mathcal{E}_0/\hbar$ with $\mathcal{E}_0$ being the electric field amplitude of the light field. The limit of $\Omega_0 \ll \delta$ was used in defining Eqs. (2.34) and (2.35). These equations are known as the light shift, since they scale with Ω_0^2, which is proportional to the light intensity. Figure 2.2 shows a graphical representation of the light shift.

In practice, the $1 + \cos(G\hat{x})$ term in Eq. (2.33) can often be written as $\cos(G\hat{x})$, since the 1 only leads to a constant phase shift of the wavefunction, which in most experiments is not detected. All further calculations in this thesis will omit the 1. Further simplification can be achieved if the position and momentum operators are rescaled to dimensionless quantities. We rescale the momentum $\hat{p}$ in units of $\hbar G$, the position $\hat{x}$ in units of G^{-1}, and the mass in units of m. The resulting dimensionless Hamiltonian is given by

$$\hat{H}(t) = \frac{\hat{p}^2}{2} - \frac{\eta}{\tau}\hat{x} + k\cos(\hat{x}) \sum_{N_p} \delta(t - N_p\tau), \tag{2.36}$$

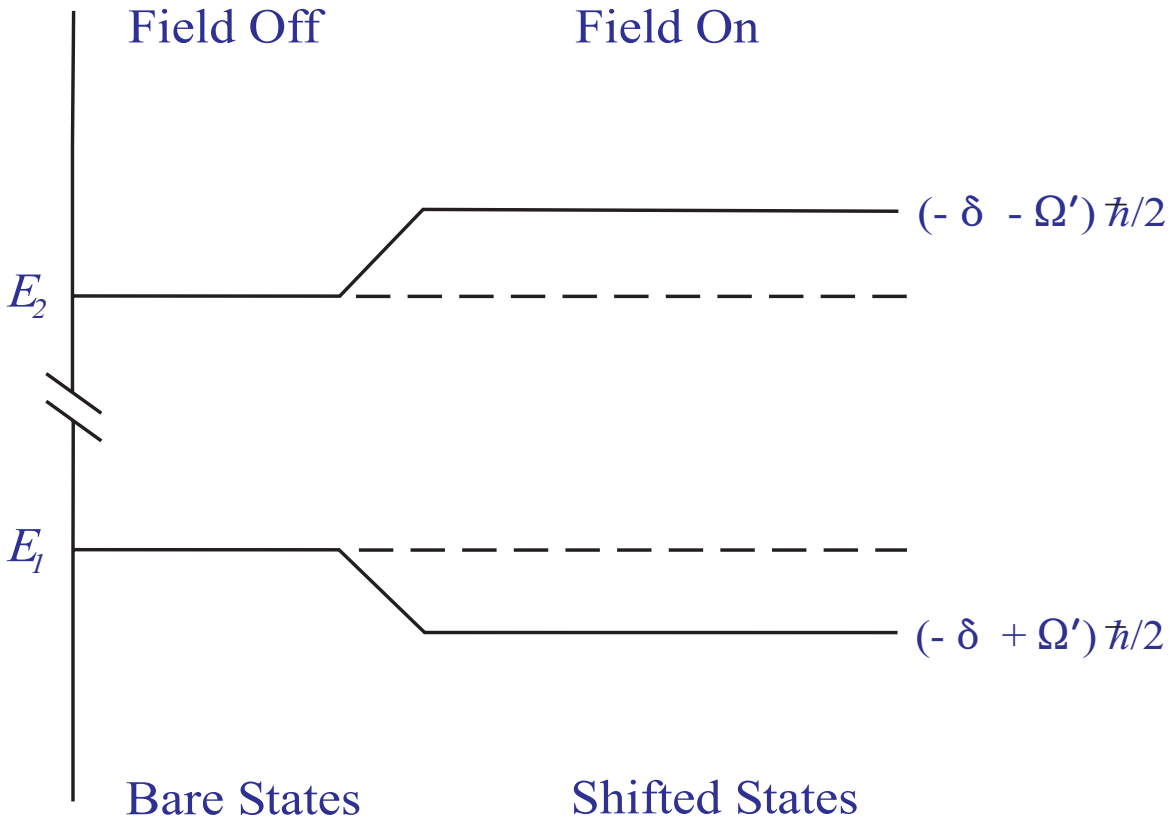

Figure 2.2. Energies of the coupled states with the light field off (bare states) and with the light field on (shifted states) with $\delta<0$ and $\Omega' = \sqrt{\delta^2 + \Omega_0^2 \cos^2(kz)}$.

where $k = U_{max}/2\hbar$, $\tau = \hbar T G^2/m$, and $\eta = mgT/\hbar G$. The dynamics of the system are fully characterized by the dimensionless quantities k, τ, and η.

Next we look at the evolution of a particle through a pulse and the free evolution to the next pulse by substituting Eq. (2.36) into the time dependent Schrödinger equation. Gravity and kinetic energy have little effect during a pulse, since the interaction time, Δt, is short. The atoms are said to be in the Raman-Nath regime. Therefore, the corrugated potential of the standing light wave acts on the atoms as a thin phase grating. We let $|\Psi_n\rangle$ be the wavefunction before a pulse and $|\Psi'_n\rangle$ be the wavefunction immediately after the pulse. The result is

$$|\Psi'_n\rangle = e^{-i\phi_d[\cos(\hat{x})]}|\Psi_n\rangle, \tag{2.37}$$

where ϕ_d is the phase modulation depth of the potential,

$$\phi_d = k\Delta t. \tag{2.38}$$

Figure 2.3 shows a graphical representation of the diffraction of atoms due to the standing light wave. Mathematically, the fact that the standing light wave acts as a diffraction grating can be seen when we expand Eq. (2.37) as a series of Bessel functions using the identity $e^{iz\cos(\theta)} = \sum_{l=-\infty}^{\infty} i^l J_l(z) e^{il\theta}$. The result is

$$|\Psi'_n\rangle = \sum_{l=-\infty}^{\infty} i^l J_l(\phi_d)|p_l\rangle, \tag{2.39}$$

where J_l is the lth order Bessel function of the first kind and $|p_l\rangle$ represents a momentum state with momentum in the grating direction of $p = l\hbar G$. The Bessel function $J_l(\phi_d)$ has a maximum at $\phi_d \sim l + 1$.

Using the first two terms of Eq. (2.36) in the Schrödinger equation gives the free evolution with gravity of the particle from just after a pulse to the start of the next pulse. We let $|\Psi_{n+1}\rangle$ denote the wavefunction just after the free evolution. The result is

$$|\Psi_{n+1}\rangle = e^{-i\tau(\frac{\hat{p}^2}{2}+\eta\hat{x})}|\Psi'_n\rangle. \tag{2.40}$$

This gives us a total evolution from before a pulse to the start of the next as

$$|\Psi_{n+1}\rangle = e^{-i\tau(\frac{\hat{p}^2}{2}+\eta\hat{x})} e^{-i\phi_d[\mathrm{COS}(\hat{x})]}|\Psi_n\rangle. \tag{2.41}$$

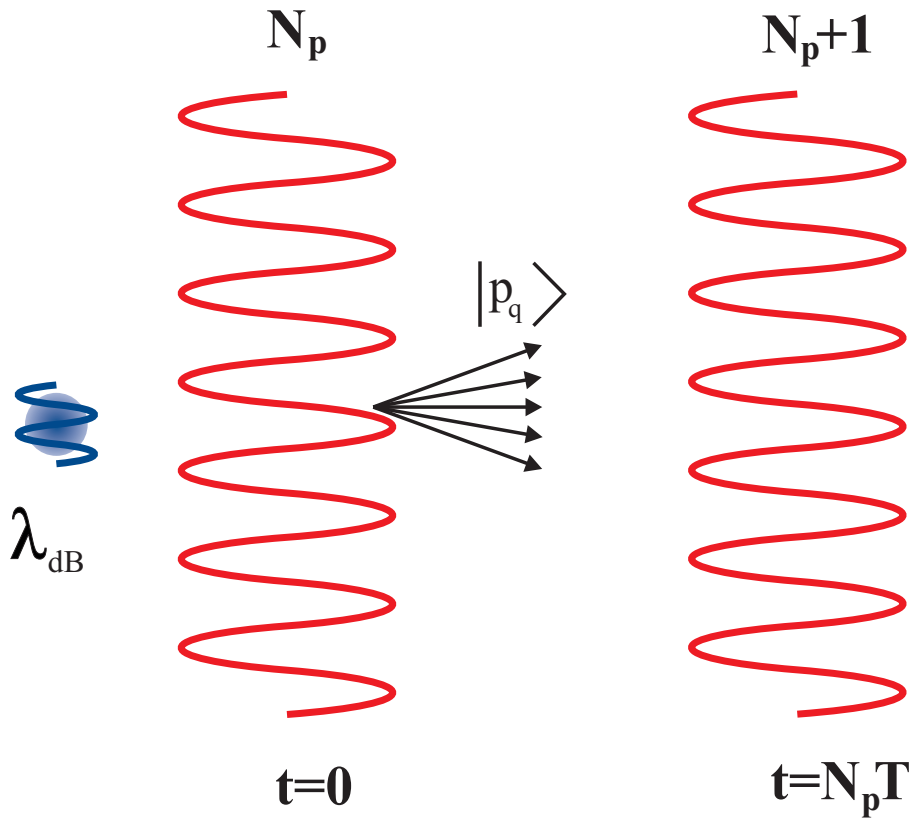

Figure 2.3. Diffraction of atomic deBroglie waves from a standing wave. This spatially varying potential splits the deBroglie wave into a series of momentum orders.

2.3.1 Phase Model

We need to find the conditions for the initial velocity v_i of the atoms and the pulse separation time T that produce an accelerator mode. We suggest that the condition for an accelerator mode is that the atomic wave needs to replicate itself from pulse to pulse. For an accelerator mode that maintains its form over time, the atomic wave should have a fixed phase relationship between its constituent momentum states as the pulse number increases. To simplify the labeling of diffraction orders and the momentum gained with each pulse, a new parameter q is introduced which represents the total number of grating recoils, $\hbar G$, that the accelerator mode has gained through the N_pth pulse. Therefore, the phase accumulated by an accelerator mode during the free evolution after the N_pth and before the $(N_p + 1)$th pulse is given by

$$\phi_q = \frac{\tau}{2} q^2 + \frac{v_i m \tau}{\hbar G} q + \eta \tau N_p q, \tag{2.42}$$

where the first term is due to the recoil frequency shift. The second term represents the phase change due to the initial velocity, given by the Doppler frequency shift, $G \cdot p_i/m$, times the scaled pulse period. The third term is the Doppler frequency shift due to the acceleration of gravity, $gGT^2 = \eta\tau$.

The phase difference between adjacent momentum states within the accelerator mode is

$$\phi_q - \phi_{q-1} = \frac{\tau}{2}(2q - 1) + \frac{v_i m \tau}{\hbar G} + \eta \tau N_p. \tag{2.43}$$

It is postulated that, in order for the accelerator mode to replicate itself from pulse to pulse, this phase difference needs to be equal to or close to integer multiples of 2π. We can separate Eq. (2.43) into an equation containing terms which depend on q and N_p and an equation independent of these quantities. Once again, we postulate that each of these components must individually be an integer multiple of 2π. The result is

$$\tau q + \eta \tau N_p = 2\pi q l', \tag{2.44}$$

and

$$\frac{v_i m\tau}{\hbar G} - \frac{\tau}{2} = 2\pi l, \tag{2.45}$$

where l and l' are integers. The initial velocity condition can be found from Eq. (2.45) once a pulse separation time is found from Eq. (2.44). This rephasing condition is analogous to the Talbot effect[39] in optics, where self-imaging of a diffraction grating occurs at distinct distances from the grating. In the case of atoms without gravity, this rephasing can be exact and happen simultaneously for all momentum states, since the velocity of the atom along the grating does not change between pulses. In the case of accelerator modes, the gravitational acceleration only allows a few momentum states to approximately rephase. The Talbot formalism can still provide an important guide for treating this problem, as these times, integer half multiples of the Talbot time are the quantum resonances. Therefore we scale the time by the half-Talbot time, $T_{1/2} = 2\pi m/\hbar G^2$, where $T_{1/2}$ is about 33μs for rubidium 87 at $\lambda_{spat} = 390$ nm. For the scaled half-Talbot time, we have

$$\tau = \alpha\tau_{1/2}. \tag{2.46}$$

The substitution of Eq. (2.46) into Eqs. (2.44) and (2.45) results in

$$(\alpha - l')q + \eta\alpha N_p = 0, \tag{2.47}$$

and

$$v_i = (l + \frac{\alpha}{2})\frac{\hbar G}{m\alpha}. \tag{2.48}$$

Solving Eq. (2.47) for q produces the momentum of the QAM as a function of scaled pulse period,

$$q = \frac{\eta\alpha N_p}{(l' - \alpha)}. \tag{2.49}$$

From this one can readily see that without gravity, i.e. $\eta = 0$, the accelerator mode has no momentum. Figure 2.4 graphically represents Eq. (2.49).

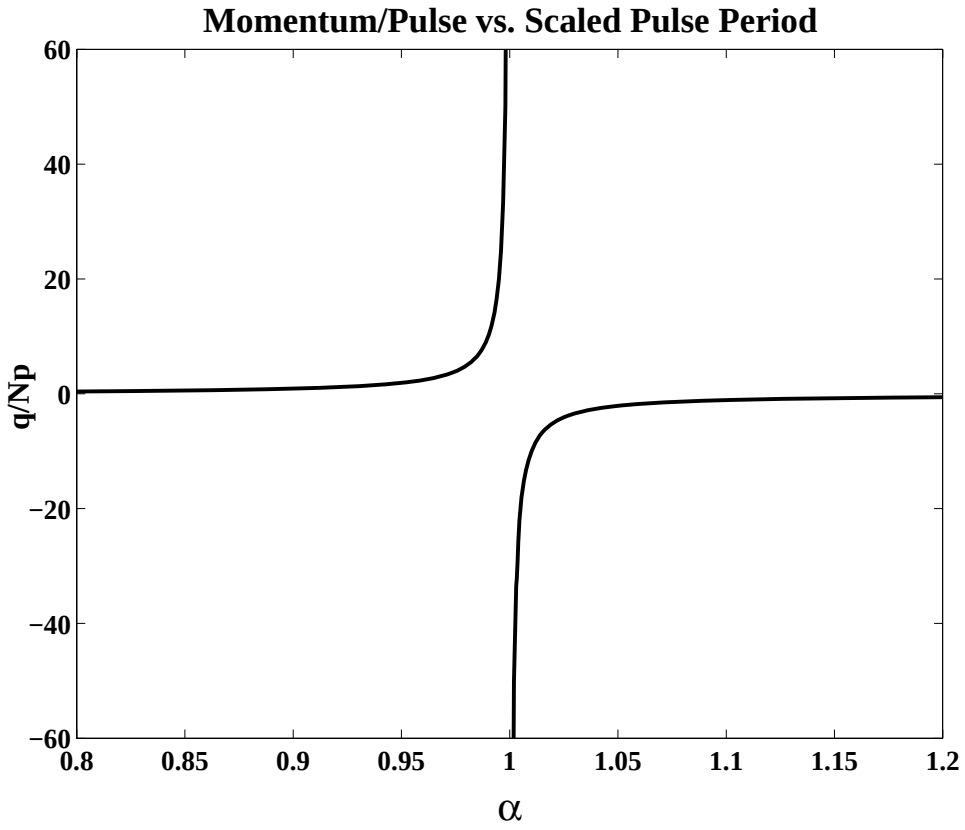

Figure 2.4. The momentum of the accelerator mode per pulse versus scaled pulse period for l'=1. Note the discontinuity which occurs exactly at the resonance position of the half-Talbot time. This plot is calculated using Eq. (2.49)

.

2.3.2 ϵ-classical Theory

In the previous section, we discussed a phase model approach to understanding the theory of QAM's. While this model was accurate in accounting for the existence of QAM's when $l' = 1$, there was an issue of higher order QAM's with $l' > 1$ where these ideas proved not to work so well. In what follows we discuss a different approach which can successfully treat higher order modes. To begin we transform the Hamiltonian to a freely falling frame by replacing $\hat{p} - \frac{\eta}{\tau}t'$ by $\hat{p}$. This gives

$$\hat{H}(t') = \frac{1}{2}(\hat{p} + \frac{\eta}{\tau}t')^2 + k\cos(\hat{x}) \sum_{N_p} \delta(t' - N_p\tau). \tag{2.50}$$

This Hamiltonian is related to Eq. (2.36) by the gauge transformation $e^{i\eta\hat{x}t'/\tau}$. Now $\hat{x}$ only appears in the cosine term and the Hamiltonian resembles that of the famous kicked rotor system[23]. Throughout the rest of the thesis, time is a discrete variable represented by the pulse counter, N_p. The $\frac{\eta}{\tau}t'$ term is the fractional quasimomentum. The atoms can have initial momentum that is a fraction of the momentum gained with a pulse. Since the grating only transfers integer $\hbar G$ multiples of momentum, the fractional quasi-momentum is conserved. Thus, we separate the momentum into integer and fractional parts by putting $p = n + \beta$. Where n and β are the integer and fractional parts, respectively. Since β, fractional quasimomentum, is conserved, only n varies throughout the dynamics of the system, and the evolution can be described as a superposition of individual pulsed states, each with a separate value for β. These states are typically called β rotors[22]. Now, the step evolution operator is found from Eq. (2.50) by $\hat{U} = e^{-i\int \hat{H}(t')dt'}$ with $\hbar = 1$ and limits from just after the N_pth pulse to just after the next pulse $(N_p + 1)\tau$. Besides a constant phase factor the evolution operator is,

$$\hat{U}_\beta(N_p) = e^{-ik\cos(\hat{\theta})}e^{-i(\tau/2)(\hat{N}+\beta+\eta N_p+\eta/2)^2}. \tag{2.51}$$

where $\theta = x \bmod(2\pi)$ and the momentum operator is $\hat{N} = -i\frac{d}{d\theta}$. With no gravity, $\eta = 0$, and Eq. (2.50) reduces to the normal kicked rotor Hamiltonian, giving a

classical standard mapping with stochasticity parameter $K = k\tau$. For $K > K_c \approx 0.9716$ diffusion in momentum occurs [40].

With gravity present, $\eta \neq 0$, resonances occur around integer multiples of 2π and thus we restrict our discussion to τ close to these values. In particular we let $\tau = 2\pi l + \epsilon$ and $k = \tilde{k}/|\epsilon|$, with ϵ small and use the identity $e^{-i\pi l n^2} = e^{-i\pi l n}$ when l and n are integers. Now, the evolution operator takes on the form:

$$\hat{U}_\beta(N_p) = e^{(-i/|\epsilon|)\tilde{k}\cos(\hat{\theta})} e^{-(i/|\epsilon|)\hat{H}_\beta(\hat{I},N_p)}, \tag{2.52}$$

where the angular momentum operator

$$\hat{I} = |\epsilon|\hat{N} = -i|\epsilon|\frac{d}{d\theta}, \tag{2.53}$$

and

$$\hat{H}_\beta(\hat{I}, N_p) = \frac{1}{2} sign(\epsilon)\hat{I}^2 + \hat{I}[\pi l + \tau(\beta + \eta N_p + \frac{\eta}{2})]. \tag{2.54}$$

As seen in Eq. (2.53), $|\epsilon|$ must take the role of Planck's constant because of the angular momentum operator definition of $\hat{I}$. Now $\hat{U}_\beta$ and $\hat{H}_\beta$ lead to the following time-dependent maps,

$$\begin{aligned} I_{N_p+1} &= I_{N_p} + \tilde{k}\sin(\theta_{N_p+1}) \\ \theta_{N_p+1} &= \theta_{N_p} \pm I_{N_p} + \pi l + \tau(\beta + N_p\eta + \eta/2) \bmod(2\pi), \end{aligned} \tag{2.55}$$

where $\pm$ is chosen according to the sign of ϵ. Since ϵ behaves as Planck's constant, the "classical" dynamics will occur in the limit of $\epsilon \to 0$ and not $\hbar \to 0$. Taking $\hbar \to 0$ would set the dimensionless parameters, $k \to \infty$, $\tau \to \infty$, $\eta\tau > 0$ and would arrive at the "classical" limit only if $l = 0$ in Eq. (2.55). We let $J_{N_p} = I_{N_p} \pm \pi l \pm \tau(\beta + \eta N_p + \eta/2)$, to remove the explicit time dependance of the mapping. This results in,

$$\begin{aligned} J_{N_p+1} &= J_{N_p} + \tilde{k}\sin(\theta_{N_p+1}) \pm \tau\eta \\ \theta_{N_p+1} &= \theta_{N_p} \pm J_{N_p}. \end{aligned} \tag{2.56}$$

If J, θ are both mod(2π) and J_0, θ_0 is a period $\mathbf{p}$-fixed point of either map, then the iteration of Eq. (2.56) at $N_p = \mathbf{p}$ gives,

$$\begin{aligned} J_p &= J_0 + 2\pi\mathbf{j} \\ \theta_p &= \theta_0 + 2\pi m, \end{aligned} \tag{2.57}$$

where $\mathbf{j}$, m are integers. Reverting back to the original dynamics in Eq. (2.55), any integer N_p, gives a family of orbits,

$$I_t\mathbf{p} = I_0 + aN_p\mathbf{p}, \qquad \theta_t\mathbf{p} = \theta_0 = \vartheta_0 \text{ mod}(2\pi), \tag{2.58}$$

where $a = \mp\tau\eta + 2\pi\mathbf{j}/\mathbf{p}$ and $I_0 = J_0 \mp \pi l \mp \tau(\beta + \eta/2) + 2\pi m'$ with m' any integer.

Therefore, the primitive periodic orbits of Eq. (2.56) correspond to accelerator orbits of Eq. (2.55) with a linear average growth of momentum with time. This momentum growth with time is the signature of the accelerator modes. Each is characterized by an *order* ($\mathbf{p}$) and a *jumping index* ($\mathbf{j}$). The order $\mathbf{p}$ represents how many pulse periods it takes before cycling back to the initial point in phase space. The jumping index is related to how many units of the grating momentum are given per cycle.

Modes of order 1 give $J_0 = 0$ and $\theta_0 = \theta_{\mathbf{j}}$ and are fixed points of the map Eq. (2.56). This gives

$$\sin(\theta_{\mathbf{j}}) = (2\pi\mathbf{j} \mp \tau\eta)/\tilde{k}, \tag{2.59}$$

where $\mathbf{j}$ is any integer, such that the result is not greater than ± 1. We can restructure Eq. (2.59) as an inequality,

$$|2\pi\mathbf{j} \mp \tau\eta| < \tilde{k} < \sqrt{16 + (2\pi\mathbf{j} \mp \tau\eta)^2}. \tag{2.60}$$

This gives bounds on the stability of the mapping of Eq. (2.56). As $\tilde{k}$ moves out of these bounds bifurcations occur. As $\tilde{k}$ gets small, higher order accelerator modes appear, with higher period primary orbits. This leads us to find the higher order accelerator mode momentum. If there are enough atoms meeting the necessary initial conditions then an accelerator mode will be observed which is governed by a

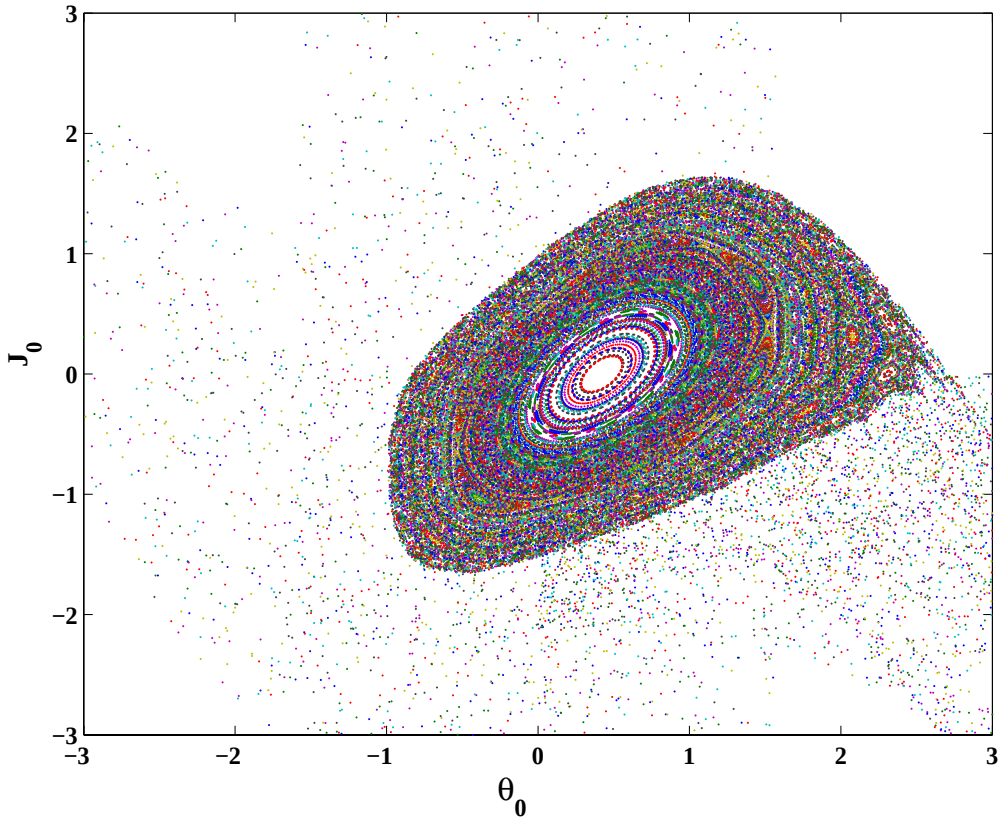

Figure 2.5. Phase space plot of the mapping Eq. (2.56) on the 2-torus, with $\tau = 5.86$, $\eta = 0.0925$, and $\tilde{k} = 1.329$. A stable fixed point exists at $J_0 = 0$ and $\theta_0 = 0.42$

.

momentum equation determined using Eq. (2.58),

$$n_{QAM} = -\frac{N_p \tau \eta}{\epsilon} + 2\pi \frac{N_p \mathbf{j}}{\mathbf{p}\epsilon} \tag{2.61}$$

Notice for the (1,0) accelerator modes that the second term is zero. Although one would think an infinite number of accelerator modes could be seen, the inequality of Eq. (2.60) must have the proper τ, $\tilde{k}$, and jumping index, $\mathbf{j}$. Higher order accelerator modes, as will be observed, are more prominent closer to the resonances and have a much smaller momentum gain per pulse.

CHAPTER 3

EXPERIMENTAL APPARATUS

This chapter gives a detailed description of the components used in the experiments and their purpose(s). Two optical tables, one with the vacuum chamber and one with the lasers, were used to mount the components described in this chapter. Laser light was transferred to the optical table with the vacuum chamber using optical fibers. One advantage of this arrangement was the beam profile exiting the optical fiber was cleaner than the one exiting the laser. Another purpose was to simplify the optical alignment procedure. We could adjust the optical components on the laser-optical table without disturbing the optics on the table on which the vacuum system was mounted.

The optical arrangement from the lasers to the vacuum chamber used for achieving a MOT, performing the kicking experiments, and getting the TOF signal is also described in detail. The light in these parts of the experiment traveled through various optical components such as, acousto-optical modulators (AOMs), polarizing beam splitting cubes (PBSCs), half waveplates (HWPs), and quarter waveplates (QWPs). All of these components were used to adjust the laser light to the proper frequencies and polarizations for creating the many aspects of the experiment. The AOMs and many of the electronic components were controlled through Labview interfaced with data acquisition cards (DAQs). A description of the DAQs is given in this chapter.

The engineering and design of the ultra-high vacuum system is detailed along with the vacuum components. Since the temperature of atoms released from a MOT is typically in the μK range, interactions with background gas become a major problem.

Thus, an ultra-high vacuum system was needed to prevent these background gases from significantly interacting with the cold atoms.

3.1 Computer Control and Automation

National Instruments Labview 6.1 was used for experimental control and data acquisition, while Matlab was used for the data analysis. Labview's graphical programming architecture was more suited for the task of controlling the experimental enviornment, whereas, Matlab's array based programming formalism was more proficient at data manipulation, file input/output, and graphing. The programs were installed on separate computers to perform the tasks of experimental control and data analysis independently. An overview of the Labview and Matlab code is given in Appendix A.

Labview interfaced with a National Instruments PCI-6023E analog input(AI)-digital input/output(DIO) data acquisition card(DAQ) and a National Instruments PCI-6711 analog output(AO) DAQ. The two DAQ cards were used to control various parameters of the system and acquire data as described in this thesis. Also, Labview was used to program an HP8770A arbitrary waveform generator through a general purpose interface bus (GPIB) for operation of the pulsing AOM.

3.2 Vacuum System

The vacuum system needed to be able to attain an ultra-high vacuum and have good optical access. A vacuum chamber and pump were chosen with these parameters in mind. The vacuum chamber, shown in Fig. 3.1, consisted of a Kimball Physics model MCF275-SC600-A 304 stainless steel spherical cube with a 2.6 inch inside diameter. Each cube side had a 1.5 inch clearance hole with a 2.75 inch Conflat (CF) flange sealing surface. The cube was bolted on top of an MDC Vacuum Products 1.5 inch diameter 304 stainless steel 6-way cross tube with 2.75 inch CF flanges on each end. A four pin electrical feedthrough was torqued on one end of the six-way cross

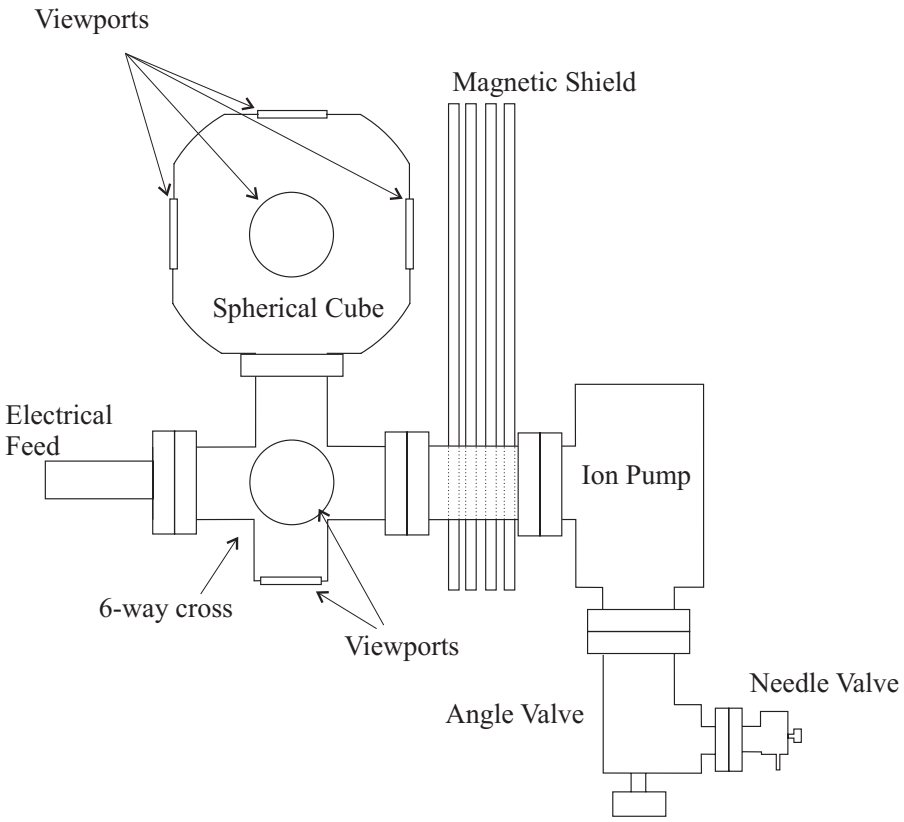

Figure 3.1. The major components of the vacuum system were the spherical cube, an ion pump, viewports, and an electrical feed through.

tube. This allowed for the connection of the SAES Getter rubidium sources. Inside the chamber, two independant rubidium sources were pressed onto wires leading to the spherical cube. When one source was depleted the other could be wired to supply the rubidium instead. A two port generic "Varian style" 8 liter/s ion pump was connected to the six-way cross tube through a 6 inch extension and maintained vacuum at 10^{-9} Torr. At this pressure, collisions between background gas molecules and rubidium atoms were negligible. The ion pump was powered by a Terrenova 751 Controller. A 1.5 inch manual angle valve was connected to the second port of the ion pump to close off the system. It was very important to reduce stray magnetic fields in the region of the MOT. Thus the 6 inch extension was employed to position the ion pump's 1200 Gauss permanent magnet further away from the cube. Also, four 0.0625 inch thick magnetic shields were placed between the magnet and cube to further reduce the effect of the magnet at the cube. The remaining ports in the vacuum system were closed off with quartz viewports.

The viewport windows were 2.0 inch diameter, 0.25 inch thick, anti-reflection coated, quartz flats. The quartz flats were attached to five sides of the cube with 2.75 inch oxygen free copper gaskets from MDC Vacuum Products. The copper gaskets were sealed per reference[41] which consisted of machining a raised knife edge on one side of the copper gasket. Figure 3.2 shows the attachment of the copper gaskets and windows to the vacuum chamber. The copper gaskets were annealed in a bakeout chamber at 500°C for two hours to soften the copper so as to provide a more efficient seal. The flat side of the copper gasket was placed on the spherical cubes CF flange sealing surface, the quartz window was placed on top of the machined knife edge, and a 2.75 inch clearance flange with a clearance hole of 1.5 inches was placed on top of the quartz window with a soft copper ring. The ring prevented the clearance flange's knife edge from contacting the viewport and in addition provided a cushion for the viewport. The clearance flange was bolted to the spherical cube with six bolts. Applying torque on the viewports was a very time consuming process. As can be seen

in Fig. 3.2, the contact point of the gasket on the viewport was very small. Thus, the torque was applied in a cross bolt pattern in increments of 0.25 ft-lbs until no leaks were found in the initial pump down (described below). The final torque on the viewports was 1.5-2.0 ft-lbs. A quartz window was bolted to the bottom of the six-way cross for additional optical access to the spherical cube. Two other windows were bolted on opposite sides to the six-way cross tube for time of flight measurements.

Prior to assembling the vacuum system, all parts were cleaned with methanol to remove any foreign material. Also, gloves were worn to handle the clean components to prevent contamination. During the assembly of the viewports, argon gas was pumped into the system to minimize the build up of normal atmospheric gas (particularly water vapor) on the vacuum walls. During initial pump down and bakeout, a Leybold Turbovac 50 turbo pump was connected to the angle valve. A Leybold Trivac B model D1.6B rotary vane roughing pump maintained proper inlet pressure for the turbo pump. The turbo pump maintained a minimum pressure of $8\text{x}10^{-9}$ Torr with an inlet pressure of 10^{-3} Torr. A Varian type 0351 vacuum gauge was installed to indicate pressures in the range of atmospheric down to 10^{-4} Torr. An initial pump down was performed to find any major leaks in the system. Leak checks were performed by applying either helium or acetone to the CF flanges and viewport seals. A leak was indicated by a rapid rise in pressure on the vacuum gauge. Great care was taken in applying additional torque to the viewport bolts if a leak was found in one of the viewport seals. After removing all leaks, the system was prepared for a bakeout. The purpose of the bakeout was to remove any foreign material, such as oil or water, from the system which was not removed with methanol. Also, it reduced the outgassing of impurities in the metal during the final experiments. The procedure started by installing ceramic heaters, powered by variable transformers (variac), near the vacuum chamber. Two J-type thermocouples were attached to the system with heat conducting adhesive for temperature indication. Each end of the thermocouples

was plugged into a separate AI port on the PCI-6023E DAQ card. An insulated blanket covered the system. With the turbo and roughing pumps running and ion pump off, a slow heat-up began by increasing the varaic's voltage. The temperature was increased in 20°C increments and allowed to stabilize at each increment. The temperature was raised to a maximum of 200°C over a time period of about eight hours, that is, a heat up rate of about 25°C/hr. The slow heat-up was used to ensure that the system was not thermally stressed. The maximum temperature was determined by the specifications of the magnet as well as the vacuum seals. The system was maintained at 200°C for about a week. A sudden rise in pressure was an indication of outgassing. When a pressure of 10^{-6} Torr was reached during the bakeout the ion pump was started and pressure was read from the ion pump controller. Also, foreign material was burnt off of the rubidium sources by supplying each source with 4 to 5 Amps of current for an hour. This was done periodically until no change in pressure was seen when applying normal operating currents of 2.5 to 3.0 Amps. When the pressure stabilized to 10^{-9} Torr after a week, a cool down commenced by lowering the voltage in the variac. After the cool down, a final leak check was performed. The angle valve was shut and the turbo and roughing pumps were removed. A 0.25 inch needle valve was installed on the input angle valve's CF flange and a small vacuum was created in the space between the angle valve and needle valve to lower the differential pressure across the angle valve. The vacuum system was now ready for experiments.

3.3 Laser and Optical System

3.3.1 Lasers

The lasers were chosen according to several important characteristics. They needed to have the proper wavelength, high power, the ability to lock and stay locked to < 1 MHz of a specific spectral line, and be mechanically stable. Laser diodes were

chosen as the light source, since they met the wavelength and power requirements. The optical table and a large base attached to the laser provided the mechanical stability. In order to form a MOT and reproduce the same MOT, the lasers needed to be locked near a spectral line. This was done using an external cavity diode laser (ECDL) setup in a Littrow[42] configuration, where the light was diffracted from a grating and the first order diffraction was sent back into the diode as optical feedback. The zeroth order exited the cavity housing and was available for experiments. Initial adjustments of the laser required that the first order be aligned back to the diode. This was done by finding the lasing threshold of the laser by lowering the current through the diode until the lasing stopped. The horizontal and vertical position of the grating was then adjusted to find the minimum current at which the laser was lasing. A rubidium vapor cell was used for saturated absorption spectroscopy, where the master laser scanned across the $F = 2 \rightarrow F' = 1, 2, 3$ transitions and the repump scanned across $F = 1 \rightarrow F' = 0, 1, 2$ transitions. This gave us the spectral lines to lock the lasers. Also, to minimize thermal drift in the laser frequency, a thermoelectric cooler provided a heat sink for the laser diode. The power output of the master laser was not sufficient at producing a MOT, therefore two other lasers were built as amplifiers to provide increased power. These lasers were free running diode lasers injection locked[43] to the master laser. This was done by supplying a small amount of power from the master and aligning it into the cavity of the primary slave laser. A portion of the primary slave laser light went through a vapor cell for an absorption profile. With the proper current and temperature set, the primary slave would be at the same frequency as the master laser. The other part of the primary slave's light was injected into two secondary slaves (characteristics similar to the primary slave), one for the laser cooling experiments and one for the BEC experiments. The light from our secondary slave was used for the laser cooling and TOF measurements.

Figure 3.3 shows the optical setup for the lasers and the optical components. The master and repump lasers were Toptica Model DL100 extended-cavity diode

lasers (ECDLs) with a maximum output power of approximately 25 mW and a wavelength of 780 nm. A DC100 current control in the laser supply rack powered the diode laser. A thermoelectric cooler maintained the diode laser temperature and was controlled by the DTC100 temperature controller also in the supply rack. The laser light passed through a collimating lens to the grating and out the laser housing. The micrometer screws on the grating mount allowed for feedback and wavelength adjustments. The horizontal grating position was adjusted when the laser was operating in a bad mode. This was seen as a poor saturated absorption profile on the oscilliscope with numerous discontinuities. A piezo actuator was attached to the grating mount and provided fine tuning of the wavelength through the SC100 scan control in the supply rack. The primary and secondary slaves were Sharp Microelectronics 784 nm wavelength diode lasers with a 120 mW maximum output power. These lasers were powered by Thorlabs LDC500 current controllers and the temperature was maintained with a thermoelectric cooler (TEC) driven by a Thorlabs TEC2000 Thermoelectric Temperature Driver. These diode lasers, shown in Fig. 3.4, were housed in aluminum mounts built in-house.

3.3.2 Doppler Broadening and Saturated Absorption Spectroscopy

In order to lock the lasers, a signal was needed for input to the laser circuitry. We chose a saturated absorption spectroscopy signal, because it was robust and easy to setup. We also monitored the absorption of a low intensity beam from the slave through a vapor cell in order to give an indication of its lock to the master laser.

Broadening of the atomic line occurs in a vapor cell due to a Doppler shift in the laser frequency seen by the atoms. This results in a doppler-broadened linewidth at full width half maximum (FWHM)[44] of,

$$\Delta\omega_d = \omega_0\sqrt{8\ln 2\frac{k_B T}{mc^2}}, \tag{3.1}$$

where ω_0 is the transition frequency, k_B is the Boltzmann's constant, T is the temperature, m is the atoms mass, and c is the speed of light. Figure 3.5 shows the

absorption profile for the slave lasers. The linewidth was about 500 MHz for rubidium 87 at 300 K. This was a large linewidth so that in order to resolve the hyperfine levels in Fig. 3.10 it was necessary to perform saturated absorption spectroscopy.

The technique of saturated absorption spectroscopy involved splitting the light exiting the laser into a low power "probe" beam and high power "saturating" beam. Here, low power was well below the saturation intensity ($\approx 25\%$ of saturation intensity) and high power was above saturation (≈ 1.5 times saturation intensity). The two beams were approximately counterpropagating through a vapor cell with the probe beam incident onto a photodiode after the cell as shown in the upper left corner of Fig. 3.3. For the master laser, We scanned the frequency across the $F = 2 \rightarrow F' = 3, 2, 1$ transitions. When the frequency was close to a transition, only those atoms with zero velocity with respect to the probe and saturating beam's directions would be on-resonant. The saturating beam would equalize the populations between excited and ground state (saturation). Therefore, the probe beam had fewer atoms to excite resulting in an intensity increase on the photodiode ((a), (c), and (f) labels in Fig. 3.6). The crossover peaks, labels (b), (d), and (e) in Fig. 3.6, are not transitions. These were the result of the laser frequency being halfway between the resonant frequency of two lines. For atoms with certain velocities the Doppler shift allows the probe and saturating beam to be on-resonant with two different excited states. This has the effect of lowering the population in the ground state to an even greater extent. Thus, the probe beam intensity was increased even more than for the regular saturated absorption peaks.

3.3.3 Laser Locking Techniques

Laser locking was required to recreate the experiments with the same frequency of light. Our requirement, stated above, that the laser must be able to stay locked to <1 MHz of an atomic line was met by locking to a peak in the saturated absorption spectroscopy[45,46] signal. When we first began building the experiments, two other

methods were also considered as candidates for laser locking. These were dichroic-atomic-vapor laser lock[47] (DAVLL), and locking to a polarization spectroscopy[48] signal.

The DAVLL technique uses a weak magnetic field to split the Zeeman components of an atomic Doppler broadened absorption signal. Laser light exiting the laser passes through a linear polarizer. After the polarizer, the lights polarization is equivalent to two equal amounts of circular polarizations (σ_+ and σ_-). The light then passes through a vapor cell, a quarter waveplate to convert the two circular polarizations to two orthogonal linear polarizations, and through a polarizing beam splitting cube to split the two polarizations. Each beam enters a separate photodiode for an absorption profile. The absorption of σ_+ (σ_-) polarized light shifts the Doppler-broadened absorption signal to a positive (negative) frequency in reference to a Doppler-broadened absorption signal with no magnetic field. Therefore subtracting the two signals produces a dispersion signal which is fed into a locking circuit controlling the laser grating.

Polarization spectroscopy on the other hand, signal uses light-induced birefringence and dichroism of the alkali gas. The setup is similar to our system described below (weak probe beam counterpropagating a saturating beam)) except that the saturating beam is replaced by a polarizing beam. The polarizing beam is circularly polarized and induces a different saturation and index of refraction. The probe beam passes through a crossed polarizer and a polarizing beam splitting cube to separate the different polarizations. As in the DAVLL, the two signals are subtracted and the laser is locked to a zero crossing. The two methods described needed more equipment and required more time in setting up the apparatus. Thus, the technique of locking to a saturated absorption spectroscopy signal was utilized for our laser locking requirements.

The saturated absorption signal in Fig. 3.6 was used as input to the the lock-in regulator LIR100 in the master laser's supply rack. The laser frequency was modulated with a 17 kHz sine wave. This wave was mixed with the absorption signal to create a dispersion signal. The dispersion signal as well as the absorption signal was observed on an oscilloscope. The scan through the laser frequencies was reduced to the $F = 2 \rightarrow F' = 3$ crossover peak (label (e) in Fig. 3.6) and the laser was locked.

3.3.4 Acousto-optical Modulator(AOM)

The different stages of the experiment necessitated that the laser light frequency was switched through three different values, one for the MOT, one for the optical molasses, and one for the TOF. This required the use of an acousto-optical modulator (AOM) with the proper bandwidth to shift the frequency of the laser light over a wide range. Another advantage of an AOM was its fast switching time. The beam size through the AOM had a significant impact on the switching times. Therefore, all of the AOM's were positioned at the focus of an approximately one-to-one telescope.

Our AOM's were made up of a piezoelectric transducer attached to a lead molybdate ($PbMoO_4$) crystal. A radio frequency (RF) voltage was applied to the piezoelectric transducer to generate an acoustic wave which was driven through the crystal. As shown in Fig. 3.7, laser light of frequency f_0 entered the AOM crystal at the Bragg angle, Φ_B, causing the light to diffract from the standing wave in the crystal. The laser light exited the AOM with a zeroth order beam (frequency unchanged) and a first order beam of frequency, f_1, which was Doppler shifted up by the acoustic wave frequency, F. The first order beam angle, Φ, was twice the Bragg angle. The frequency of the first order light could also be Doppler shifted down if the original beam entered the crystal at $-\Phi_B$. The AOM's were able to shift the frequency of laser light within the range of frequencies that could be produced by their driver. The amount of frequency shift depended on the voltage applied to the driver.

Three Isomet Model 1205C-2 AOM's and one Isomet Model 1201E-2 were used in the entire optical setup. The AOM for the repump light was driven by an Isomet Model 301B voltage-tunable RF driver. This driver allowed for frequency control in the range of 60-100 MHz with an applied voltage of 4.2-15.4 VDC. The master AOM was driven by an Isomet Model 322B-805 voltage-tunable RF driver with digital modulation. The digital modulation provided fast switching of the AOM using a digital output (DO) signal from the PCI 6023E DAQ card. The frequency range of the 322B-805 was 60-100 MHz with an applied voltage of 4.2-15.4 VDC. The slave AOM was driven by an Isomet Model 302B voltage-tunable RF driver with a frequency range of 80-150 MHz with an applied voltage of 4.7-15.3 VDC. Finally, the pulsing AOM was driven by an HP8770A arbitrary waveform generator in combination with an Isomet Model RFA-1108 amplifier. The overall configuration of the AOM's, with their different frequency ranges and digital modulations, were chosen such that all of the frequencies necessary to create a sample of cold atoms could be produced. The repump and slave AOM drivers were voltage controlled through the PCI-6711 DAQ cards AO's. During the experiments, the master AOM driver was cycled through several different frequencies for trapping and cooling the atoms in addition to the on-resonant frequency needed for time of flight measurements. This required more voltage than the 10 VDC maximum limit of the PCI-6711 DAQ card AO, so an amplifier circuit was built in order to double the voltage of the AO to the driver.

3.3.5 Shutters

Shutters were required to block the laser light during various parts of the experiment. The shutters in the optical system were designed from scratch and cost about $30.00 to build. The opening/closing time was about the same as a commercial shutter, which cost about $800.00 for the shutter and driver. One undesirable aspect of our shutters was that they did not block 100% of the light. To alleviate this problem the laser beams were focused onto the shutters. This also improved the

opening/closing times. The electronics in Fig. 3.9 were designed using "Electronic Workbench's Multisim". This program was very easy to use and was essential in designing all of the circuits used in the experiments.

The main, TOF, and pulsed light each had a shutter, as shown in Fig. 3.3, and were positioned such that no light entered the vacuum chamber when the shutters were closed. Although the shutters were not capable of blocking all the light under normal circumstances, they did block close to 100% of the light passing through the optical fibers if the shutters were placed before the optical fiber. Therefore, the main and TOF shutters were placed before their respective optical fiber. This could not be done with the pulsing shutter, as its purpose was not to actually block the pulsed light. Its purpose was to block that portion of TOF light not passing through the PBSC after the fiber in Fig. 3.13. The pulsing shutter did not block 100% of the this light, but the leakage was minimal. Also, since the pulsed beam was orientated at an angle relative to the vertical, the atoms had fallen out of the pulsed beam path by the time the TOF light was turned on. The repump light initially had a shutter, however it was found to be unnecessary since applying zero voltage to the repump AOM resulted in no light traveling down the fiber. Thus, the repump AOM was used as a shutter. At a later point in time we had to replace the laser diode in the repump laser. This meant realigning the repump light with the repump AOM as well as the optical fiber. After this procedure the experiments did not work and it was found that a small amount of repump light was entering the vacuum chamber. This necessitated the reinstallation of a repump shutter. Since the majority of the experimental data were taken without a repump shutter, it is omitted from Fig. 3.3. However it is worth mentioning that its placement was before the PBSC, at the entrance to the fiber.

The shutters in Fig. 3.8 as well as the electronics in Fig. 3.9 were all built "in-house". The shutters were an off-the-shelf 9 VDC solenoid housed in a 2 inch^2 aluminum case for heat dissipation. Each shutter was controlled by a separate +5 VDC TTL signal from the PCI-6023E digital output. The original circuit contained a

TL084 quad operational amplifier (op-amp) powered by a ±12 VDC power supply. A +5 VDC TTL signal was sensed on op-amp 1 which turned on the TIP 111A transistor to allow current flow from the +5 VDC power supply through the LM675T high power op-amp. This supplied the shutter (solenoid) with 9 VDC to close the shutter. Immediately after the shutter was closed op-amp 2 output a voltage difference which lowered the voltage across the solenoid to 5.5 VDC for holding the shutter closed. The different voltages, one for energizing and one for holding, were necessary due to the fact that the force required to activate a solenoid is greater than the force required to keep one closed. This last step of lowering to a holding voltage caused the operating time of the shutter to be too long for our experiments (on the order of 100 ms from open to shut). Thus, we removed op-amp 2 and 3, reducing the operating time to 15 ms.

3.4 Laser Cooled Rubidium-87 Atoms

This section gives details of the optical paths in Fig. 3.3. The layout of the components on the optical tables was created to allow us to perform experiments discussed in this thesis while still leaving space for future experiments. As this was not easy, many revisions were made and table space was used up very quickly.

3.4.1 Cooling Light

The master laser light was used for cooling the atoms as discussed in Chapter 2 and was injected into the primary slave which provided light for both experimental apparati (kicking and BEC[17,18]) in the laboratory. The details of the master laser's and the slave laser's optical paths and frequencies were as follows.

The master laser light exited the laser and was split. One part, 15 mW, was used to inject the primary slave laser and 0.5 mW was passed through a rubidium vapor cell for saturated absorption spectroscopy. Figure 3.6 shows a saturated absorption spectrum of the $F = 2 \rightarrow F' = 1, 2, 3$ transitions and crossover peaks. The master

laser used this saturated absorption signal as input to the Lock-in Regulator LIR100 in the laser supply rack. The excited state hyperfine values in Fig. 3.10 were taken from Ye[49] and the ground state values were taken from Bize[50]. The master laser was locked to the crossover peak between $F = 2 \rightarrow F' = 3$ (label (e) in Fig. 3.6) and $F = 2 \rightarrow F' = 2$ (label (c) in Fig. 3.6) of the D2 line (-133.5 MHz below the $F = 2 \rightarrow F' = 3$ transition). After injection, the primary slave's light output was at the same frequency as the master. This light exited the primary slave laser and the power was split in half by a PBSC. One half went to the BEC apparatus, and the other half was sent through the primary slave AOM in a double pass configuration for our experiments. The primary slave AOM's frequency could be switched between the three different frequencies necessary for the experiments (this will be discussed in more detail later). From the AOM, the laser light injected the secondary slave laser, the output of which passed through the secondary slave AOM. This AOM was set at a constant +97 MHz. Henceforth, the light out of the slave AOM will be called the "MOT light". The MOT light, with a power of 70 mW, passed over the main shutter, through a polarizing beam splitting cube, and was coupled into an optical fiber. The MOT light exited the fiber (as shown in Fig. 3.11) at a power of 40 mW corresponding to a coupling efficiency of 60 percent. After the fiber, the MOT light was split into three separate beams and expanded to 0.5 inches in diameter. These beams were passed through quarter waveplates in order to circularly polarize the light. In the vacuum chamber, the beam configuration was such that one of the beams was vertical and the other two were horizontal as in Fig. 3.12. The three beams were orthogonal and were retroreflected through another quarter waveplate to reverse the circular polarization. The next section provides the details of the MOT light polarization orientation. Originally, we had planned on having two of the beams enter the chamber through the same horizontal viewport. This would have given greater optical access for the pulsed beam but required that these beams be at a reduced angle to one another. This angle was so small that it was found that the

cooling process was inefficient due to the small vertical force. The greater force in the horizontal plane during the optical molasses stage led to a force imbalance which increased the temperature of the atoms.

3.4.2 Polarization

As discussed in Chapter 2, the polarization of the cooling light was very important in the interaction with the atoms. The circular polarizations were checked and set through a polarization analyzer. The polarization analyzer consisted of a quarter waveplate (QWP) and a polarizing beam splitting cube (PBSC). By placing the analyzer in the beam path after the QWPs in Fig. 3.11, the polarization was adjusted by rotating the QWPs to maximize the light reflected or transmited by the PBSC in the analyzer. When the analyzer was removed, the light was such that σ_+ (σ_-) circularly polarized light entered the vacuum chamber and reflected back through another QWP. The retroreflected light was opposite circularly polarized, i.e. σ_- (σ_+). Thus, a $\sigma_+ - \sigma_-$ circularly polarized standing wave resulted. The analyzer only supplied the relative polarizations of each beam and not the absolute direction of the rotating polarization. The relative polarizations of the beams was important and needed to be set correctly with respect to the magnetic field gradient.

The orientation of the polarizations in the three MOT light beams was extremely important and was set such that the vertical beam and the horizontal beam, propagating perpendicular to the main coils, had the same circular polarization. Therefore, the horizontal beam in the direction of the magnetic field gradient had the opposite circular polarization. This was necessary because of the quadrupole magnetic field's direction as shown in Fig. 3.15. In order to observe the MOT, the direction of the magnetic field gradient had to match the correct beam polarization as discussed in Chapter 2.2. In the initial stages of observing a MOT, either the current in the main coils or the light polarizations needed to be switched. We switched the direction of current, since this was easier to do.

3.4.3 Repump Light

A probability existed for the atoms to decay to the ground state $F = 1$ through spontaneous emission from the $F' = 1$ or $F' = 2$ state. Without further intervention this would rapidly place all of the atoms in the $F = 1$ ground state and the MOT would disappear. Thus an extra laser was required to depopulate the $F = 1$ state and maintain the cycling transition of the MOT light. The repump laser achieved this objective by exciting the $F = 1 \rightarrow F' = 2$ transition and ultimately optically pumping atoms in the $F = 1$ state into the $F = 2$ state.

The repump laser light exited the laser and passed through the repump AOM in a double pass configuration, where the first order light was sent back through the AOM as in Fig. 3.3. Approximately 1 mW of light was sent through a vapor cell used for the saturated absorption spectroscopy similar to the setup used for the master laser. The repump light was locked to the crossover peak between $F = 1 \rightarrow F' = 2$ and $F = 1 \rightarrow F' = 1$. The repump light was then sent through the same optical fiber as the trapping light by reflecting off of the polarizing beam splitting cube in front of the fiber as shown in Fig. 3.3. There was approximately 1 mW of repump light at the exit of the optical fiber. The repump beam was expanded to be roughly 0.5 inches in diameter and directed through the chamber in the vertical direction. As will be shown later, having the repump light in the vertical direction was critical for the kicking experiments.

3.4.4 TOF and Pulsed Light

Measuring the momentum distribution of the atoms was very important in determining the temperature of the atoms as well for observing QAMs. There were several methods available to us in which to capture the momentum distribution. A charge-couple device (CCD) camera could have been used to take an image of the MOT. These systems were bulky and required another laser beam to enter through

the horizontal viewports. With the MOT light taking up the majority of the optical access, this method was not an option. We chose to have a system where the atoms fell through an on-resonant beam configured into a thin "light sheet". A photodiode was used to measure the light absorbed by the atoms as they fell through the beam.

The TOF light in Fig. 3.3 was taken from a beamsplitter (BS) after the slave AOM. The light passed through a shutter and a polarizing beam splitting cube (PBSC), before being coupled through an optical fiber. As shown in Fig. 3.13, the TOF light exited the fiber on the optical table with the vacuum chamber and passed through a PBSC, a half waveplate (HWP), and was reflected off another PBSC before entering the vacuum chamber. The HWP was set to provide 80 μW of power reflecting from the PBSC. The beam then entered a cylindrical lens pair which expanded the beam dimensions to a size of 6 mm wide by 1.5 mm high. With these beam dimensions and 80 μW of power, the intensity of the TOF beam on the atoms was 0.8 mW/cm^2 or about half the saturation intensity I_s. This prevented saturation and consequently improved the signal to noise ratio. The TOF light passed through a QWP to circularly polarize the light and was retroreflected onto the signal photodiode to maximize the amount of absorption and to prevent the atoms from being pushed aside as would occur with a single beam. A reference TOF signal passed through the PBSC, shown at the top of Fig. 3.13, and into the reference photodiode. The reference and signal photodiode voltages were sent to a differential circuit which subtracted the two voltages. The output of the differential circuit provided input to an EG&G lock-in amplifier. The lock-in amplifier increased the signal to noise ratio by only measuring the signal in a narrow bandwidth around a certain modulation frequency. The reference for the lock-in was provided by a 4 kHz sine wave dither on the secondary slave AOM. The dither signal was added to the constant DC voltage applied to the AOM driver. The output from the lock-in amplifier was read into the computer via one of the PCI-6023E AI's and a temperature was then calculated using the width of the TOF absorption signal. The temperature of the atoms was found

using the full width at half maximum (FWHM) of a gaussian fit to the absorption signal and calculated by,

$$T = \frac{\sigma_t^2 g^2 m}{k_B} \tag{3.2}$$

Where g is the Earth's gravitational acceleration, m is the atom's mass, and σ_t is the standard deviation of the time. In deriving this equation, we assumed that the atomic cloud was in thermal equilibrium and hence had a gaussian velocity distribution. The relationship between the standard deviation of the velocity distribution and the observed temporal signal was $\sigma_v = \sigma_t g$. Therefore we could find σ_v by simply fitting a gaussian function of the form $ft = Ae^{-(t-t_0)^2/2\sigma_t^2}$ to the TOF peak. Figure 3.14 shows a typical TOF absorption signal.

Due to the short pulse duration of the pulses, it was very important to have the pulsed light focused at the pulsing AOM to achieve the fastest possible switch on/off time. The pulse lengths used in the experiment were on the order of a 1 μs, so that the AOM needed to turn on in a duration considerably faster. We found with a beam diameter of 1 mm that the AOM's rise time was about 300 ns. While this was faster than the typical pulse length, it resulted in very poor data. By focusing the beam diameter to <0.5 mm, a rise time of 90 ns was seen, producing much better data. The pulsing AOM's cover was removed for two purposes: firstly, it allowed for more heat to dissipate (therefore a more stable pulse and better efficiency), and secondly a 5-10% increase in efficiency was noted with the beam centered along the crystal's width. The AOM manufacturers machined an aperture in the cover that placed the beam as close as possible to the radio frequency (RF) applied to the crystal (near the crystal's edge).

The pulsed light in Fig. 3.3 was comprised of the zeroth order light from the primary slave AOM. This light passed through a $f = 250$ mm lens in order to focus the beam at the center of the pulsing AOM. The zeroth and first order AOM beams exited the pulsing AOM and passed through another $f = 250$ mm lens. The zeroth order beam was then blocked and the first order beam passed through a half waveplate

(HWP). The HWP was adjusted such that all of the first order pulsed light was reflected off of the TOF PBSC. The pulsed light (with a power of 60 mW) was coupled through the same fiber as the TOF light. The light then exited the fiber onto the optical table with the vacuum chamber (as shown in Fig. 3.13) with 35 mW of power, reflected from a PBSC, and the finally had its diameter doubled (using a beam expander) to a size of 1.5 mm. The light entered the chamber near vertically by reflecting off of the lower vertical MOT beam mirror. It was then retroreflected to create the standing wave. The angle of the pulsed beam to the vertical was set to a minimum by placing the pulsed beams retroreflecting mirror as close as possible to the vertical MOT beam's retroreflecting mirror as shown in Fig. 3.11.

3.4.5 Magnetic Coils

In section 2.2, we discussed the possible trapping effect of a magnetic field on the atoms. Since the MOT was the basis of the experiment we had to build a set of current carrying coils to perform this function. These coils were to be placed near the vacuum chamber and dissipated a considerable amount of power. Thus their effect on the temperature of the chamber had to be taken into account. Although the coils had to produce only a modest field gradient of about 10 Gauss/cm, because of their small diameter a high current was required.

The coils were 3 inches in diameter, had 150 turns of wire per coil, and were setup in a near anti-Helmholtz configuration (the separation between the coils equals the diameter of the coils) as shown in Fig. 3.15. The coils were centered on opposite sides of the cube (as shown in Fig. 3.12) and attached to the cube by thin metal strips. The only contact between the coils and the cube was through the strips. The strips allowed the coils to dissipate heat to the cube and provided good structural support. The main coil DC power supply provided 10 Amps to the coils and produced an inhomogenous magnetic field with a gradient of 20 Gauss/cm with a zero field in the center. Since the main coils had to be turned off and on during the experiment, a

solid state relay (SSR) was installed on the output of the power supply. This gave us the ability to switch the main coils by applying a TTL pulse through the PCI-6711 DO's to the SSR.

Three pairs of nulling coils were positioned on all six sides of the trapping chamber to counteract the Earth's magnetic field and any stray fields produced by other sources. Each pair was controlled by a different DC power supply. The nulling coils were very important in the cooling part of the experiment. Adjustment of the nulling coils' current lead to a change in the position of the zero of the magnetic field produced by the main coils. Therefore, the atoms in the trap could be moved in any direction. By taking TOF signals, the temperature was determined and the current in the nulling coils was adjusted for the lowest possible temperature. This was a very sensitive process as even the smallest change in current would increase the temperature by 5 or 10 μK. This was a task that was essential to perform at the start of each day if the coldest atoms possible were to be produced.

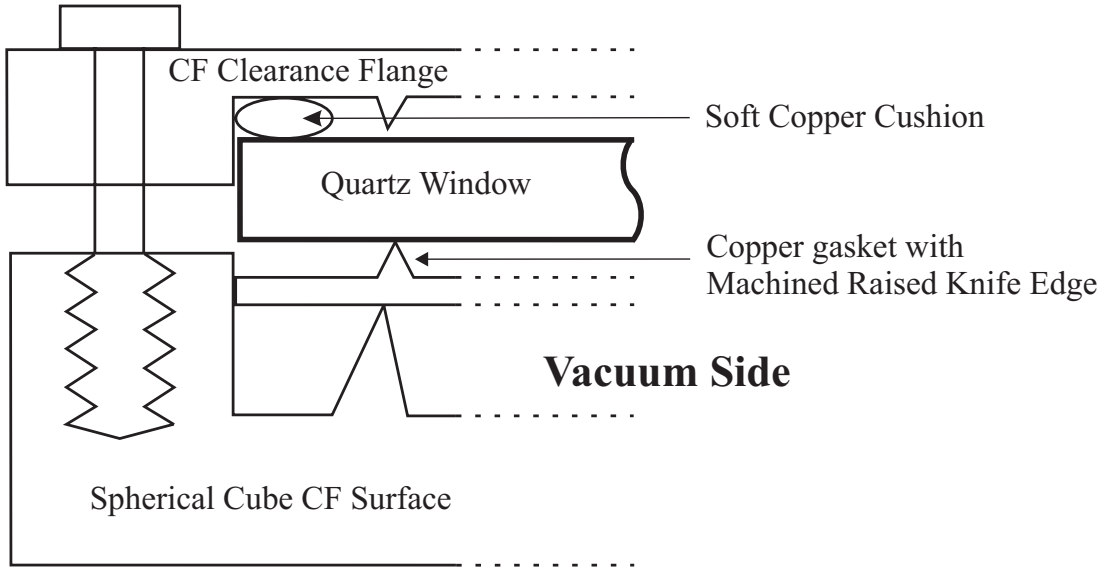

Figure 3.2. A side view of half the viewport vacuum seal. The soft copper cushion provided a gap between the clearance CF flanges' knife edge and the surface of the viewport, thus preventing direct contact with the viewport.

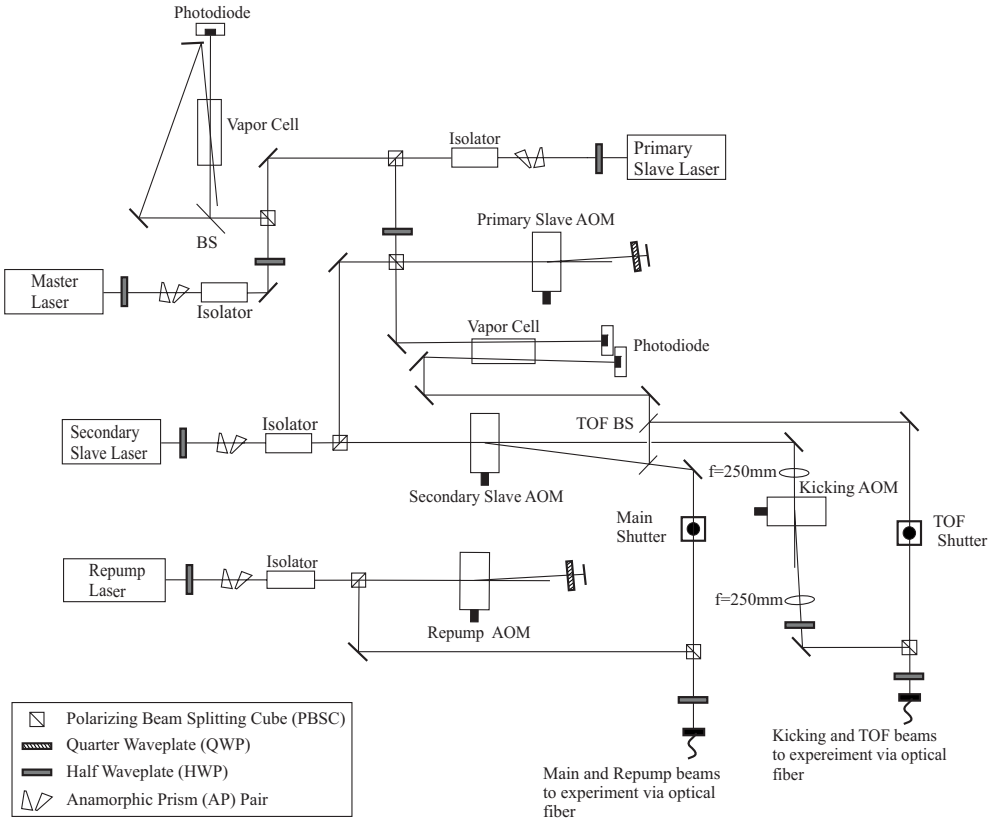

Figure 3.3. Optical table setup of the lasers showing the optical paths for repump, cooling, time of flight (TOF), and pulsed laser light. Each laser's output went through an anamorphic prism (AP) pair to create a circular beam. Also, optical isolators at the laser's output eliminated back reflections to the lasers. All of the beam splitting cubes were polarizing beam splitting cubes (PBSCs). The angles of the first order light from the acousto-optical modulators (AOMs) are exaggerated to show detail. The cooling light and repump light both shared a common PBSC and optical fiber. The TOF light and the pulsed light also shared a common fiber. In both cases the polarizations of the beam were adjusted using quarter waveplates (QWPs) and half waveplates (HWPs).

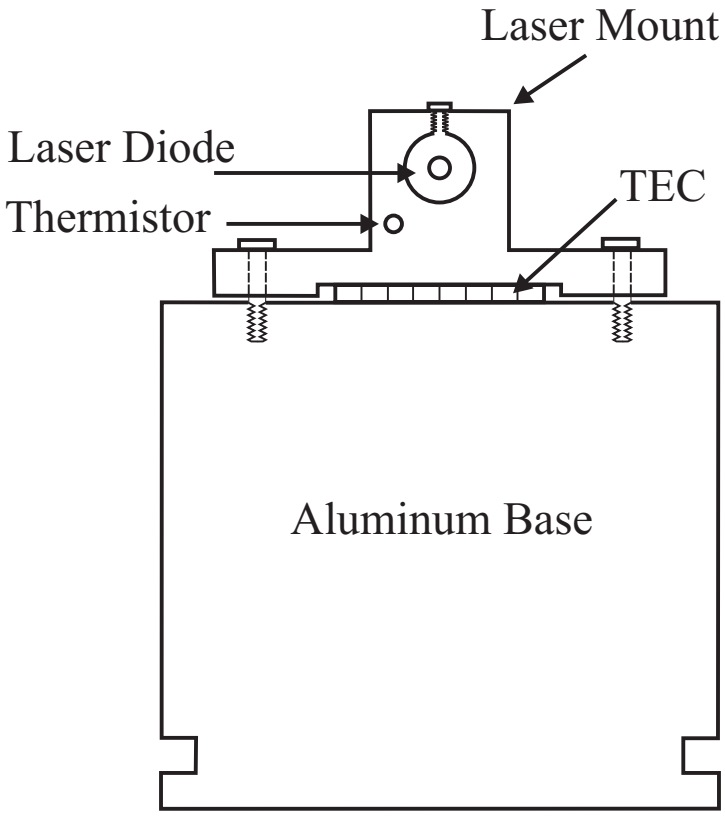

Figure 3.4. Front view of the primary and secondary slave lasers. The laser diode was housed in an aluminum mount and was secured to the aluminum base by Teflon screws. The thermoelectric cooler (TEC) was mounted between the diode housing and the base. The large base provided a heat sink for the TEC as well as a stable platform. A thermistor was installed in the laser diode housing to provide input to the driver for temperature control.

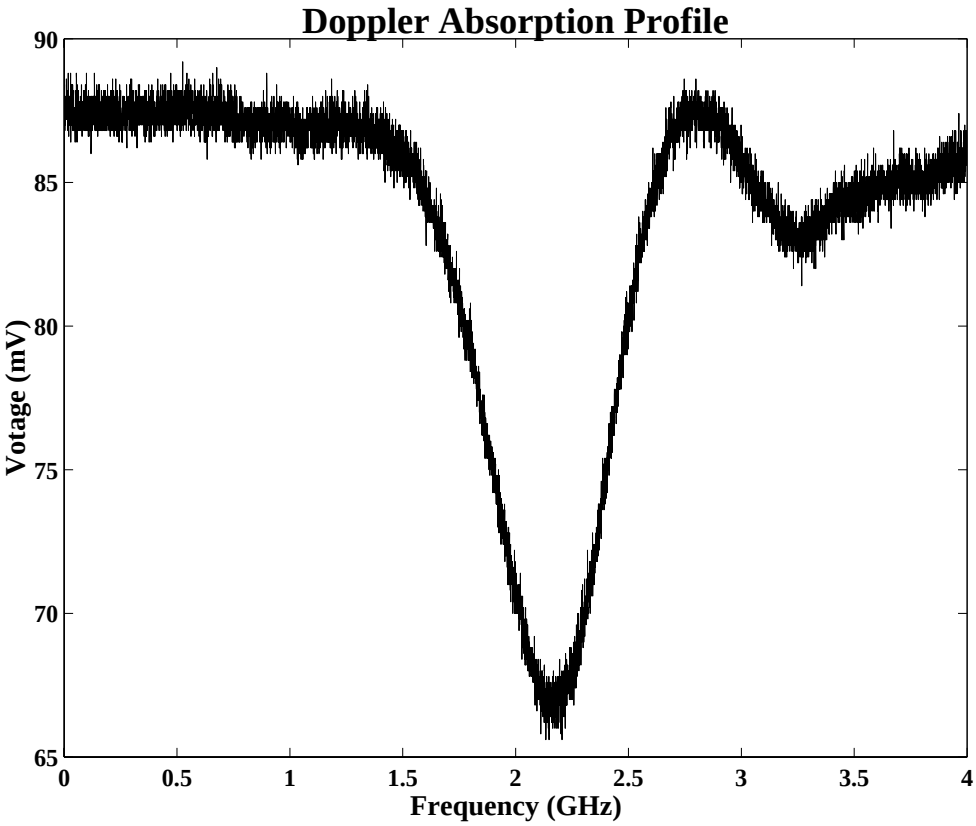

Figure 3.5. The Doppler absorption profile for the slave lasers.

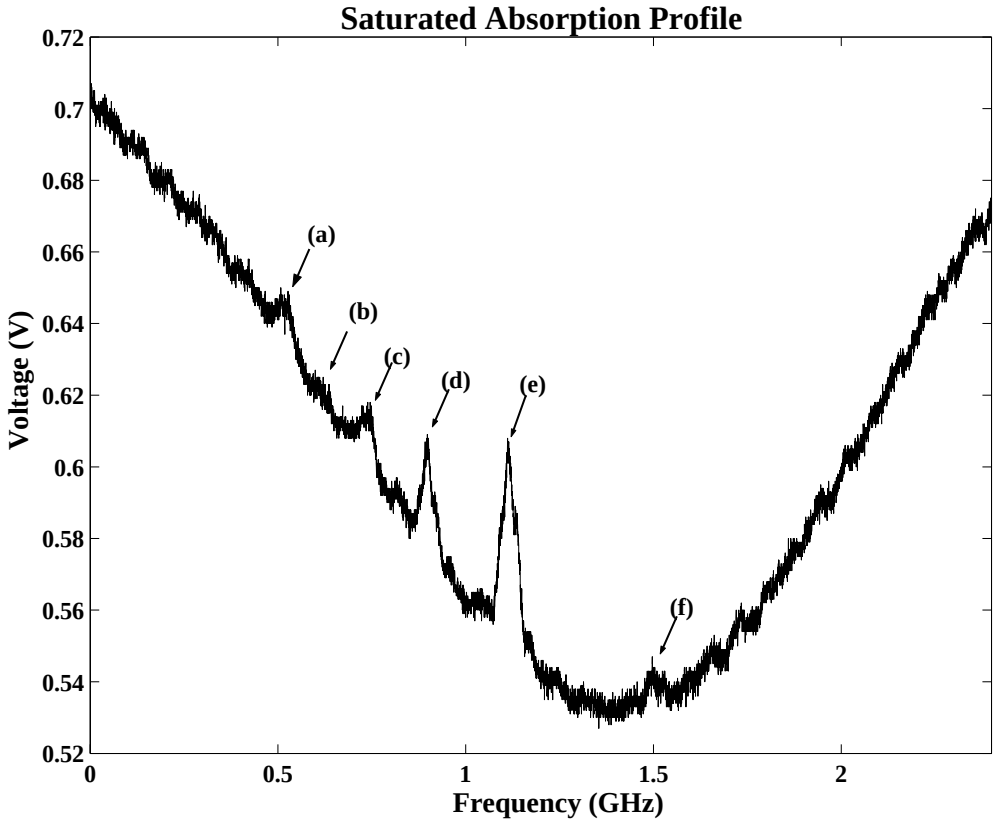

Figure 3.6. Rubidium 87 $F = 2 \rightarrow F' = 3, 2, 1$ saturated absorption lines: (a) $F' = 1$ transition, (b) $F' = 1-2$ crossover, (c) $F' = 2$ transition, (d) $F' = 1-3$ crossover, (e) $F' = 2 - 3$ crossover, and (f) $F' = 3$ transition.

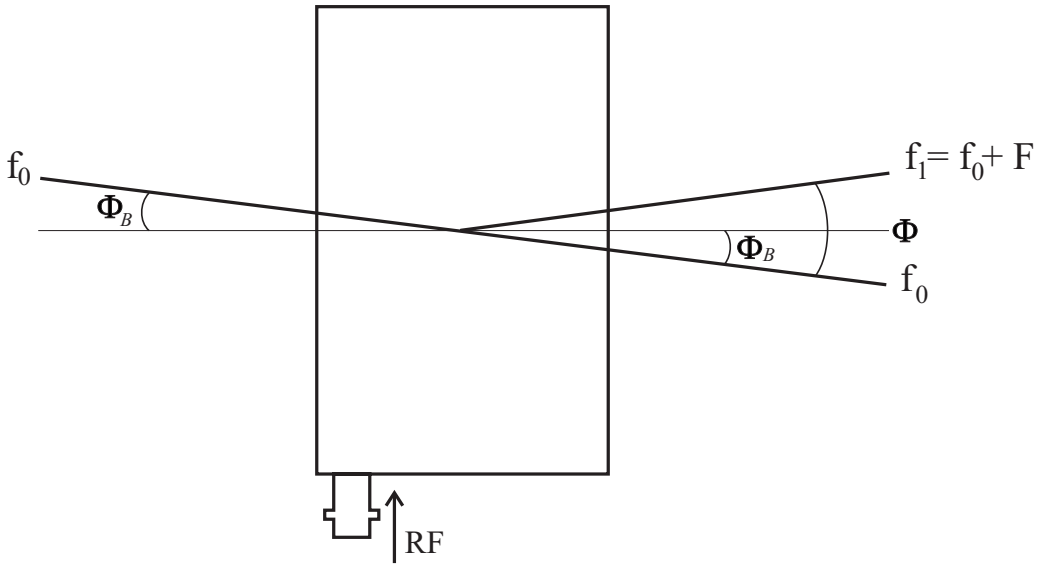

Figure 3.7. The incoming light at frequency, f_0, entered the AOM at the Bragg angle, Φ_B. The acoustic wave velocity was in the direction of the applied radio frequency (RF) wave. The zeroth order light passed through the AOM with its frequency unchanged. The first order light exited the AOM at twice the Bragg angle with a frequency of f_1. The angle was important for achieving efficient diffraction.

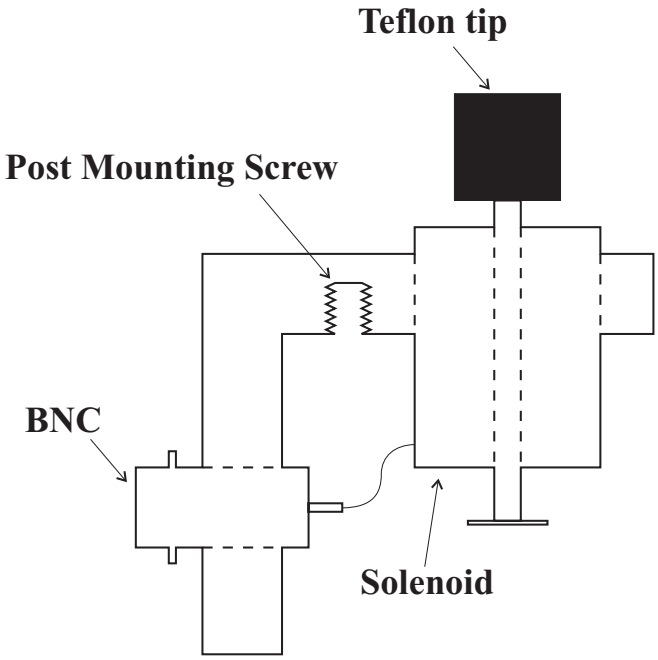

Figure 3.8. The main, TOF, and pulsing shutters were designed to use an off-the-shelf linear plunger type 9 VDC solenoid. A black Teflon tip increased the surface area of the shutter. The shutter electronic circuit is shown in Figure 3.9

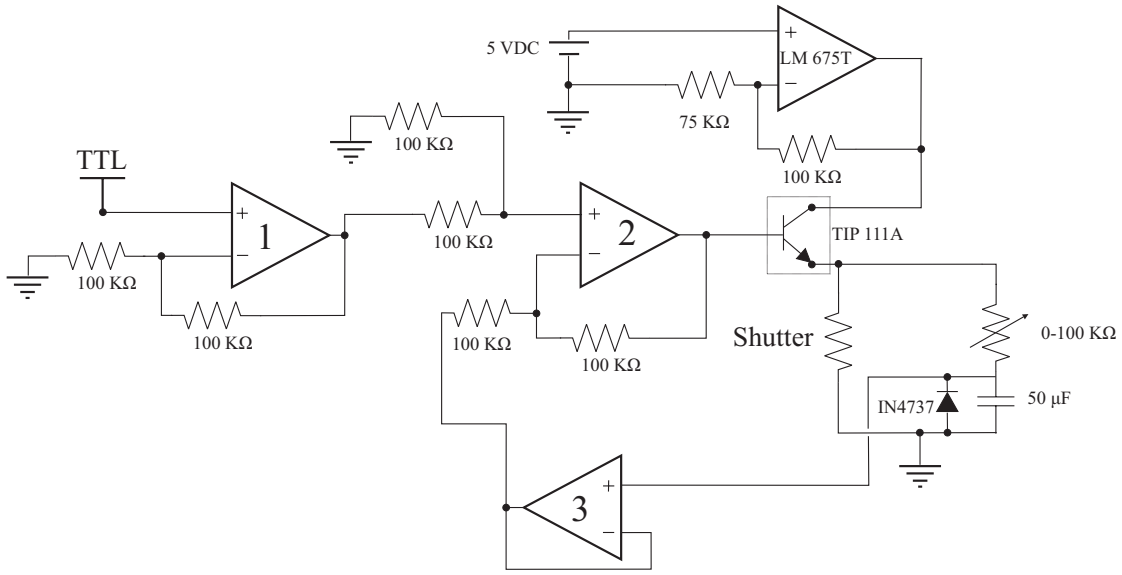

Figure 3.9. Shutter Electronics: The labels 1-3 correspond to components on a TL084 quad operational amplifier (op-amp). A transistor-transistor logic (TTL) high pulse was sensed at the TIP 111A's base and allowed current to flow from the LM675T to the TIP 111A's collector then through the emitter to power the shutter (here represented as a single resistor).

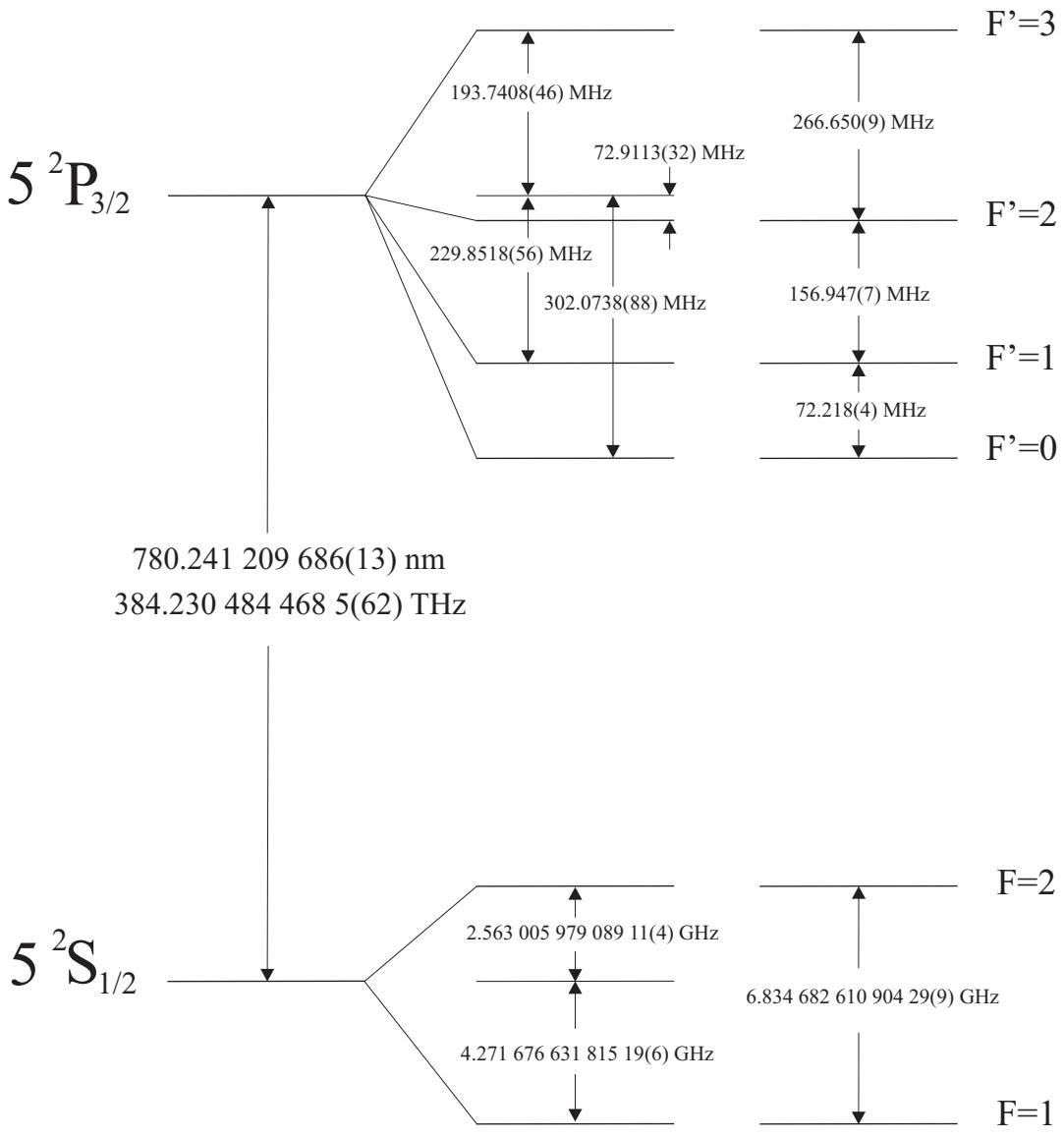

Figure 3.10. Hyperfine splitting of rubidium 87 D2 line[49,50]. The cooling light and pulsed light was on-resonant with $F = 2 \rightarrow F' = 3$ and repump was on-resonant with $F = 1 \rightarrow F = 2'$.

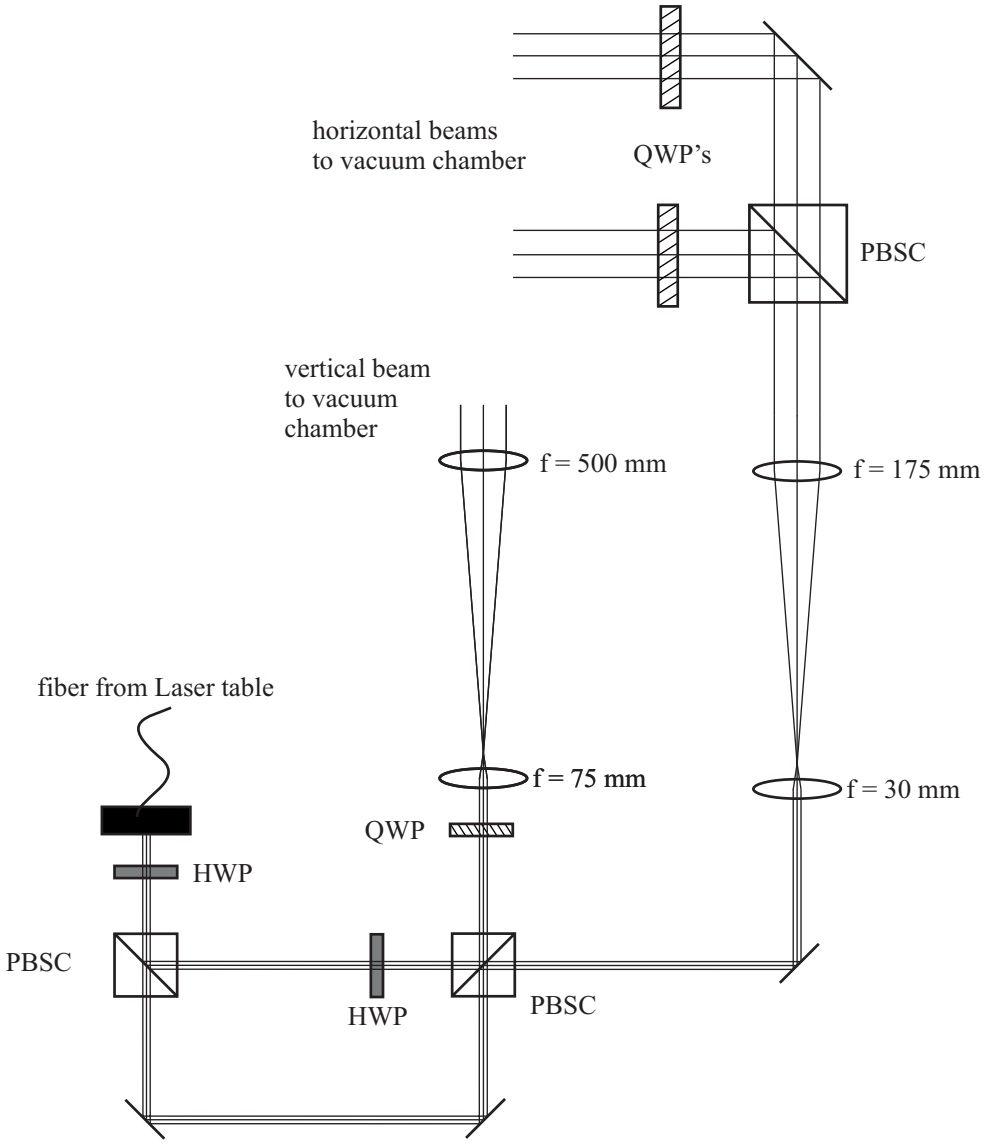

Figure 3.11. Optical arrangement used for creating the trapping beams on the optical table with the vacuum chamber. First, the MOT light exited the fiber from the laser optical table. The MOT beams were then split using the polarizing beam splitting cubes (PBSCs) and were circularly polarized using the quarter waveplates (QWPs). The PBSC after the fiber split off repump light to enter the chamber in the vertical direction.

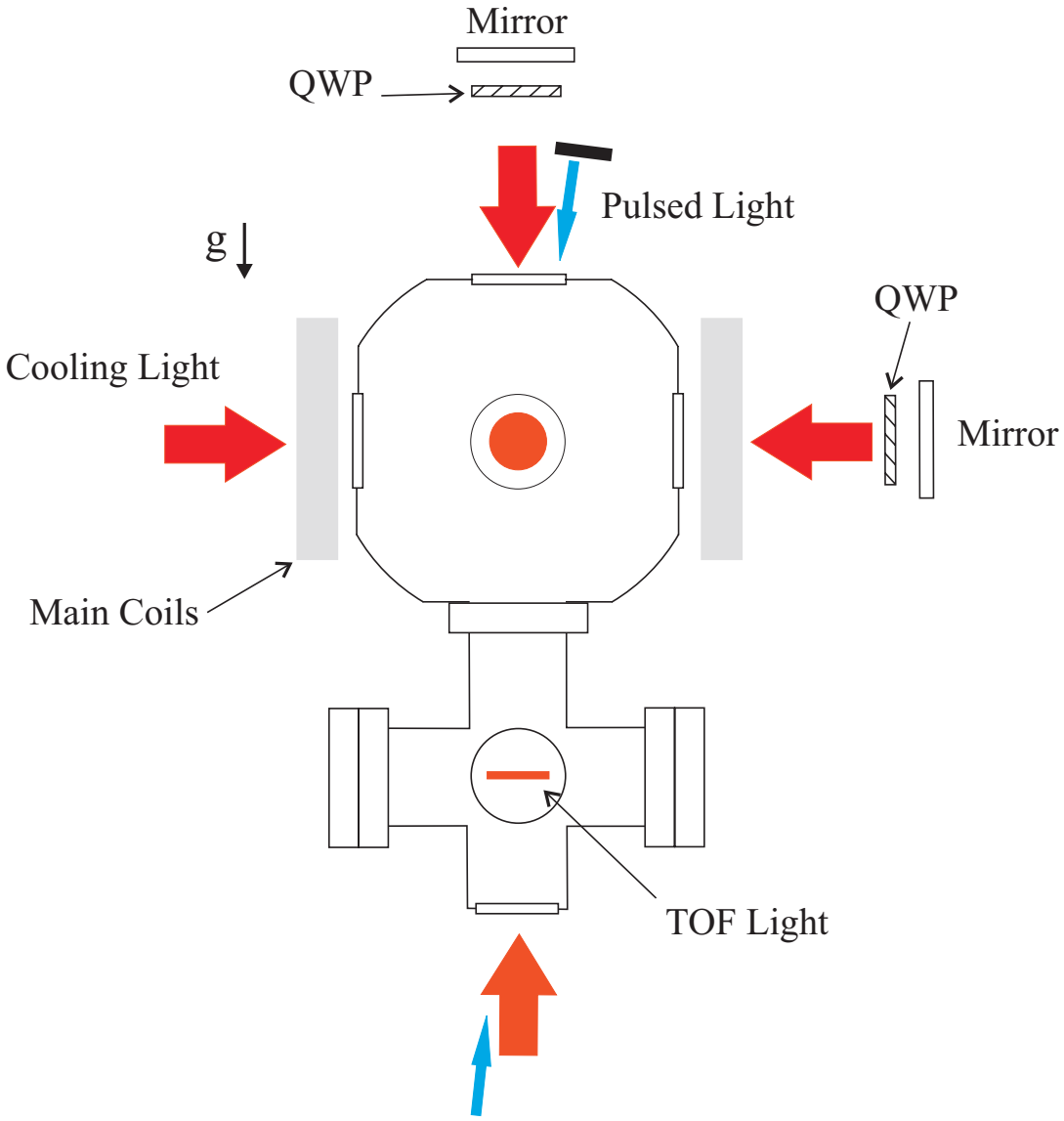

Figure 3.12. A side view of the vacuum chamber. The cooling light beams entered through orthogonal viewports and were retroreflected through quarter waveplates (QWPs). TOF light entered through the bottom viewport and was retroreflected. The pulsed light (blue arrows) entered at a small angle vertically and was retroreflected.

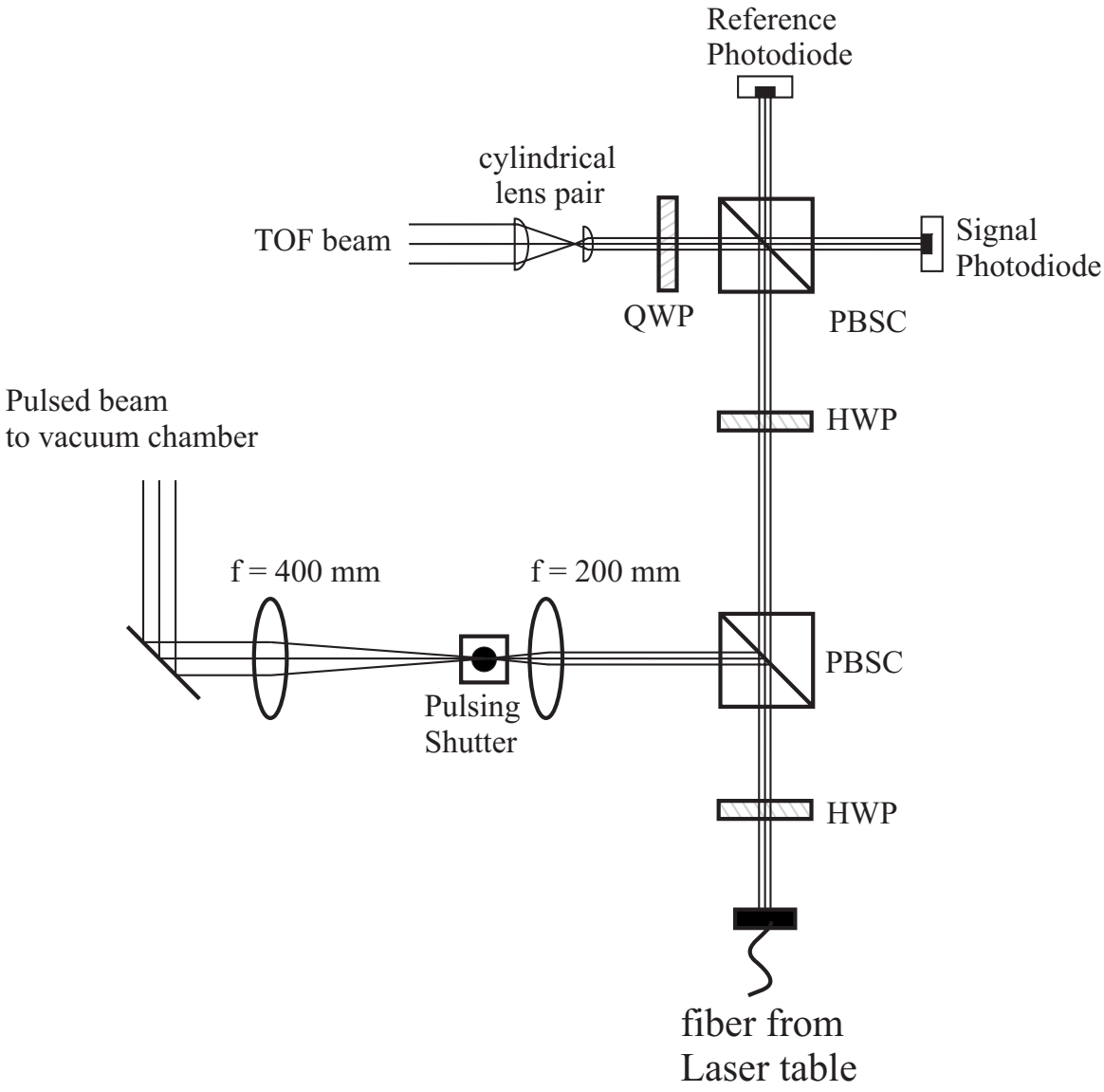

Figure 3.13. TOF and Pulsed light paths to the vacuum chamber. The pulsed light and that portion of TOF light not passing through the polarizing beam splitting cube (PBSC) was focused on the pulsing shutter for a faster closing time and for better beam blockage. The pulsed light was sent through a beam expander and to the vacuum chamber.

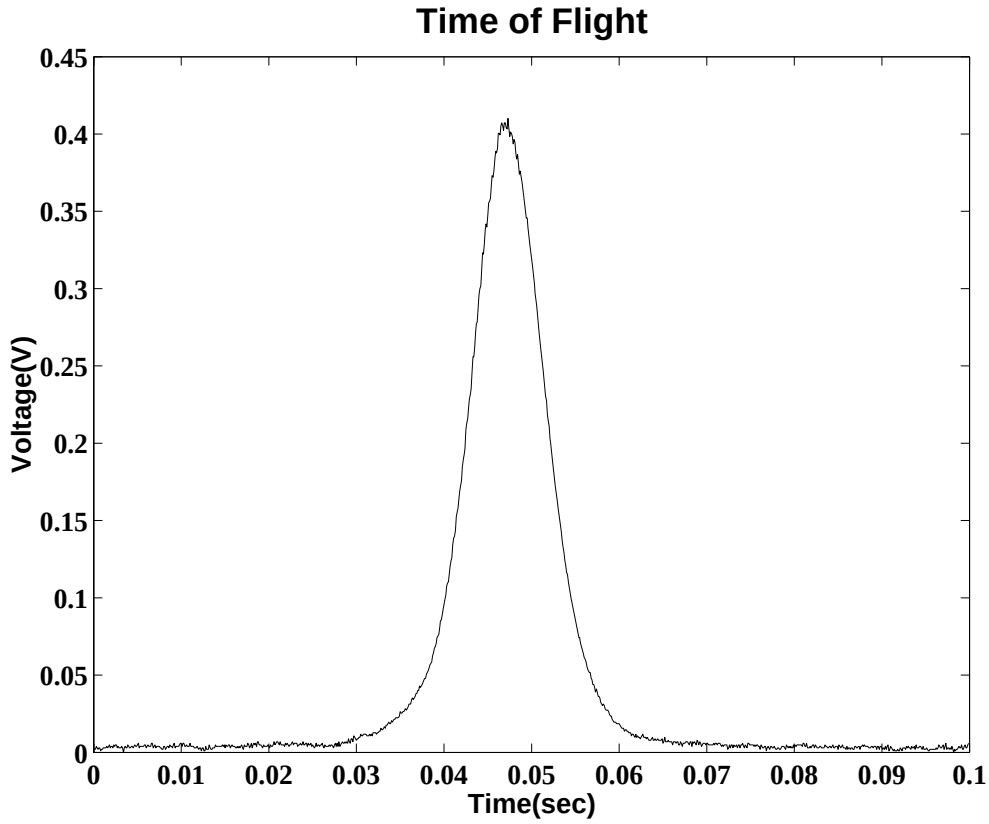

Figure 3.14. TOF absorption signal from the lock-in amplifier. Labview code was written to fit a gaussian to the signal and calculate a temperature. These atoms had a temperature of 15 μK.

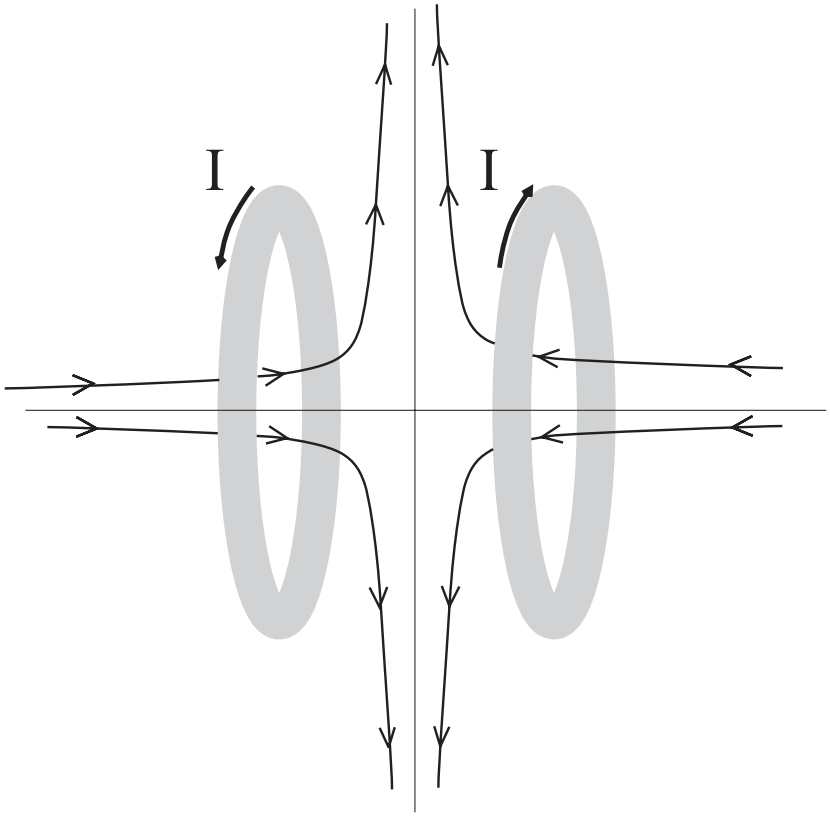

Figure 3.15. The magnetic coil configuration used to create the magnetic field for the MOT. The coils had 150 turns per coil and provided a magnetic field gradient of 20 Gauss/cm with 10 Amps of current. A zero magnetic field was produced at the center due to oppositely flowing current in the two coils.

CHAPTER 4

QUANTUM ACCELERATOR MODES

4.1 Experimental Setup

In this chapter we explain in detail the experiments on kicking rubidium 87 atoms. The theory has already been explored in Chapter 2, so we are now in a position to examine how well this work matches a real system. The experiments done with rubidium 87 are compared and contrasted with previous experiments[26] with cesium 133. As will be seen, there are signifficant differences between the two atomic species. The sample of laser cooled rubidium 87 atoms needed for the experiment was produced using the methods explained in Chapter 3. The sample of atoms was suspended in a MOT, released by switching off the magnetic field, and then kicked with pulses of off-resonant light. A time line of the experiments is given in Fig. 4.1 and a detailed explanation of the Labview code to perform these functions is given in Appendix A.

To commence an experiment the magnetic coils were turned off and the atoms were placed in an optical molasses. To allow for further cooling, the primary slave AOM was adjusted to provide cooling light at -70 MHz detuning. During this cooling stage, the amount of light was reduced by adjusting the secondary slave AOM's frequency to 91 MHz in order to misalign the light with the fiber. After an 18 ms cooling period, the repump light intensity was set to zero by switching off the repump AOM driver with the cooling light staying on for an additional 5 ms. With no repump light the atoms decayed into the $F = 1$ ground state, the state required for the kicking experiments. Once the MOT light was turned off the atoms began to

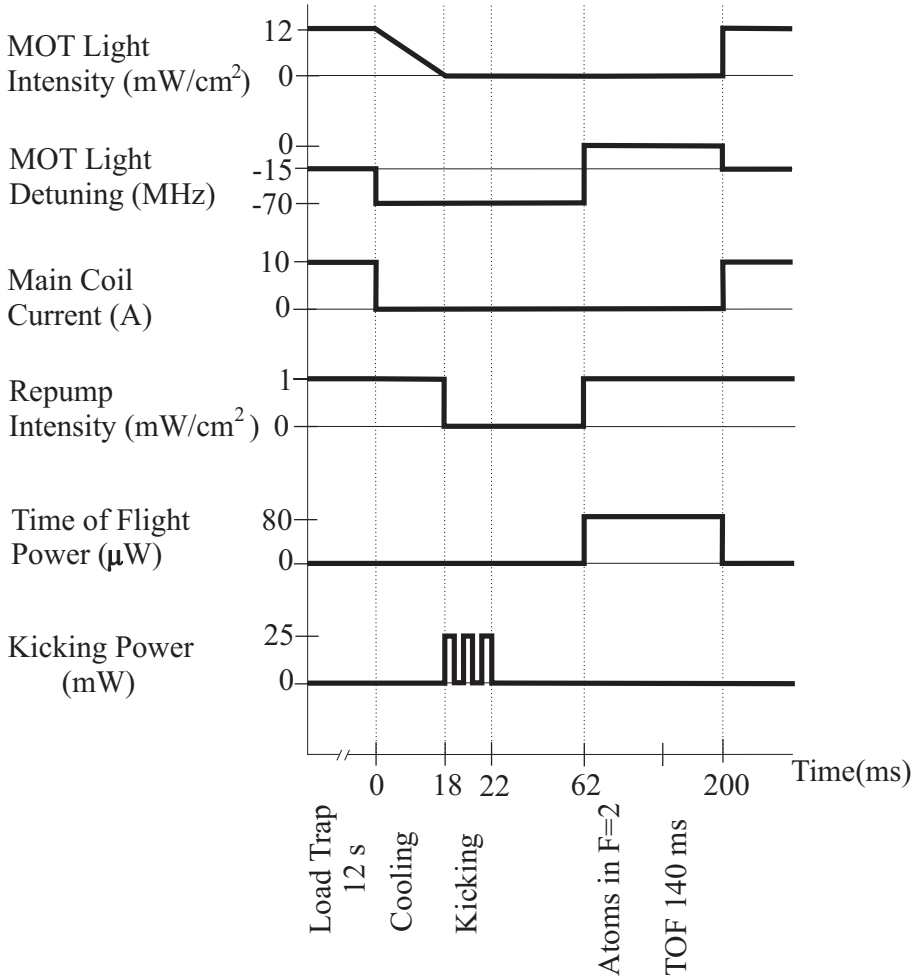

Figure 4.1. Time line showing the values of the parameters important for a successful kicking experiment.

fall. The pulsed light frequency was on-resonant with the D2 line $F = 2 \rightarrow F' = 3$ transition. Therefore, the pulsed light was detuned by 6.8 GHz for atoms in the $F = 1$ ground state. At this point several different experiments were performed (which will be described shortly) by adjusting the pulsing parameters programmed into the arbitrary waveform generator. After the atoms received the pulses, repump light was turned on so as to optically pump the atoms into the $F = 2$ level so that they could absorb the TOF light. The repump light, as stated earlier, was directed into the vacuum chamber in the vertical direction. This made it possible to optically pump the atoms into the $F = 2$ state, since in any other configuration the atoms would have fallen out of the region where the light was present.

The major parameters changed during the experiments were number of pulses, time between pulses, polarization, pulse length, and pulsed beam diameter. By changing the number of pulses, it was possible to observe the momentum gained with each pulse and verify the predicted linear increase in momentum with pulse number. Changing the time between pulses across the half-Talbot time and the Talbot time gave us a view of the dynamics across a resonance and allowed us to resolve the details set out in the theory in Chapter 2. Polarization effects were examined through circularly polarizing the pulsed beam and then scanning across the time between pulses across the resonances. The pulse length and pulsed beam diameter were varied to change ϕ_d. The role of ϕ_d was to determine the relative population of the diffraction orders as can be seen in Eq. (2.39).

4.1.1 Changing Number of Pulses

In this experiment, we changed the number of pulses and kept all other parameters (time between pulses, power, and pulse length) constant. A linear increase in the atoms' momentum can be seen as a linear trace with positive momentum at an angle to the bulk thermal cloud referenced at zero momentum in Fig. 4.2. This characteristic is indicative of a QAM. The plot in the lower left corner of Fig. 4.2 is

one slice of the color plot. The pulsed beam power was approximately 25 mW with a 1/e beam diameter of 1.5 mm. Using Eq. (2.38) and 0.6 μs for the pulse length gives ϕ_d=2.2. At each value of the pulse number ten shots were taken and averaged in order to improve signal to noise. A TOF absorption profile for the experiment with 61 pulses is shown in the lower left corner of Fig. 4.2. The profile has been rotated 90 degrees clockwise with respect to the actual absorption profile seen on the computer. Thus, time is on the vertical axis and voltage is on the horizontal. The QAM's with positive/negative momentum were those reaching the TOF absorption beam before/after the bulk atoms referenced at zero momentum. That is, all of the figures presented in this chapter plot momentum measured relative to a freely falling reference frame. As we see in Fig. 4.2 not all of the atoms were accelerated. This was due to the initial velocity condition as discussed in Chapter 2.

4.1.2 Changing Time between Pulses

The time between pulses was scanned across the Talbot time and half-Talbot time resonances. Figure 4.3 shows an experimental scan across the half-Talbot time at 33 μs with ϕ_d=2.2 and the number of pulses equal to 60. A comparison of Fig. 4.3 with the phase model presented in Fig. 2.4 shows similarities for the momentum of the accelerator modes. Figure 4.4 shows a numerical simulation using the same parameters as found in the experiments of Fig. 4.3. The theoretical data was created by applying the Bessel function Eq. (2.39) with a $\phi_d = 2.2$ and 60 pulses to an initial gaussian distribution of atoms. The white trace in Figs. 4.3 and 4.4 was generated from the ϵ-classical theory Eq. (2.61) for (1,0) QAMs. Similarities exist between the theory and the experiment such as the momentum gain in the QAMs. The experimental data shows a smaller number of negative momentum QAM's, something that is also seen in the theoretical scan. The secondary jets centered closer to the half-Talbot resonance in Figs. 4.3 and 4.4 were higher order accelerator modes which were explained through the ϵ-classical theory in Chapter 2 and are described below.

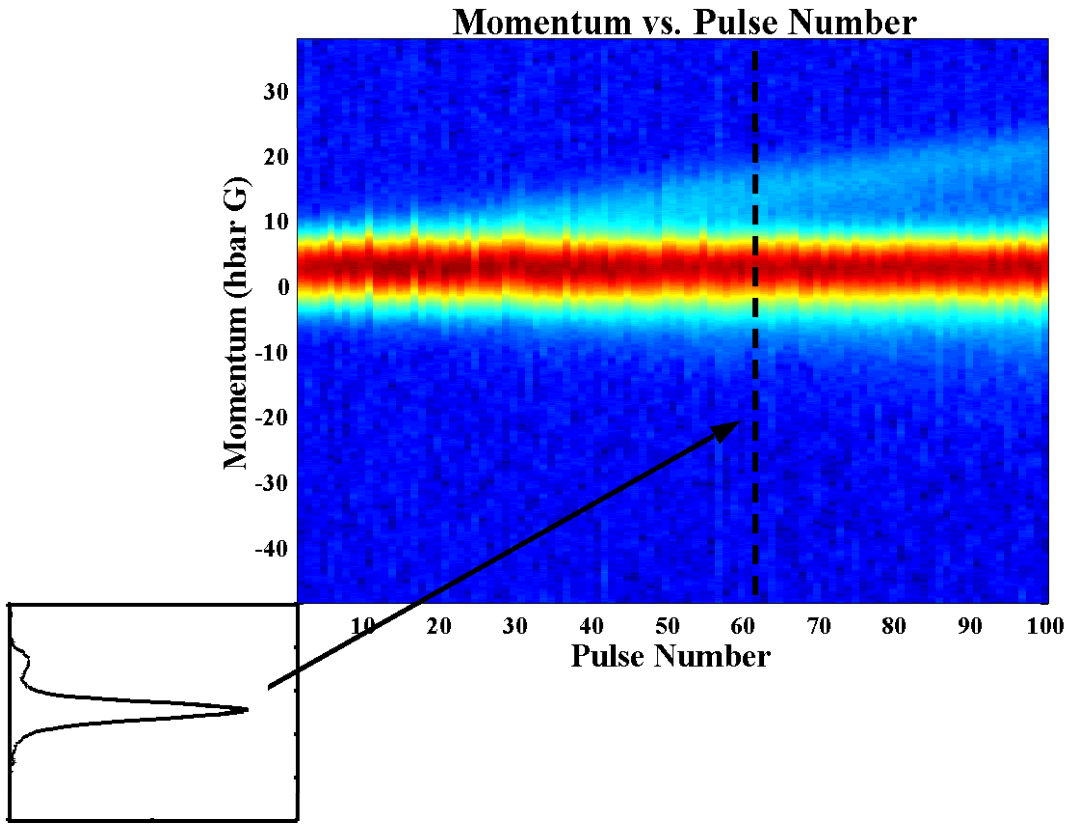

Figure 4.2. Experimental momentum distributions obtained by changing the number of pulses in 1 pulse increments where the vertical dashed line represents a single experiment performed with 61 pulses as shown by the absorption profile in the lower left corner of the figure. The time between pulses was 29.5 μs and ϕ_d was 2.2

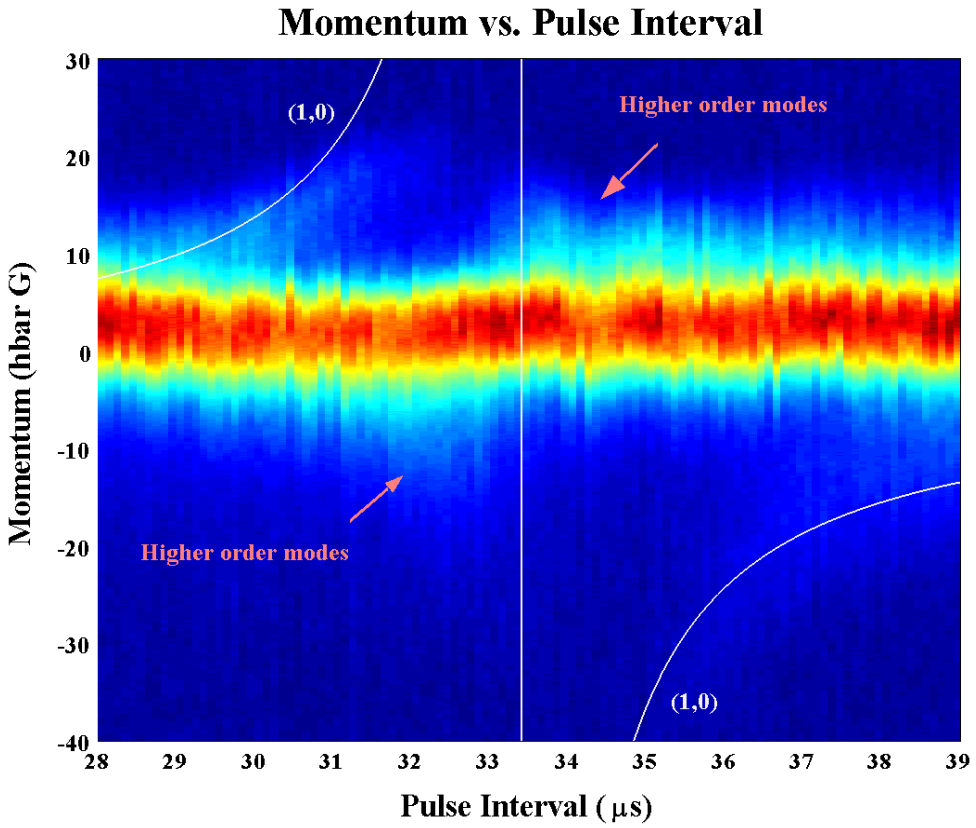

Figure 4.3. Experimental momentum distributions as a function of the pulse interval with an ϵ-classical fit. The half-Talbot time is located at approximately 33 μs. The white curve is the (1,0) accelerator mode from Eq. (2.61) and the vertical white line is the half-Talbot time. The data was obtained using 60 pulses and ϕ_d=2.2.

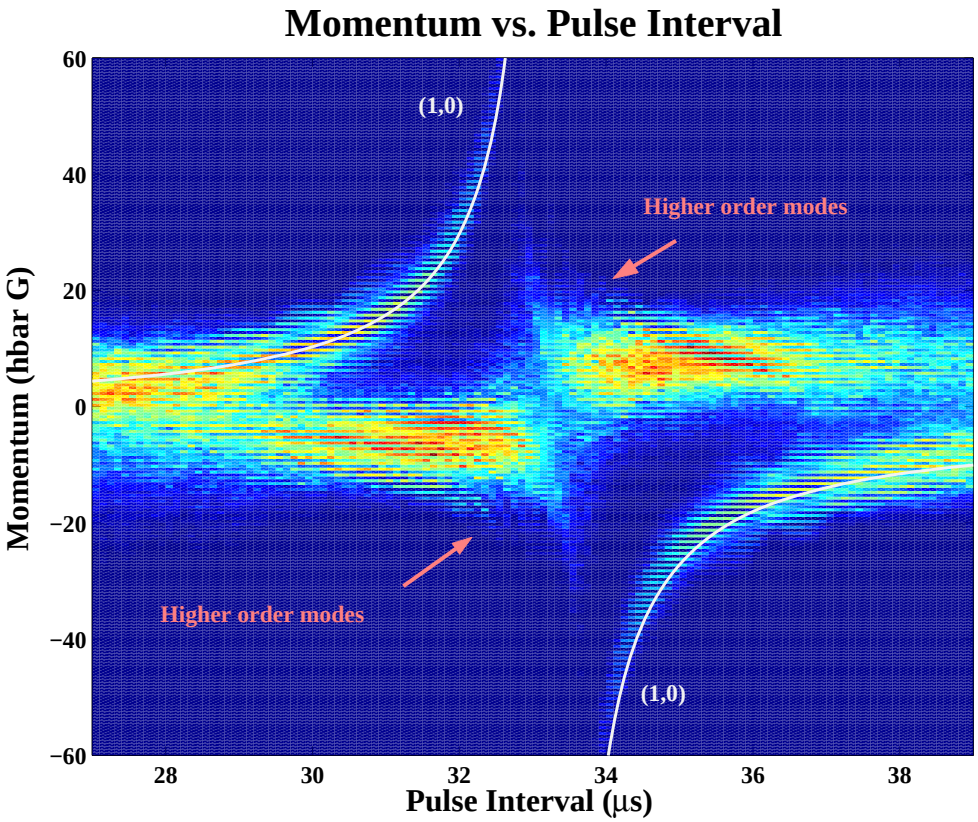

Figure 4.4. Theoretical result of changing the pulse interval, with 60 pulses and ϕ_d=2.2. The theoretical data was obtained by iterating Eq. (2.39). The white curve is the (1,0) accelerator mode from Eq. (2.61).

One significant difference between the experiment and theory was that the density of accelerated atoms in the theory was higher than in the experiment. This could be due to a smaller number of atoms meeting the initial velocity condition in the experiment. Also, the pulsed beam size was about the same size as the atoms. This lead to a larger gradient of ϕ_d over the atoms, and the likelyhood that a significant number of atoms experienced an insufficient ϕ_d.

This experiment could be used as an atomic beamsplitter making up the first part of an atom interferometer[15] as shown in Fig. 4.5. This is an important part of the interferometer. If the atoms are given a large spatial splitting (separation angle) with a beamsplitter, a large area enclosed by the interferometer arms could be created. The phase shift caused by an acceleration is proportional to the area enclosed by the arms of an atom interferometer and for a rotation is given by[15],

$$\Phi_{rot} = \frac{2m}{\hbar}\mathbf{A} \cdot \Omega, \tag{4.1}$$

where m is the atomic mass of the atom, A is the area enclosed by the arms of the interferometer, and Ω is the rotation rate of the interferometer in the plane of the interferometer. Thus, a larger area would produce a larger phase shift in Eq. (4.1) and ultimately improve the sensitivity of an atom interferometer to such phase shifts. The QAM's described in this thesis have the ability to produce a large spatial splitting depending on the number of pulses. As an example, we can provide approximately 3 mm spatial splitting with a momentum of 25 $\hbar$G per Fig. 4.3. One type of atom interferometer in use at MIT[51] uses atomic beam diffraction from 3 200-nm-period gratings[52] for the mirrors and beamsplitters. The spatial splitting is inversely proportional to the grating period. Thus, the spatial splitting is small and the area is made large by a large separation of the gratings. Another type of atom interferometer is a fountain type[53] and uses 3 pulses of light separated by a certain time. This only delivers $2\hbar k$ units of momentum in the initial pulse and the remaining pulses are applied at specific time intervals to complete the area of the interferometer.

Quantum accelerator modes in our theoretical scans can deliver as much as 60 $\hbar G$ units of momentum, thus presenting the possibility of a very large spatial splitting.

With the addition of another acousto-optical modulator the standing wave could be accelerated and one could relate the total acceleration (Earth's gravitational acceleration plus standing wave acceleration) to h/m by manipulating Eq. (2.56) and (2.57). The resulting equation is

$$\frac{j}{p} = \frac{2\pi\eta}{\tau} \tag{4.2}$$

and can be rewritten as

$$g_{tot} = (\frac{h}{m})^2(\frac{j}{p})(\frac{1}{\lambda_{spat}}), \tag{4.3}$$

where g_{tot} is the total acceleration. The total acceleration can be tuned to make Eq. (4.3) an equality for a known j and p accelerator mode, the standing wave acceleration can be subtracted out to find the gravitational acceleration. This type of experiment was performed with cesium 133[54] by kicking a thermal cloud of cesium atoms (similar to the experiments in this thesis) with the retroreflecting pulsed beam passing through a crystal phase modulator to shift its phase. This enabled the creation an accelerated standing wave with respect to the atoms. For example, if the modulator was adjusted to provide a standing wave acceleration equal in magnitude but opposite in direction to the Earth's gravity, quantum accelerator modes would cease to exist[25]. The authors of the gravity measurement experiment[54] concluded that the precision of the experiment could be greatly improved by controlling the frequency difference of the two retroreflecting beams. This could easily be done in the laser cooling vacuum chamber by splitting the pulsed beam, passing each component through an independent, frequency adjustable acousto-optical modulator, and directing the beams so that they counterpropagated through the vacuum chamber. This is one possible direction for the OSU experiment.

Figure 4.6 shows a scan across the Talbot time. In this case even less atoms contribute to the major accelerator modes. This may be due to the vibrations in the vertical pulsed beam mirrors. This could cause a loss of phase coherence and thus

a loss of accelerator modes. Also, since the pulsed beam was at an angle and the atoms fell further during an experiment conducted at the Talbot time some of the atoms failed to see a pulse. This could be prevented by better alignment or making the pulsed beam diameter bigger.

4.1.3 Higher Order Accelerator Modes

The ϵ-classical theory discussed in Chapter 2 labels the QAMs as an *order* ($\mathbf{p}$) and a *jumping index* ($\mathbf{j}$). The experimental data and theory data were fitted by adjusting $\mathbf{p}$ and $\mathbf{j}$ in Eq. (2.61) as shown in Fig. 4.8 and Fig. 4.9. The higher order modes accelerate much slower than the zeroth order. Therefore, we need to look closer to the resonance as shown in Fig. 4.8 and Fig. 4.9 where the rate of momentum change increases.

Experimental and theoretical data is shown in Figs. 4.8 and 4.9 with various curves generated using Eq. (2.61) overlayed. Both sets of data contain the same parameters ($\phi_d = \pi$ and 45 pulses) and were scanned across the same pulse interval. We were able to identify two higher order modes (35,-4) and (8,-1). The other higher order modes were fitted with the theory but were not seen in the experiments. The zeroth order QAMs, (1,0), in the experimental data were not seen in the pulse interval range. This was possibly due to an alignment issue as describe in the previous section.

A phase mapping of Eq. (2.56) is shown in Fig. 4.11 with the same parameters as the experiment and with the time between pulses set to 65 μs. The vertical axis $J_0 = 0$ is the QAM's momentum and the horizontal axis θ_0 is the QAM's displacement along the standing wave. The $(\mathbf{j}, \mathbf{p})$ labels are the known QAM's in the experiment and were found from the stable fixed point (J_0, θ_0). These are stable point islands in a sea of chaos.

We have seen dynamics not explained by the ϵ-classical theory as shown by the jet (labeled (A) in Fig. 4.10) extending out with negative momentum from the bulk cloud referenced at zero momentum. These dynamics were not observed at

Oxford[55] but were hinted at in the theoretical momentum distributions. This was an interesting observation since theory[22] suggests primary resonances close to integer-half multiples of the Talbot time. Other higher order resonances have just started to be investigated in the δ-kicked rotor[27]. This δ-kicked rotor experiment observed the higher order resonances at 3/4 and 1/3 of the Talbot time. In our case the dynamics appear close to 63 μs (Fig. 4.10) which is approximately 3.5 μs before the Talbot time (95% of the Talbot time). This results in a large ϵ of approximately -0.3 as compared to the (35,-4) higher order mode (Fig. 4.10) with an ϵ of -0.06. A recent publication by Bach[28] *et al.* gives some theoretical insight to this type of new QAM dynamics which allows ϵ to be of order unity, although this work is still very preliminary. It is anticipated that our results will give impetus for further developments to theory.

These experiments could prove useful in studying quantum chaos. One possible study is "dynamical tunneling" from one dynamical state to the other. If the system is of a Kolmogorov-Arnold-Moser (KAM)[40] type (KAM dynamics are characterized by the gradual destruction of stable orbits in phase space as the pulse strength is increased), then classically, trajectories remain trapped in the stable islands since they can not move through the KAM boundaries surrounding the stable islands. In Fig. 4.9, we see two higher order modes existing at the same pulse interval of 67 μs. These would correspond to stable fixed points in Fig. 4.11. In the quantum regime the two dynamical states could tunnel from one state to the other. Dynamical tunneling has been observed[56,57] with quantum chaotic systems, but has not probed the quantum-classical boundary because the effective Planck's constant was of the order of unity. With QAMs we can tune the effective Planck's constant ϵ to at least an order of magnitude smaller than previous experiments and thus move closer to the quantum-classical boundary[58].

4.1.4 Polarization Effects

For the theory and experiments discussed to this point, the pulsed light was linear polarized. Polarization can affect atoms in an accelerator mode because there are several different hyperfine sublevels of the ground state $F = 1$ which, in general, interact with the laser light differently. The rubidium 87 D2 line, shown in Fig. 3.10, has three upper levels F'=0,1, and 2 with m_F=-1, 0, and 1 for the ground $F = 1$ state. The pulsed potential will be the sum (weighted by the population) of the light shifts from each of these three magnetic substates. Figures 4.15 and 4.16 show the hyperfine transition strengths for rubidium and cesium[32]. The numbers represent the relative strengths of the transitions and are taken from squaring the dipole matrix operator, $\mu = e\langle e|\hat{\epsilon}\cdot \mathrm{r}|g\rangle$. Recall from Chapter 2 that this is proportional to the light shift. In Fig. 4.13 the top two graphs represent the light shift for linear polarized light for rubidium (left) and cesium (right). Each magnetic sublevel has the same light shift. Therefore all atoms irrespective of their internal state saw the same light shift and hence ϕ_d. In the case of circularly polarized light (bottom two graphs of Fig. 4.13), the sum of the light shifts had different values (or ϕ_d's) for the different magnetic sublevels. The plots in Fig. 4.13 were generated by summing the transition strengths for each ground magnetic sublevel. For example, The $F = 1$ $m_F = -1$ magnetic sublevel has three possible transitions for $F' = 1, 2, 3$ in Fig. 4.15 with transitions strengths 20, 25, and 5 respectively. We sum the strengths and arrive at 50 which is shown in the lower left plot of Fig. 4.13. Figure 4.12 is experimental data for circularly polarized pulsed light across the half Talbot time. The main features in the linear polarized pulsed light in Fig. 4.3 were still seen in Fig. 4.12 but with a lower number of atoms in an accelerator mode. We postulate that this was because the atoms in different sublevels see different ϕ_d's and thus different potential maxima.

These experiments contrasted markedly to those carried out with cesium 133 in Oxford[25]. For cesium, nine different magnetic sublevels of the ground state $F = 4$ the D1 transition, $F = 4 \rightarrow F' = 3, 4$ had two upper levels, $F' = 3$ and $F' =$

4. Figure 4.14 shows the hyperfine splitting of cesium D1 line where the excited state values were taken from Rafac and Tanner[59] and the ground state values are exact[60]. Therefore ϕ_d varied by over a factor of six for atoms in the different substates. Although, QAMs existed, the populations within the different diffraction orders was small for some magnetic substates.

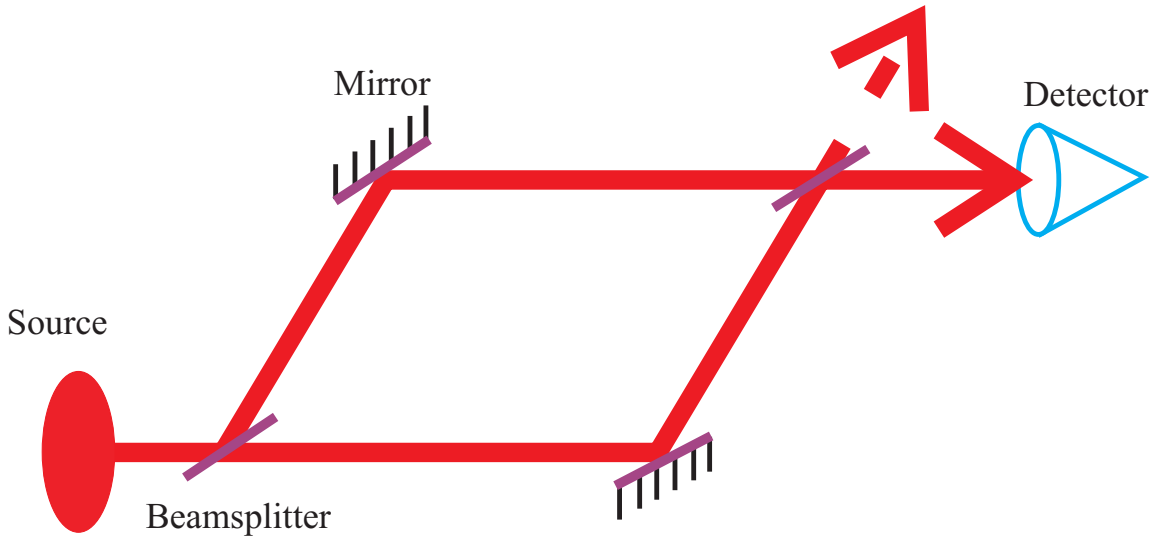

Figure 4.5. Mach-Zehnder[15] type atom interferometer showing the spatial splitting of the atomic source from the grating represented as a beamsplitter in the figure. The two beams reflect from another grating to recombine the two beams at the final grating. The interference pattern is then detected.

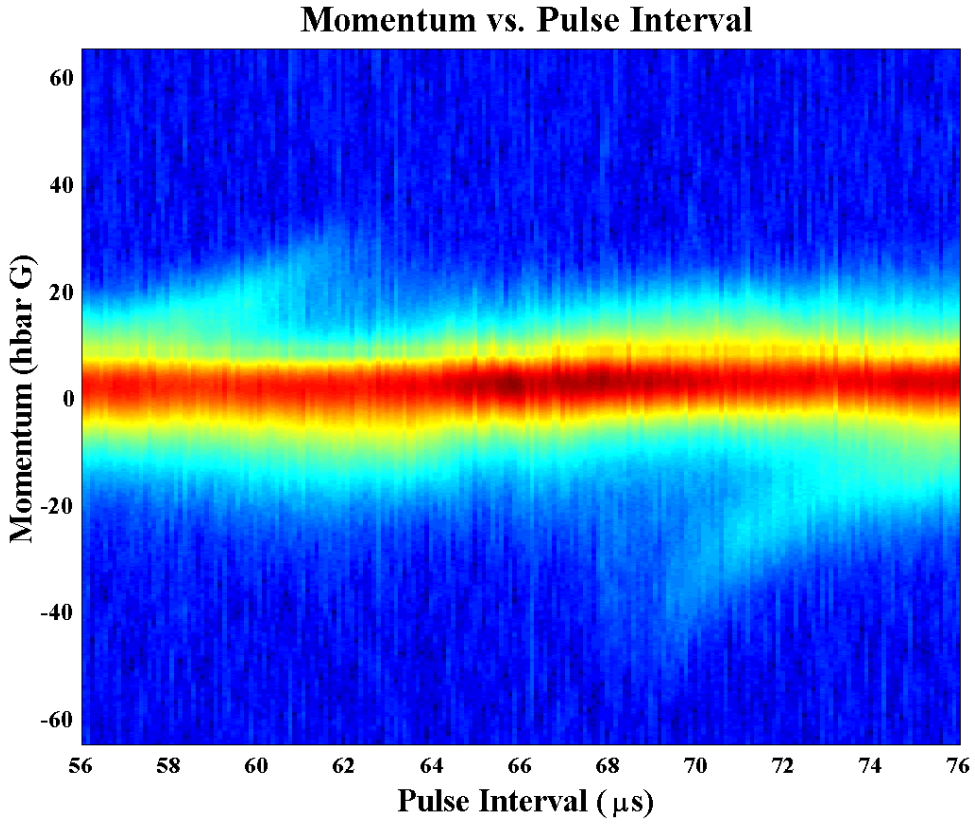

Figure 4.6. Experimental momentum distributions as a function of the pulse interval across the Talbot time, with 30 pulses and $\phi_d=\pi$.

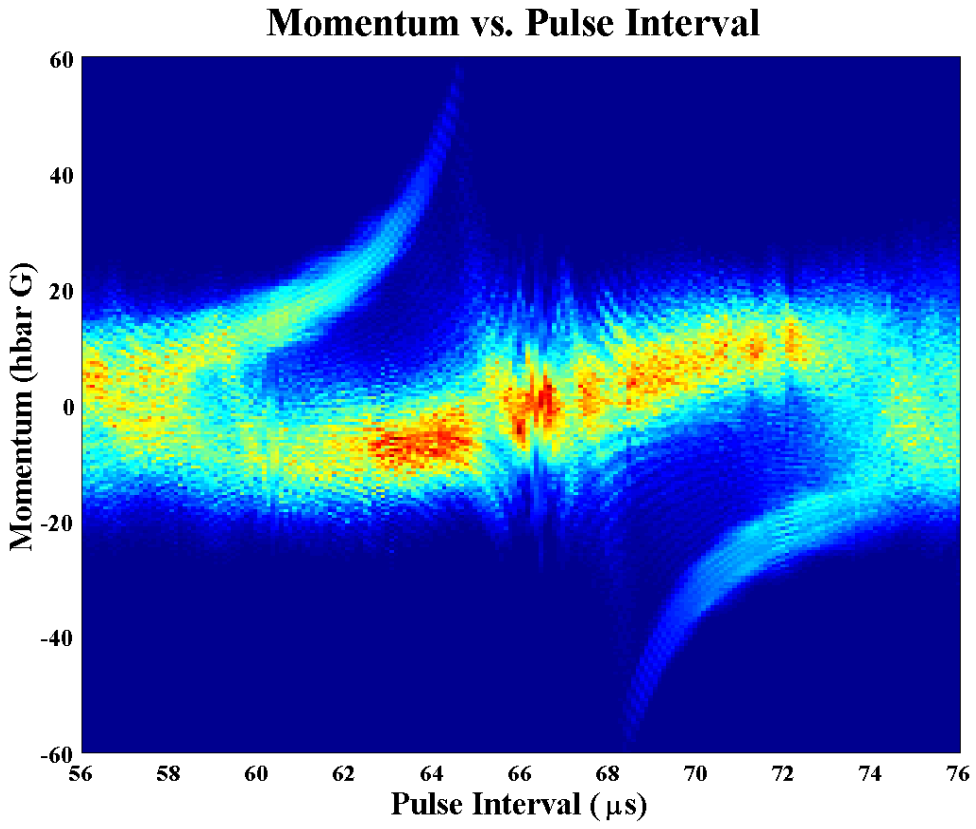

Figure 4.7. Theoretical momentum distributions as a function of the pulse interval across the Talbot time, with 30 pulses and $\phi_d=\pi$. (A) represents dynamics not explained by the ϵ-classical theory.

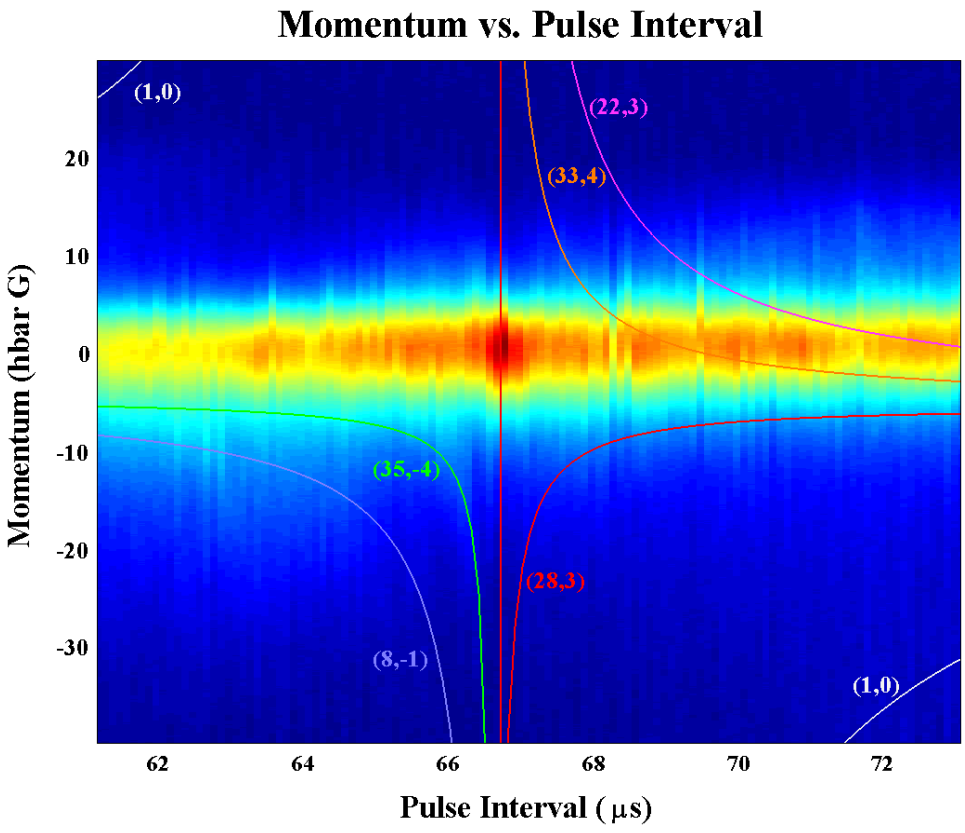

Figure 4.8. Experimental results of changing the pulse interval across the Talbot time, with 45 pulses and $\phi_d=\pi$. The colored curves are Eq. (2.61) and represent the different orders of the QAMs as $(\mathbf{p}, \mathbf{j})$.

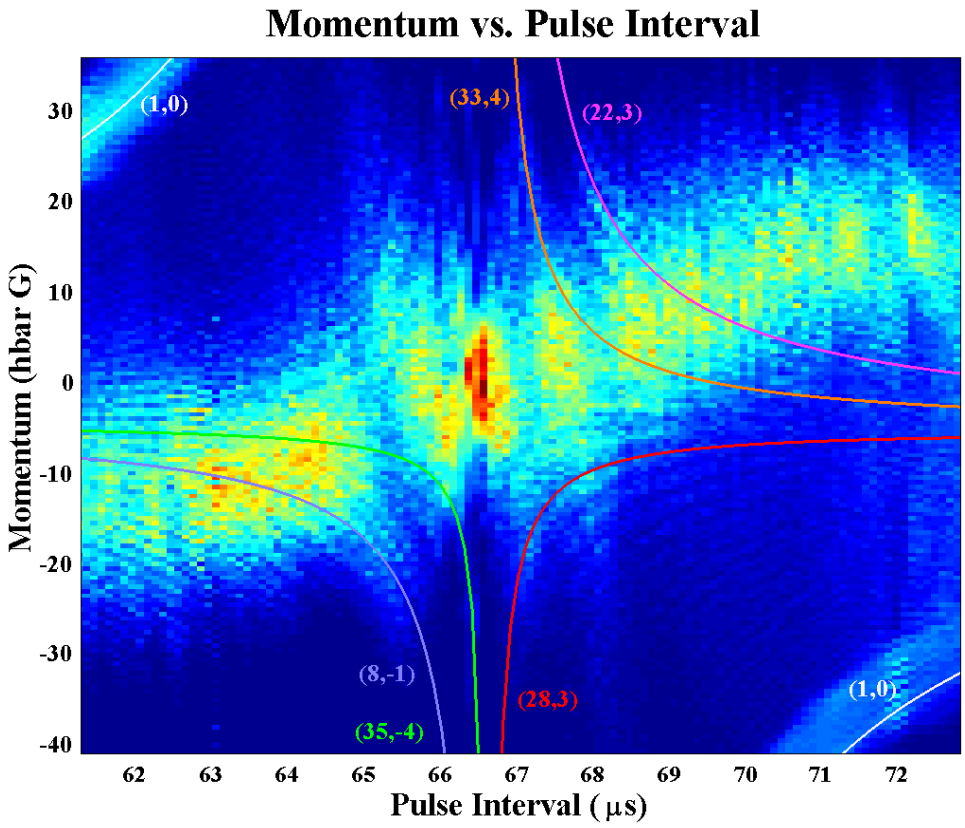

Figure 4.9. Theoretical results of changing the pulse interval across the Talbot time, with 45 pulses and $\phi_d=\pi$. The colored curves are Eq. (2.61) and represent the different orders of the QAMs as $(\mathbf{p}, \mathbf{j})$.

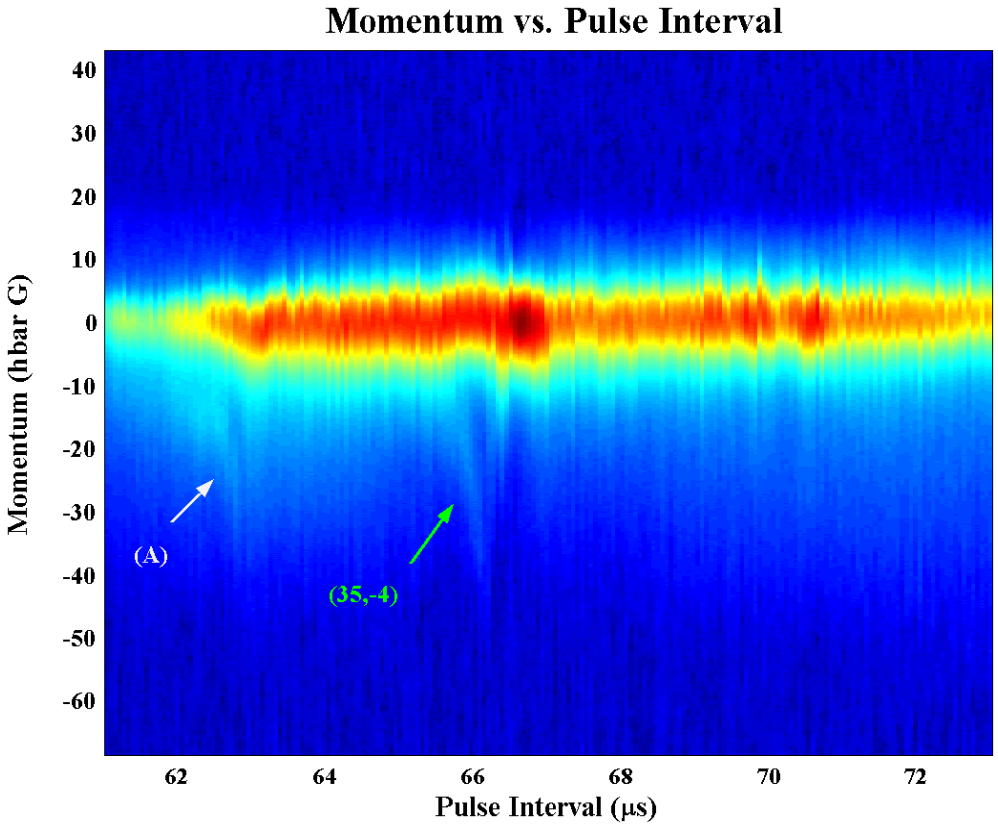

Figure 4.10. Experimental momentum distribution as a function of the pulse interval across the Talbot time, with 60 pulses and $\phi_d=\pi$. (A) represents dynamics not explained by the ϵ-classical theory.

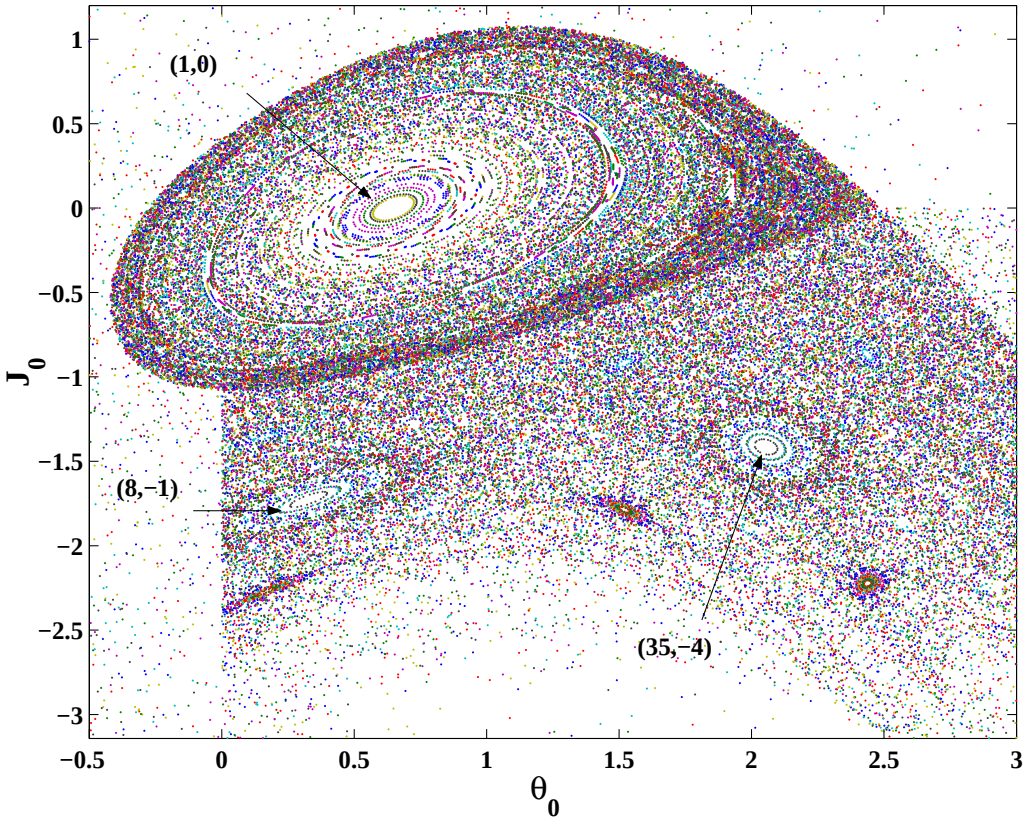

Figure 4.11. A phase mapping using Eq. (2.56) with 45 pulses, $\phi_d = \pi$, and time between pulses of 65 μs. Labeled are the most prominent higher order modes shown in Fig. 4.8.

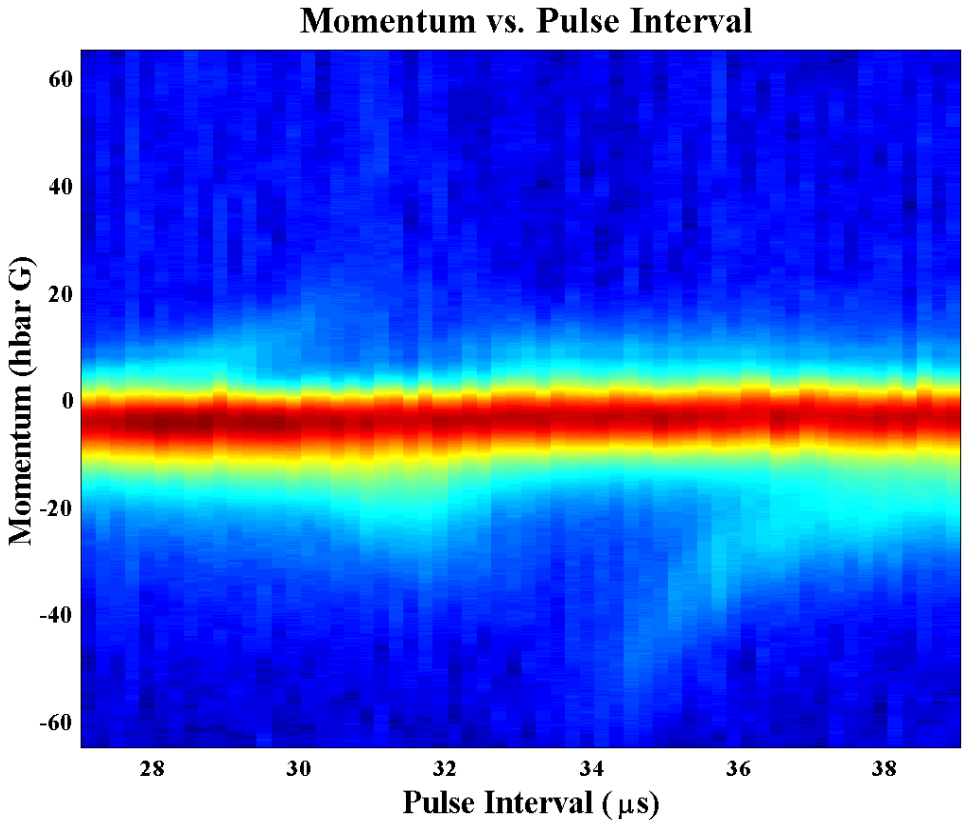

Figure 4.12. Experimental momentum distributions as a function of time between pulses across the Talbot time with circularly polarized pulsed light with 60 pulses and $\phi_d = \pi$.

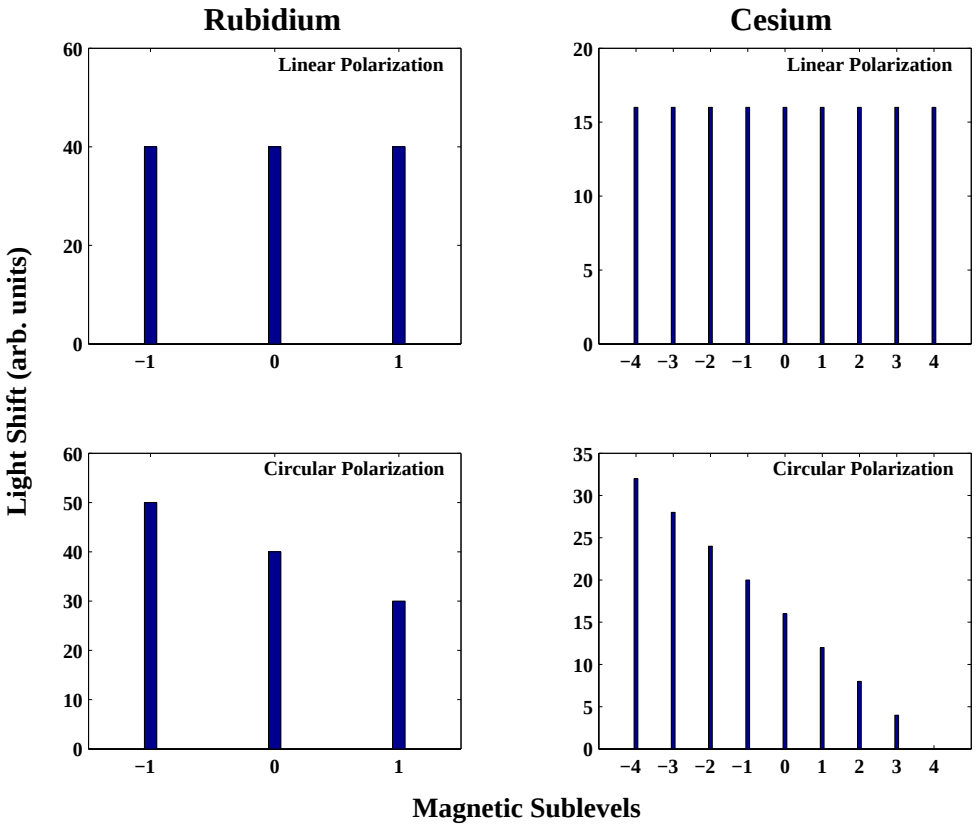

Figure 4.13. Light shifts of the different ground magnetic sublevels for rubidium (left) and cesium (right) (see the text for an example of generating these plots).

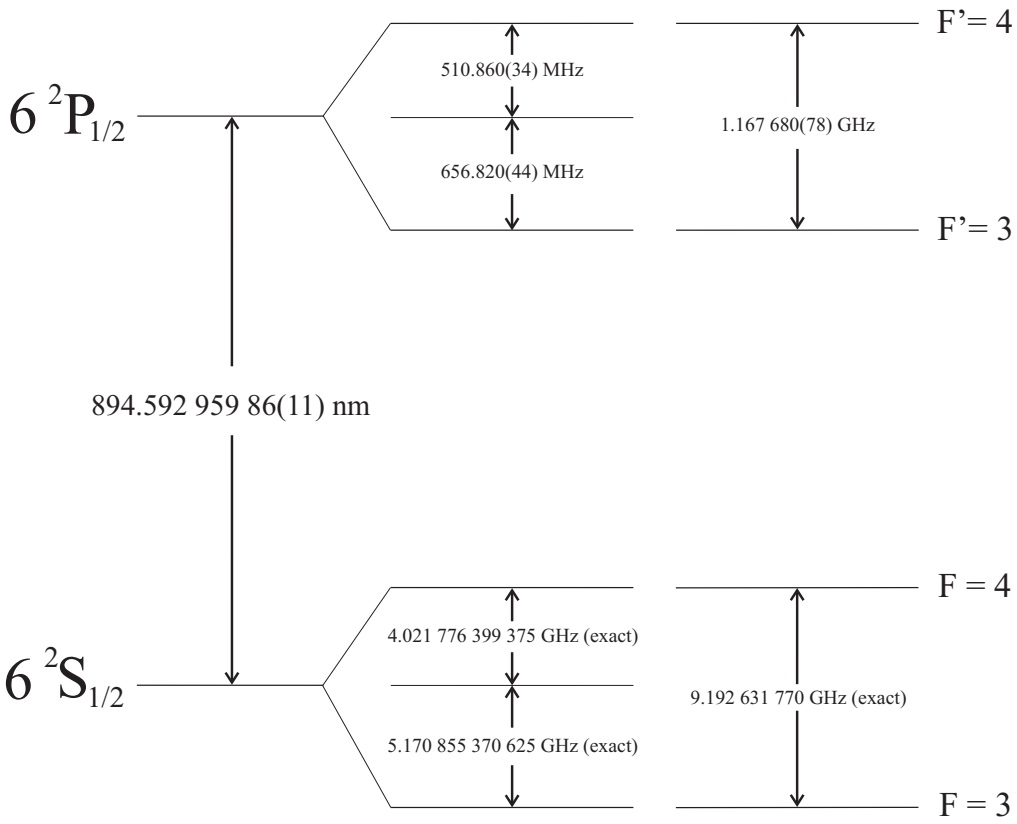

Figure 4.14. Hyperfine splitting of cesium 133 D1 line[59,60].

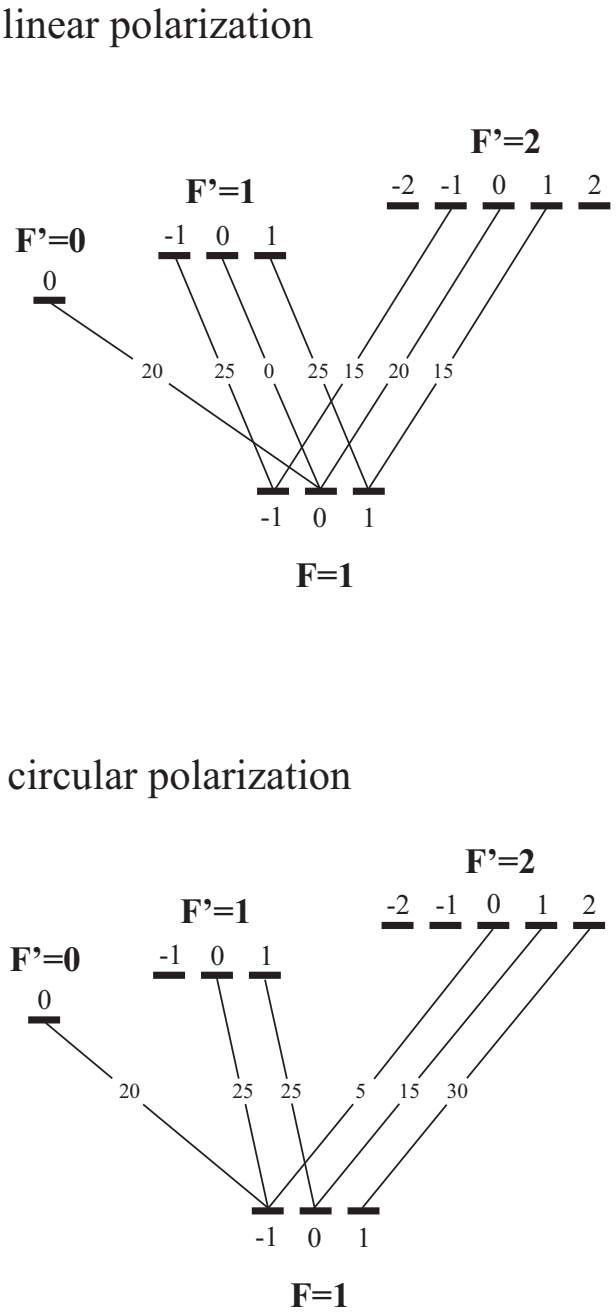

Figure 4.15. Rubidium 87 D2 line $F = 1 \rightarrow F' = 0, 1, 2$ transition strengths[32]. Linear polarized light follows the $\Delta M = 0$ selection rule and circularly polarized light follows the $\Delta M = \pm 1$ selection rule.

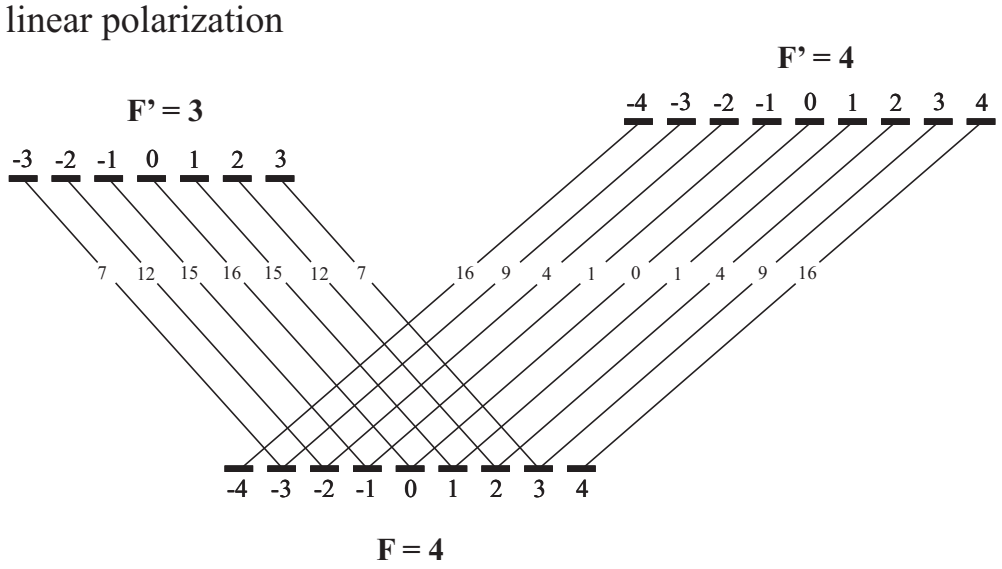

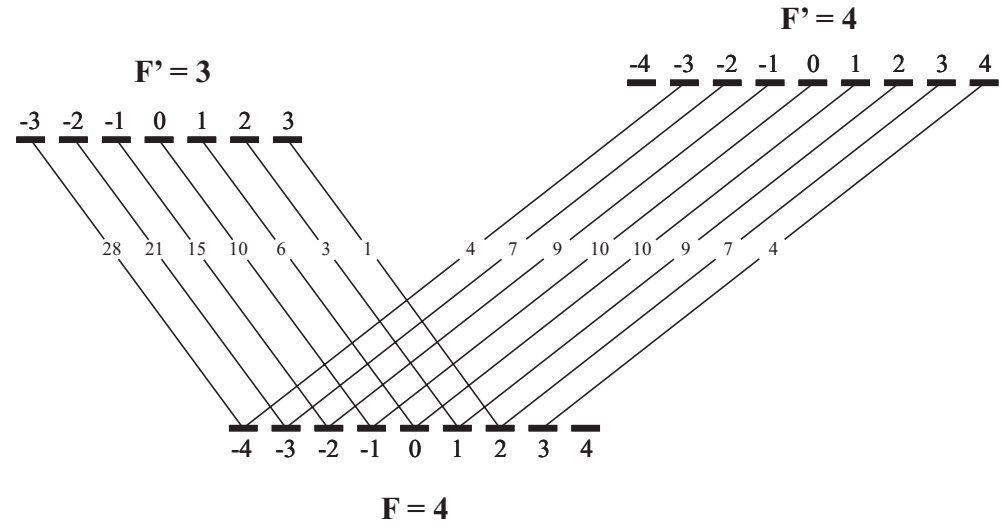

Figure 4.16. Cesium 133 D1 line $F = 3 \rightarrow F' = 3, 4$ transition strengths[32].

CHAPTER 5

CONCLUSION

5.1 Summary

In summary, we were able to observe quantum accelerator modes for the first time in rubidium 87 atoms using a newly constructed laser cooling apparatus. The cooling was required to fulfill an initial condition on the velocity of the atoms for the quantum accelerator modes. The dynamics of cold atoms in an off-resonant pulsed standing wave was studied through the phase model and the ϵ-classical theory. Both the phase model and the ϵ-classical theory explained the dynamics of a QAM, the later gave a more rigorous treatment and explained higher order QAMs as well.

A system for laser cooling rubidium 87 atoms was designed and built for the purpose of experimenting with the laser light interaction with atoms. This required an ultra-high vacuum system with sufficient optical access to perform the experiments which used multiple laser beams from several different directions. Due to the insufficient power of the master laser, a primary slave was injection locked to the master's frequency which in turn injection locked a secondary slave. The secondary slave provided approximately 40 mW of light for the experiment. A change in the light's frequency was needed in several parts of the experiment and was adjusted using acousto-optical modulators (AOMs). Optical fibers were used as light disconnects from the laser optical table to the vacuum chamber optical table for a good experiment beam quality and for alignment purposes. The time-of-flight (TOF) system used for detecting momentum distribution was a sheet of on-resonant light positioned approximately 4.5 inches below the trapped atoms. This measured the momentum

distribution of the atoms as they fell. The kicking experiments were performed using an off-resonant light pulse from the pulsing AOM. This light passed through the vacuum chamber and was retroreflected to produce the standing wave. The pulse length, light power, and time between pulses was adjusted through the arbitrary waveform generator controlling the pulsing AOM. The arbitrary waveform generator was programmed in Labview as were most other vital aspects of the experiment.

Extensive code was written using Labview for the instrumentation controls and data acquisition (portions of the code are included as an appendix). Finding the correct sequence of operations for the experiments was a time intensive task. However when finished, the experiments ran with very little trouble or human intervention. The automatic features written to perform the experiments continuously were very robust and allowed us to perform other tasks, such as data analysis, while an experiment was running. Creating Matlab code for the data analysis was an involved process as well. A graphical user interface (GUI) was written and required very little input to execute. Since in Labview, a parent file, consisting of all the experimental parameters, was saved. This file referenced thousands of data files which were loaded, averaged, plotted, and the plot was saved for later analysis.

The analysis of the experimental data verified the realization of quantum accelerator modes (QAM). This was shown in Fig. 4.2 for the experiment on changing the number of pulses. The right initial conditions were produced through achieving a cold sample of atoms for the initial velocity condition and programming the timing sequence for the pulse interval. With these initial conditions and gravitational potential energy, a linear increase in the atoms momentum was observed. Large amounts of momentum were imparted on the atoms (Fig. 4.3) which gives a large spatial splitting of the atoms. This could be used as a beamsplitter in an atom interferometer. A small number of higher order QAMs were observed. These higher order modes could prove useful in studying the dynamics of the quantum-classical boundary by tuning ϵ to near zero. The new dynamics observed far from the Talbot time were

very interesting. This was an important observation since much of the recent work on quantum chaos has *only* concentrated on understanding the behavior of systems near such primary resonances. Polarization effects were shown and resulted in a lower number of QAMs. This was due to the atoms interaction with different light shifts. Overall, the differences in the theory and experimental plots in Chapter 4 could be due to the initial velocity condition, pulsed beam size, and/or the angle of the pulsed beam.

5.2 Future Work

The future work involves resolving the higher order QAMs better, especially the new dynamics. The theory shows many more higher order modes than were seen experimentally. This in part was due to alignment issues, beam size, and initial velocity condition. A paper is being written on the experiments performed in this thesis.

Pulsing the atoms in a Bose-Einstein Condensate should populate more atoms in a QAM because more atoms will be at a more exact initial velocity condition. Also, this should help in resolving the higher order QAMs and the other dynamics far from the Talbot time. This proposed increase in QAM population will help us to understand the dynamics of quantum chaos.

BIBLIOGRAPHY

1. Christiaan Huygens translated by Silvanus P. Thompson, *Treatise on Light* (Dover, New York, 1962).

2. Isaac Newton, *Opticks* (London, 1704).

3. Thomas Young, *On the theory of light and colours*, Philosophical Transactions of the Royal Society of London, **92**, 12 (1802).

4. A. Einstein, *On a Heuristic Point of View About the Creation and Conversion of Light*, Ann. Physik, **17**, 132 (1905).

5. Louis deBroglie, *Non-Linear Wave Mechanics: A Casual Interpretation* (Elsvier, New York, 1960).

6. C. Davisson and L. H. Germer, *Diffraction of Electrons by a Crystal of Nickel*, Phys. Rev., **30**, 705 (1927).

7. P. L. Kapitza and P. A. M. Dirac, *The reflection of electrons from standing light waves*, Proc. Cambridge, Phil. Soc. **29**, 297 (1933).

8. S. Altshuler, L. M. Frantz, and R. Braunstein, *Reflection of Atoms from Standing Light Waves*, Phys. Rev. Lett. **17**, 231 (1966).

9. Philip E. Moskowitz, Phillip L. Gould, Susan R. Atlas, and David E. Pritchard, *Diffraction of an Atomic Beam by Standing-Wave Radiation* , Phys. Rev. Lett. **51**, 370 (1983).

10. Phillip L. Gould, George A. Ruff, and David E. Pritchard, *Diffraction of Atoms by Light: The Near-Resonant Kapitza-Dirac Effect* , Phys. Rev. Lett. **56**, 827 (1986).

11. T. W. Hänsch and A. L. Schawlow, *Cooling of Gases by Laser Radiation*, Phys. Rev. Lett. **13**, 68 (1975).

12. Steven Chu, L. Hollberg, J. E. Bjorkholm, Alex Cable, and A. Ashkin, *Three-Dimensional Viscous Confinement and Cooling of Atoms by Resonance Radiation Pressure*, Phys. Rev. Lett. **55**, 48 (1985).

13. E. L. Raab, M. Prentiss, Alex Cable, Steven Chu, and D. E. Pritchard, *Trapping of Neutral Sodium Atoms with Radiation Pressure* , Phys. Rev. Lett. **59**, 2631 (1987).

14. G. Timp, R. E. Behringer, D. M. Tennant, J. E. Cunningham, M. Prentiss, and K. K. Berggren,*Using Light as a Lens for Submicron,Neutral-AtomLithography*, Phys. Rev. Lett. **69**, 1636 (1992).

15. P. Berman, *Atom Interferometry* (Academic, San Diego, 1997).

16. M. H. Anderson, J. R. Ensher, M. R. Matthews, C. E. Wieman, and E. A. Cornell, *Observation of Bose-Einstein condensation in a dilute atomic vapor*,Science **269**, 198 (1995).

17. P. Ahmadi, G. Behinaein, B. P. Timmons, and G. S. Summy, *Experimental investigation of optical atom traps with a frequency jump*, J. Phys. B: At. Mol. Opt. Phys. **39**, 1159 (2006).

18. P. Ahmadi, B. P. Timmons, and G. S. Summy, *Geometrical effects in the loading of an optical atom trap*, Phys. Rev. A **72**, 023411 (2005).

19. H. M. Wiseman, *Defining the (atom) laser*, Phys. Rev. A **56**, 2068 (1997).

20. M. B. d'Arcy, R. M. Godun, D. Cassettari, and G. S. Summy, *Accelerator-mode-based technique for studying quantum chaos*, Phys. Rev. A **67**, 023605 (2003).

21. R. Graham, M. Schlautmann, and P. Zoller, *Dynamical localization of atomic-beam deflection by a modulated standing wave*, Phys. Rev. A **45**, R19 (1992).

22. Shmuel Fishman, Italo Guarneri, and Laura Rebuzzini, *A Theory for Quantum Accelerator Modes in Atom Optics*, J. Stat. Phys. **110**, 911 (2003).

23. F. L. Moore, J. C. Robinson, C. F. Bharucha, Bala Sundaram, and M. G. Raizen, *Atom Optics Realization of the Quantum δ-Kicked Rotor*, Phys. Rev. Lett. **75**, 4598 (1995).

24. Shmuel Fishman, Italo Guarneri, and Laura Rebuzzini, *Stable Quantum Resonances in Atom Optics*, Phys. Rev. Lett. **89**, 084101 (2002).

25. R. M. Godun,M. B. d'Arcy, M. K. Oberthaler, G. S. Summy, and Burnett, *Quantum accelerator modes: A tool for atom optics*, Phys. Rev. A **62**, 013411 (2000).

26. M. K. Oberthaler, R. M. Godun, M. B. d'Arcy, G. S. Summy, and K. Burnett, *Observation of Quantum Accelerator Modes*, Phys. Rev. Lett. **83**, 4447 (1999).

27. C. Ryu, M. F. Andersen, A. Vaziri, M. B. d'Arcy, J. M. Grossman, K. Helmerson, and W. D. Phillips, *High-Order Quantum Resonances Observed in a Periodically Kicked Bose-Einstein Condensate*, Phys. Rev. Lett. **96**, 160403 (2006).

28. R. Bach, K. Burnett, M. B. d'Arcy, and S. A. Gardiner, *Quantum-mechanical cumulant dynamics near stable periodic orbits in phase space: Application to the classical-like dynamics of quantum accelerator modes*, Phys. Rev. A **71** 033417 (2005).

29. S. Schlunk, M. B. d'Arcy, S. A. Gardiner, G. S. Summy, *Experimental Observation of High-Order Quantum Accelerator Modes*, Phys. Rev. Lett. **90**, 124102 (2003).

30. L. Allen and J.H. Eberly, *Optical Resonance and Two-level Atoms* (Dover, New York, 1987).

31. Peter F. Bernath, *Spectra of Atoms and Molecules* (Oxford, New York, 1995).

32. Harold J. Metcalf and Peter van der Straten, *Laser Cooling and Trapping* (Springer-Verlag, New York, 1999).

33. Marvin H. Mittleman, *Introduction to the Theory of Laser-Atom Interactions 2nd Ed.* (Plenum Press, New York, 1993).

34. Paul D. Lett, Richard N. Watts, Christoph I. Westbrook, William D. Phillips, Phillip L. Gould, and Harold J. Metcalf, *Observation of Atoms Laser Cooled below the Doppler limit*, Phys. Rev. Lett. **61**, 169 (1988).

35. William D. Phillips, John V. Prodan, and Harold J. Metcalf, *Laser cooling and electromagnetic trapping of neutral atoms*, J. Opt. Soc. Am. B **2**, 1751 (1985).

36. S. Chu, J. E. Bjorkholm, A. Ashkin, J. P. Gordon, and L. W. Hollberg, *Proposal for optically cooling atoms to temperatures of the order of* $10^{-6}K$, Opt. Lett. **11**, 73 (1986).

37. David E. Pritchard, *Cooling Neutral Atoms in a Magnetic Trap for Precision Spectroscopy*, Phys. Rev. Lett. **51**, 1336 (1983).

38. J. Dalibard and C. Cohen-Tannoudji, *Laser cooling below the Doppler limit by polarization gradients: simple theoretical models*, J. Opt. Soc. Am. B, **6**, 2023 (1989).

39. M.V. Berry and S. Klein, *Integer, fractional and fractal Talbot effects*, J. Mod. Opt. **43**, 2139 (1996).

40. A. J. Lichtenberg and M. A. Lieberman, *Regular and Chaotic Dynamics 2nd Ed.* (Springer-Verlag, New York, 1992).

41. A. Noble and M. Kasevich, *UHV optical window seal to conflat knife edge*, Rev. Sci. Instrum. **65** (9), September 1994.

42. Jeffrey J. Maki, N. S. Campbell, C. M. Grande, R. P. Knorpp, and D. H. McIntyre, *Stabilized diode-laser system with grating feedback and frequency-offset locking*, Opt. Comm. **102**, 251 (1993).

43. Soichi Kobayashi and Tatsuya Kimura, *Injection Locking in AlGaAs Semiconductor Laser*, IEEE J. Quantum Electron., **QE-17**, 681 (1981).

44. Anthony E. Siegman, *Lasers* (University Science Books, Mill Valley, CA, 1986), *p.* 1186.

45. T. W. Hänsch, M. H. Nayfeh, S. A. Lee, S. M. Curry, and I. S. Shahin, *Precision Measurement of the Rydberg Constant by Laser Saturation Spectroscopy of the Balmer α Line in Hydrogen and Deuterium*, Phys. Rev. Lett., **32**, 1336 (1974).

46. B. W. Petley, K. Morris, and R. E. Shawyer, *A saturated absorption spectroscopy measurement of the Rydberg constant*, J. Phys. B: At. Mol. Opt. Phys., **13**, 3099 (1980).

47. Kristan L. Corwin, Zheng-Tian Lu, Carter F. Hand, Ryan J. Epstein, and Carl E. Wieman, *Frequency-stabilized diode laser with the Zeeman shift in an atomic vapor*, Appl. Opt., **37**, 3295 (1998).

48. C. P. Pearman, C. S. Adams, S. G. Cox, P. F. Griffin, D. A. Smith, and I. G. Hughes, *Polarization spectroscopy of a closed atomic transition: applications to laser frequency locking*, J. Phys. B: At. Mol. Opt. Phys., **35**, 5141 (2002).

49. Jun Ye, Steve Swartz, Peter Jungner, and John L. Hall, *Hyperfine structure and absolute frequency of the ^{87}Rb $5P_{3/2}$ state*, Opt. Lett. **21**, 1280 (1996).

50. S. Bize, Y. Sortais, M. S. Santos, and C. Mandache, *High-accuracy measurement of the ^{87}Rb ground-state hyperfine splitting in an atomic fountain*, Europhys. Lett. **45**, 558 (1999).

51. Alan Lenef, Troy D. Hammond, Edward T. Smith, Michael S. Chapman, Richard A. Rubenstein, and David E. Pritchard, *Rotation Sensing with an Atom Interferometer*, Phys. Rev. Lett. **78** 164101 (1997).

52. David W. Keith, Christopher R. Ekstrom, Quentin A. Turchette, and David E. Pritchard, *An Interferometer for Atoms*, Phys. Rev. Lett. **66** 2693 (1991).

53. A. Peters, K. Y. Chung, and S. Chu, *High-precision gravity measurements using atom interferometry*, Metrologia **38**, 25 (2001).

54. Z.-Y. Ma, M. B. d'Arcy, and S. A. Gardiner, *Gravity-Sensitive Quantum Dynamics in Cold Atoms*, Phys. Rev. Lett. **93** 164101 (2004).

55. Sophie Schlunk, *Cold Atoms in a Periodic Optical Potential- A System for Studying Quantum Chaos*, Thesis

56. W. K. Hensinger, H. Häffner, A. Browaeys, N. R. Heckenberg, K. Helmerson, C. McKenzie, G. J. Milburn, W. D. Phillips, S. L. Rolston, H. Rubinsztein-Dunlop, and B. Upcroft, *Dynamical tunnelling of ultracold atoms*, Nature **412** 52 (2001).

57. Daniel A. Steck, Windell H. Oskay, Mark G. Raizen, *Observation of Chaos-Assisted Tunneling Between Islands of Stability*, Science **293** 274 (2001).

58. Amaury Mouchet and Dominique Delande, *Signatures of chaotic tunneling*, arXiv:quant-ph/0512072 **2** (2006).

59. Robert J. Rafac and Carol E. Tanner, *Measurement of the ^{133}Cs 6p $^{2}P_{1/2}$ state hyperfine structure*, Phys. Rev. A **56**, 1027 (1997).

60. Th. Udem, J. Reichert, R. Holzwarth, and T. W. Hänsch, *Absolute Optical Frequency Measurement of the Cesium D_1 Line with a Mode-Locked Laser*, Phys. Rev. Lett. **82**, 3568 (1999).

APPENDICES

APPENDIX A

PROGRAMMING CODE FOR DATA ACQUISITION AND DATA ANALYSIS

This appendix gives details of the coding required to perform the acquisition and analysis of the experimental data. Several months were devoted to developing code for this purpose. Labview was used for the experimental control and data acquisition procedures, while Matlab was employed on a dedicated computer for data analysis. This allowed us to run the experiments and perform the data analysis independently. Due to the different programming architectures, it was found that Matlab was better suited for the data analysis.

A.1 Labview Code for Data Acquisition

Labview is a graphical programming language using virtual instruments (VI) as an interface. Some VI's are provided with the software, and allow for the interfacing with specific data acquisition (DAQ) cards . Other VI's created by the user are called sub-VI's. A Labview program consists of two main windows, a front panel and a wiring diagram. The front panel contains the parameters which are used as inputs and outputs from the wiring diagram. An example of a front panel is shown in Fig. A.1. This is the main front panel used to run all of the laser cooling experiments and procedures. Figure A.2 shows the wiring diagram as a sequence structure within the main program.

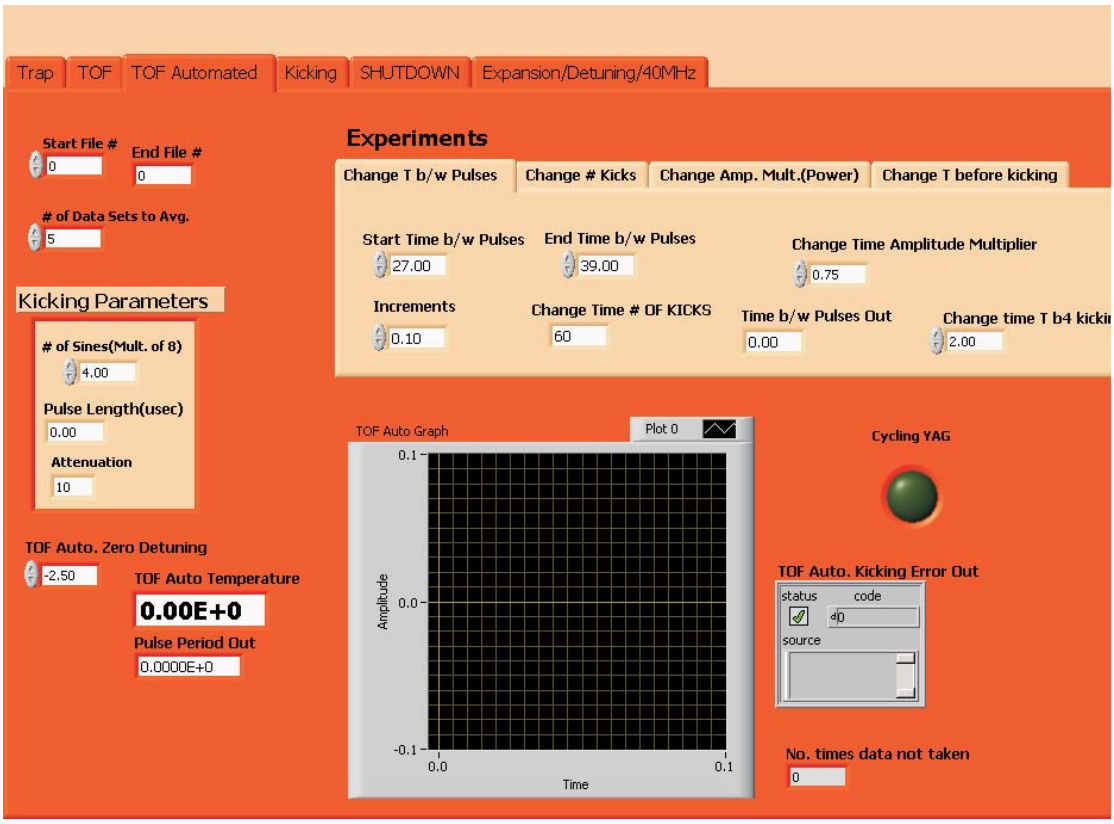

Figure A.1. The Labview front panel of the main laser cooling program. This panel provided a graphical interface for all of the experiments and procedures carried out in this thesis. The tabs at the top, "Trap", "TOF", "TOF Automated", etc., were used to interface to the various CASE structures within the wiring diagram of Fig. A.2, with each CASE representing a different procedure or experiment. The tab selected in this particular screen shot is that of "TOF Automated". Within the "TOF Automated" tab front panel were other tabs which refer to the different possible experiments which could be run. By clicking on an experiment tab and pressing "Run" that experiment was executed with the parameters loaded in the front panel. The results of the experiments are shown in Chapter 4.

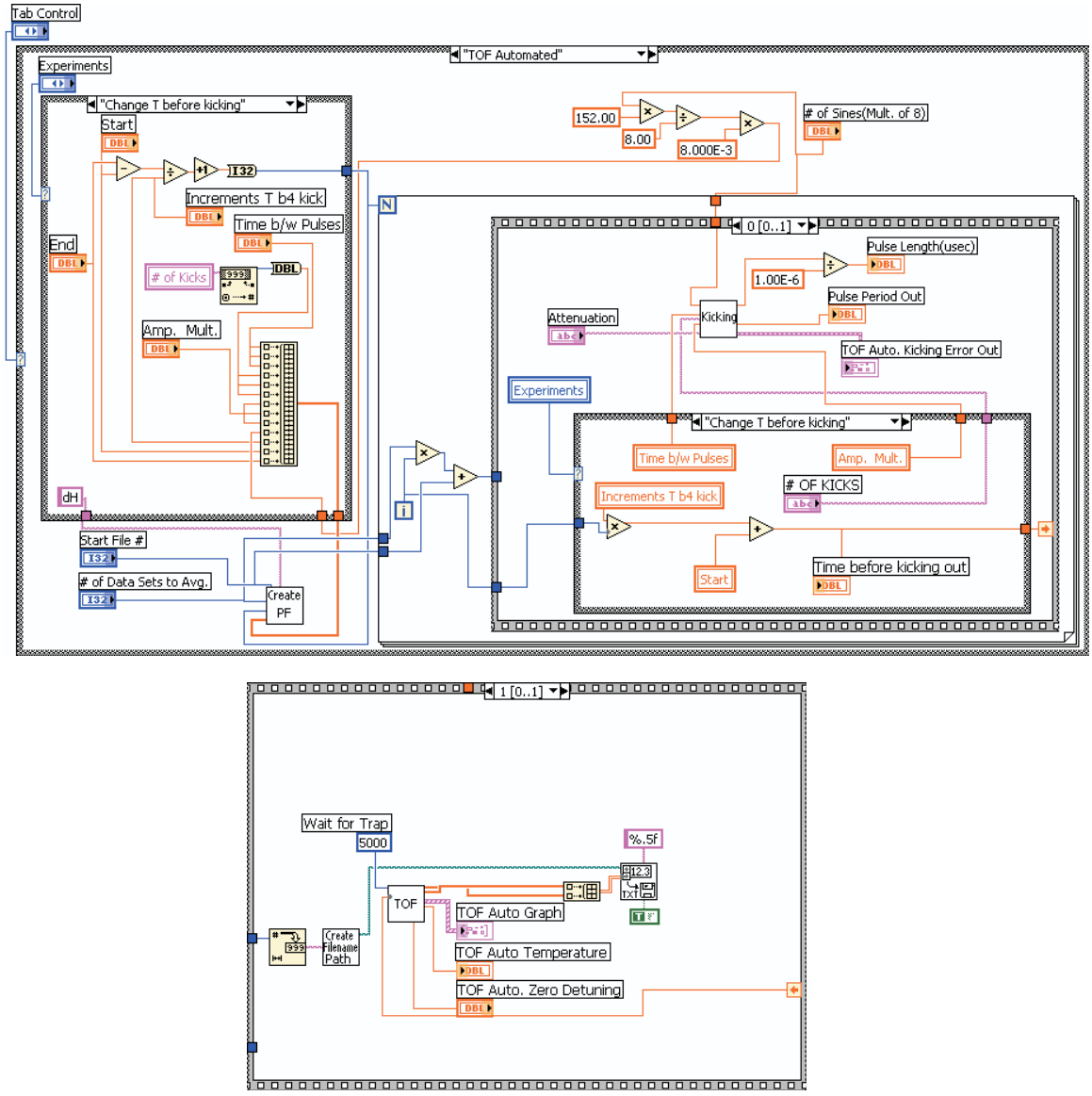

Figure A.2. The TOF Automated CASE structure in the main program wiring diagram. The wiring diagram took information entered on the front panel and then executed those parameters.

An example of how to run the "Change T b/w Pulses" experiment (shown in Fig A.1) will now be given. The initial parameters, "Start File #", "# of Data Sets to Avg.", and "# of Sines" are entered and set to 0, 5, and 4 respectively. Note that the later parameter represents a pulse length of 0.6 μs. Then the experimental parameters, "Start Time b/w Pulses" =27 μs, "End Time b/w Pulses" =39 μs, "Increments of Time" =0.1 μs, "No. of Kicks" =60, "Amp. Mult." =0.75 (represents pulsing beam power 25 mW), and "Time b4 Kicking" =2 ms are entered. The run button (not shown) is pushed and the program executes. The first part of the program saves a parent file (PF), through the "Create PF" sub-VI in the lower left of Fig. A.2, of all parameters used for the experimental run. This file is used later for data analysis and as a log of the parameters used. The program then enters a FOR loop. Inside the FOR loop is a SEQUENCE structure, represented by a box that looks like a piece of 35 mm camera film. The pulsing parameters are loaded into the kicking sub-VI, Fig. A.3, in the first frame of the sequence. One of these parameters is the 40 MHz waveform created in the "X MHz Calc'd Sine" sub-VI (shown in Fig. A.4) to program the waveform generator. The second frame of the sequence contains the TOF sub-VI. The TOF sub-VI, shown in Fig. A.5 and A.6, is repeated inside a FOR loop, each iteration of the loop acquiring a new data set with the same parameters for use in determining an averaged TOF signal. At the end of the TOF FOR loop, the outer FOR loop returns to the kicking SEQUENCE frame. The "Time b/w Pulses" has now been incremented to 27.1 μs, a value that is loaded into the kicking sub-VI for the next loop. The process is repeated until "End Time b/w Pulses" is 39 μs.

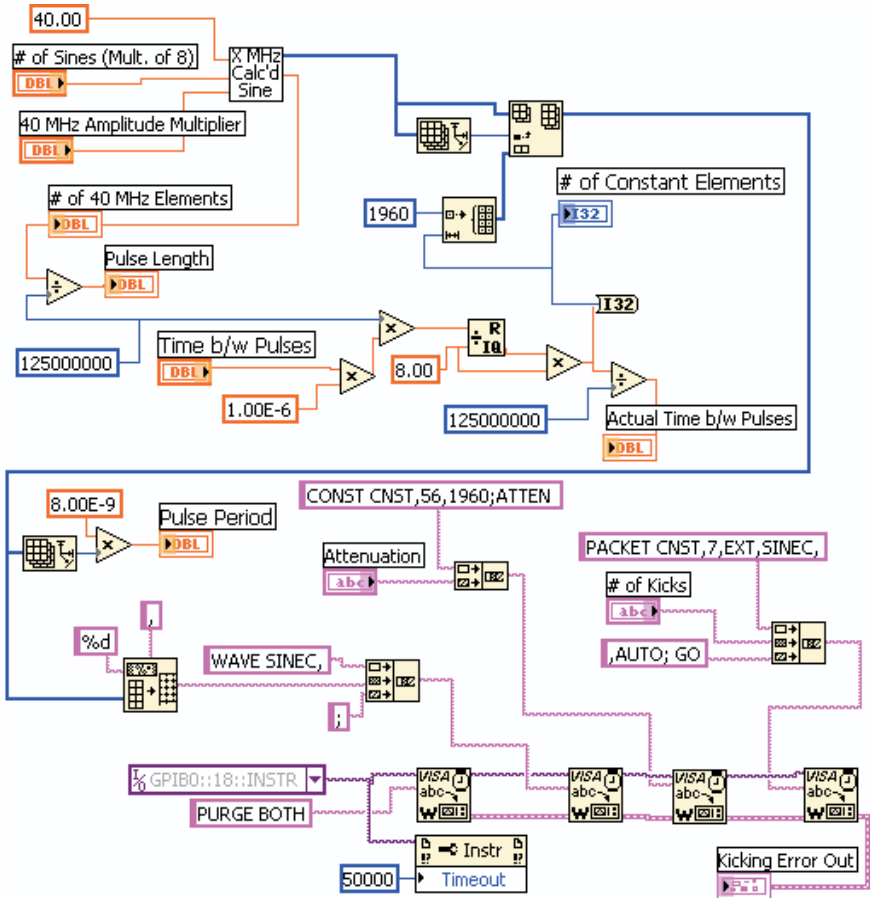

Figure A.3. The kicking sub-VI diagram was written to supply the appropriate syntax for the HP8770A arbitrary waveform generator. A 40 MHz waveform was created in the "X MHz Calc'd Sine" sub-VI in the upper left. Also, a waveform of zeroes was created and the length of the zero waveform depended on the "Time b/w Pulses" entered in the front panel of Fig. A.1. The zero waveform was appended to the 40 MHz sine to create a pulsed waveform. The pulsed waveform was loaded into the HP8770A and set for external TTL trigger.

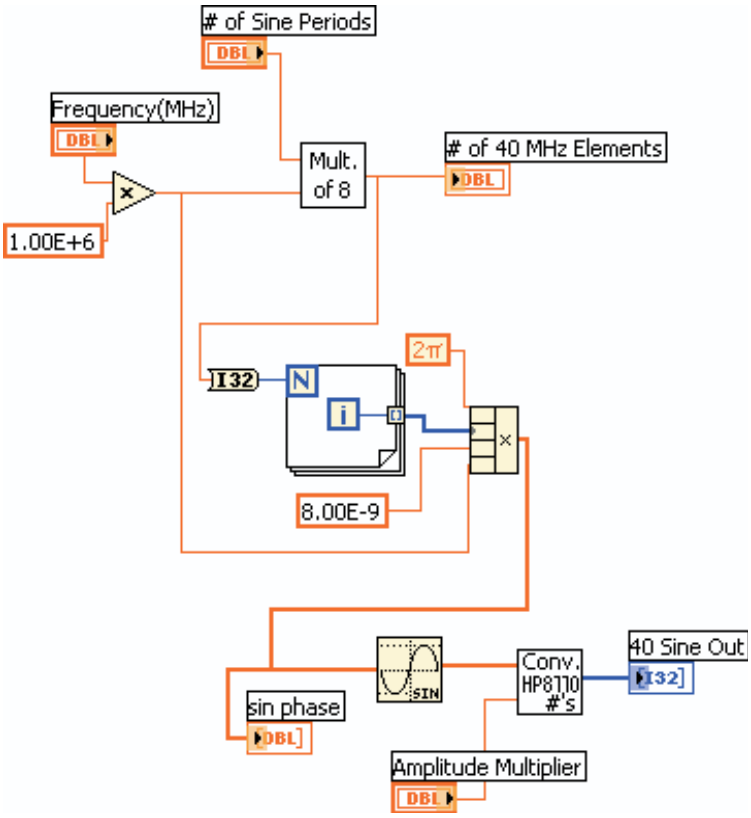

Figure A.4. "40 MHz generator" sub-VI diagram. This was used to create a 40 MHz waveform for loading into the kicking sub-VI. The "No. of Sines Periods" was an input on the main VI of Fig. A.1 and represented the pulse length. Due to the restrictions of the HP8770A, the number of elements in the waveform needed to be a multiple of 8. This was the "Mult. of 8" sub-VI. The FOR loop generated the appropriate number of elements for the input parameters "Frequency(MHz)" and "No. of Sine Periods". The "Conv. HP8770 Nos." sub-VI converted the waveform to numbers readable by the HP8770A. The "Amplitude Multiplier" determined the power applied to the pulsing AOM and was a number between 0 and 1.

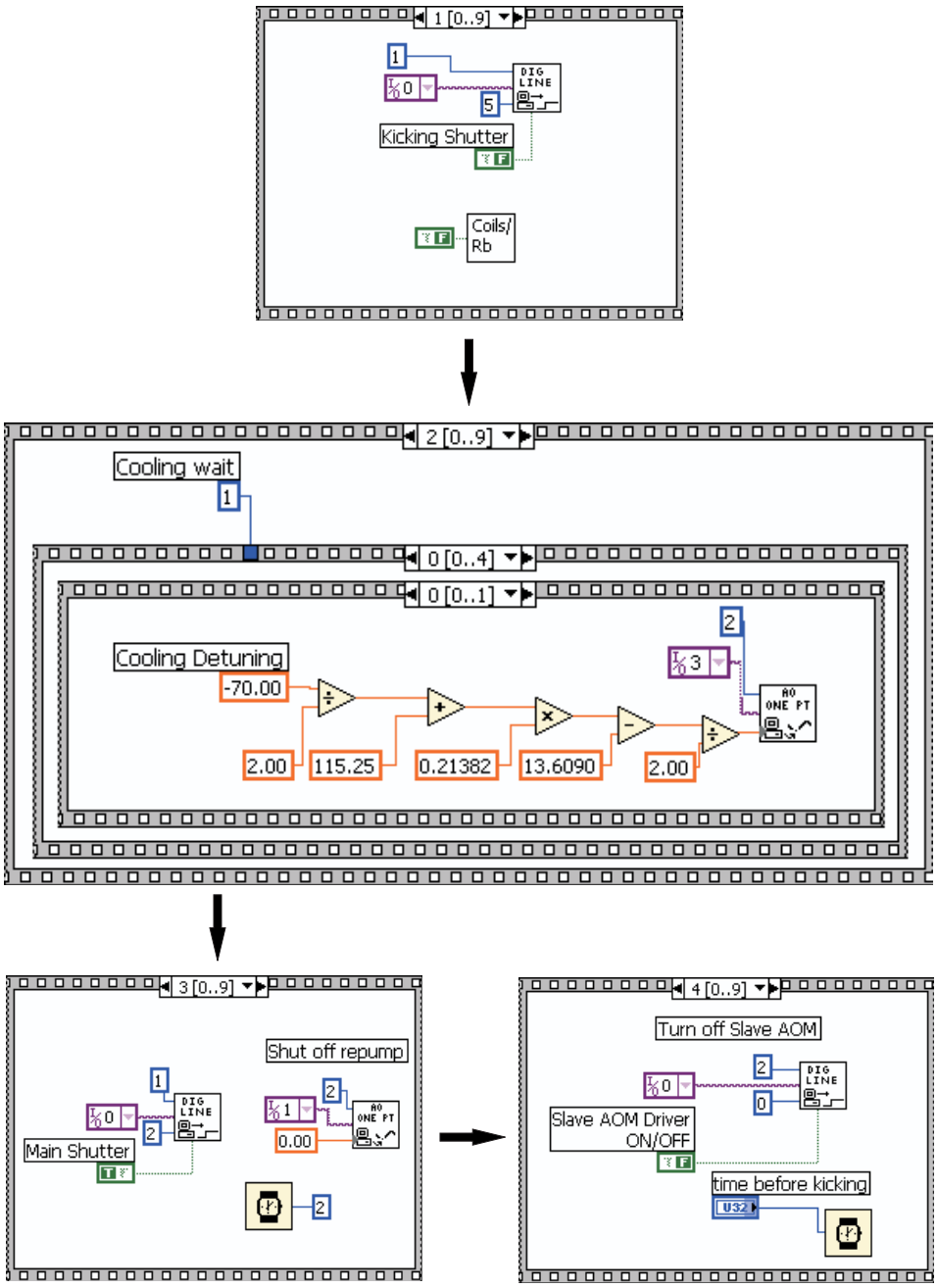

Figure A.5. The first four steps in the TOF sub-VI. A detailed explanation was given in Chapter 4. Note the center sequence structure in this figure with its multiple internal SEQUENCE structures. The timing in this sub-VI was crucial as this controls the detuning and power in the laser beam as the laser cooling process proceeded.

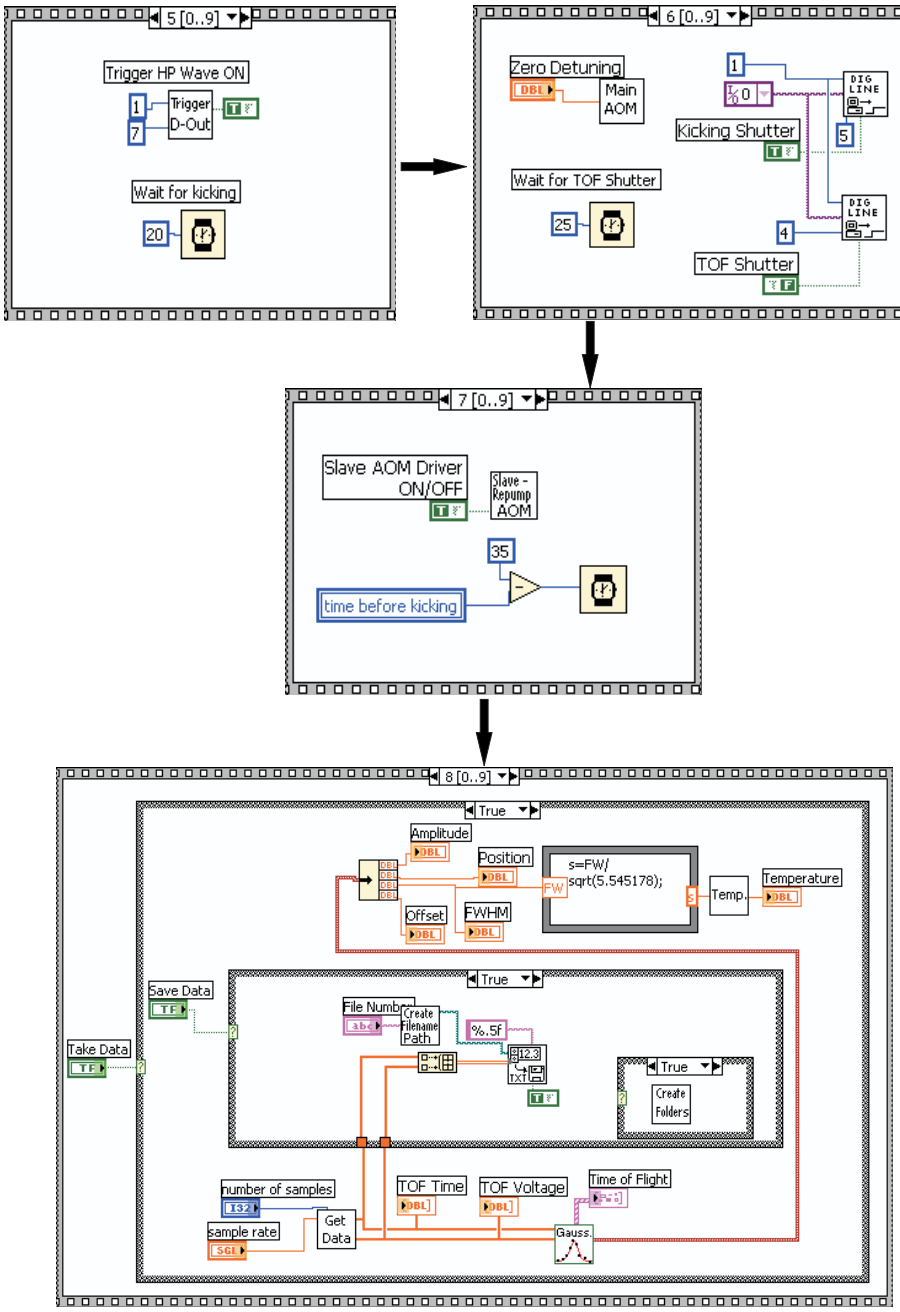

Figure A.6. The last four steps in the TOF sub VI. Here the HP8770A was triggered to pulse the atoms and the TOF signal was saved.

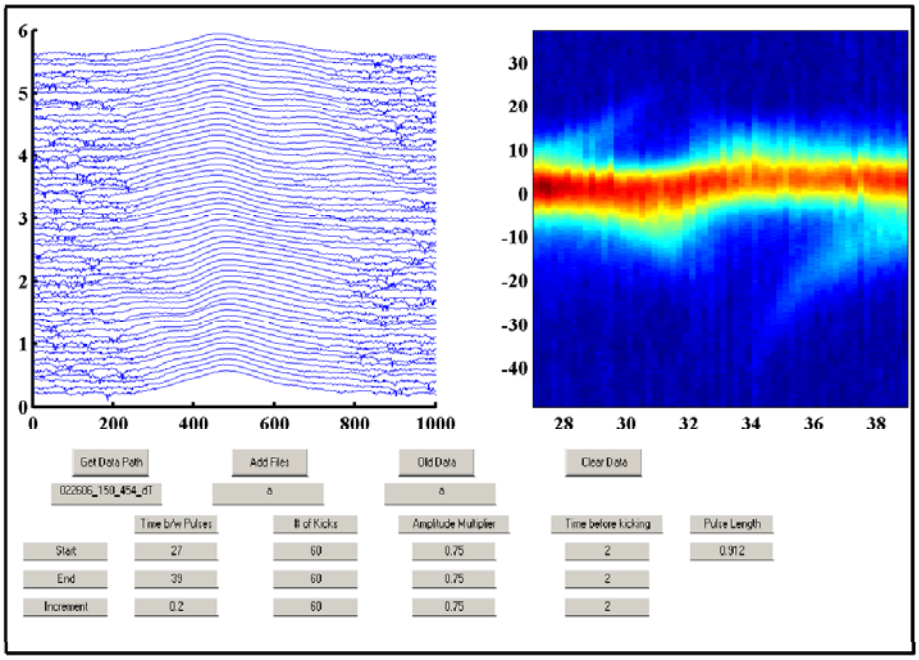

Figure A.7. The "QAM" graphical user interface (GUI) shows a typical experimental analysis. The "Get Data Path" when pushed allowed the user to choose a file for analysis. The parameters of the experiments were shown in the lower left of the figure.

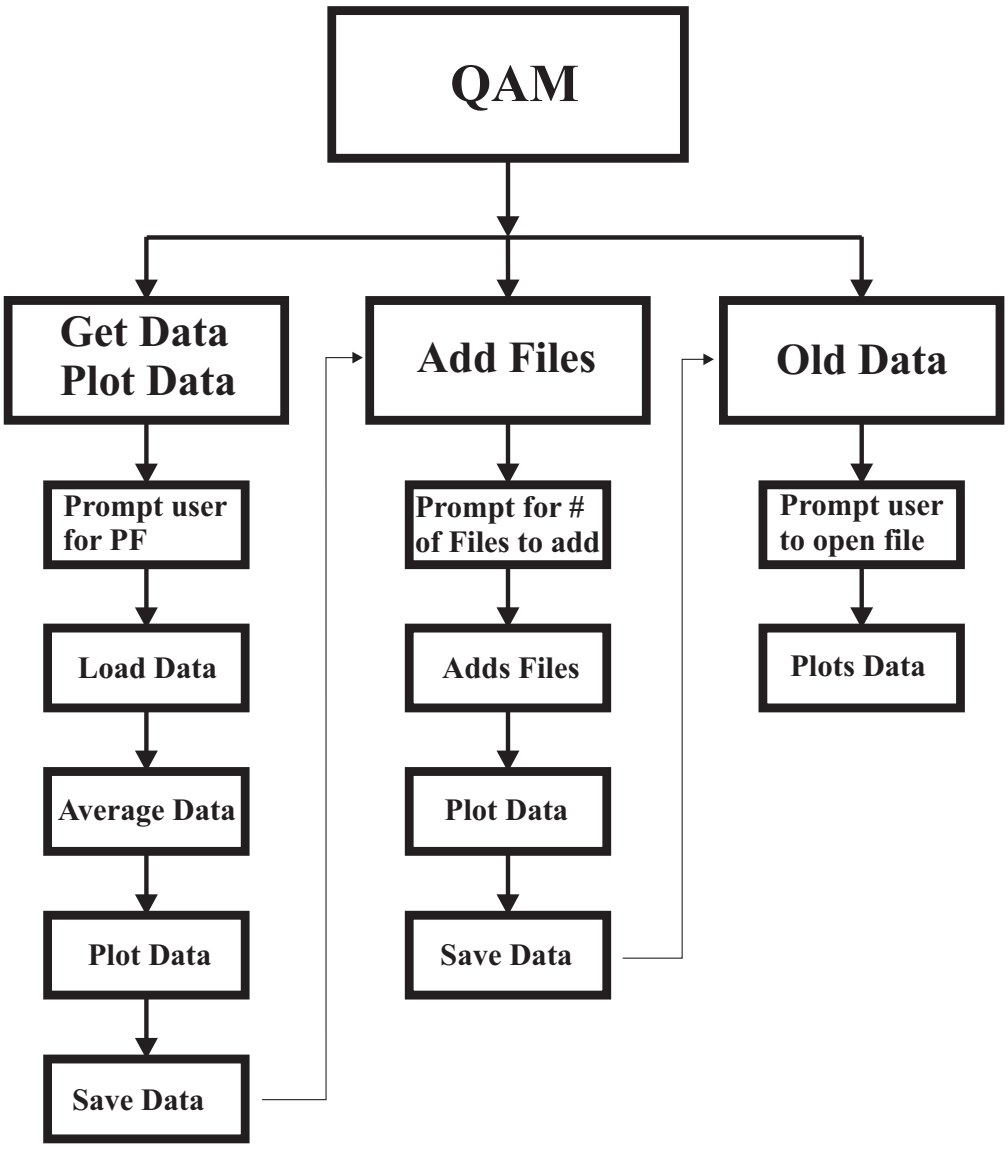

Figure A.8. A flow chart of the data analysis program written in Matlab. The arrows pointing from the save data boxes to the "Add Files" and "Old Data" boxes means the "Get Data" should be executed before "Add Files" and the "Add Files" should executed before "Old Data".

A.2 Matlab Code for Data Analysis

A large amount of effort was spent creating a robust, user friendly data analysis program. Matlab was chosen due to the extensive calculations and large number of data files involved. These calculations were not straightforward using the graphical interface and wiring architecture of Labview. Figure A.8 shows schematic diagram of the data analysis program. The main program name was "QAM", which when executed, opened a graphical user interface (GUI) shown in Fig. A.7. The GUI had three push buttons, "Get Data", "Add Files", and "Old Files". The "Get Data" push button when selected prompted the user to open the PF created in Labview. The PF had the parameter information of the TOF files saved during the experiment. The program took this information and searched the current directory for the appropriate TOF files. The TOF files were loaded and averaged. The averaged files were combined and plotted as shown in Fig. A.7. The averaged files were saved and were used in the "Add Files" routine.

The experiments were all automated and could take as long as 3 hours to complete. Thus it was important to be able to walk away and perform other tasks. One problem with this approach, was that on occasions the experimentalist would come back to find no data, typically caused by a laser malfunction at some point during the experimental run. Therefore, an "Add Files" routine was added to the program to analyze the experiments in steps. When the "Add Files" push button was pushed it prompted the user to enter the number of files to add. The files were then selected by the user through prompts. The program took those files and appended the files to create the plot. The experimental data was plotted and saved for reviewing later with

the “Old File” routine. The “Old File” routine, when pushed, prompted the user to open a file and then plotted the data in the file.

APPENDIX B

PUBLICATIONS

This appendix shows a reproduction of my publications. The research was done on the BEC chamber during a maintenance period on the laser cooling chamber.

Figures B.1-B.10 studied the evolution of a trapped atomic cloud subjected to a trapping frequency jump for two cases: stationary and moving center of mass. In the first case, the frequency jump initiated oscillations in the cloud's momentum and size. At certain times we found the temperature was significantly reduced. When the oscillation amplitude became large enough, local density increases induced by the anharmonicity of the trapping potential were observed. In the second case, the oscillations were coupled to the center-of-mass motion through the anharmonicity of the potential. This induced oscillations with even larger amplitudes, enhanced the temperature reduction and led to nonisotropic expansion rates while expanding freely.

Figures B.11-B.16 studied methods of loading atoms from a magneto-optic trap into an optical trap formed at the focus of a CO_2 laser. We showed that while the loading efficiency was very sensitive to the volume of the optical trap, it was insensitive to the total laser power once a certain threshold was reached. Based on these observations a time-averaged optical atom trap was realized to compensate for the small capture volume of tight traps which were required for efficient evaporative cooling. Up to a 100% increase in the trap population was observed for the time-averaged traps. We also studied the effect on temperature and trap population of changing

a time-averaged optical trap back to a static trap. Our results provided a basis for increasing the number of atoms in Bose-Einstein condensates produced using all-optical techniques and showed the a high-power laser was not a prerequisite for such an increase.

INSTITUTE OF PHYSICS PUBLISHING JOURNAL OF PHYSICS B: ATOMIC, MOLECULAR AND OPTICAL PHYSICS

J. Phys. B: At. Mol. Opt. Phys. **39** (2006) 1159–1168 doi:10.1088/0953-4075/39/5/014

Experimental investigation of optical atom traps with a frequency jump

P Ahmadi, G Behinaein, B P Timmons and G S Summy

Department of Physics, Oklahoma State University, Stillwater, OK 74078-3072, USA

E-mail: peyman.ahmadi@okstate.edu

Received 7 October 2005, in final form 25 January 2006
Published 15 February 2006
Online at stacks.iop.org/JPhysB/39/1159

Abstract

We study the evolution of a trapped atomic cloud subject to a trapping frequency jump for two cases: stationary and moving centre of mass. In the first case, the frequency jump initiates oscillations in the cloud's momentum and size. At certain times we find the temperature is significantly reduced. When the oscillation amplitude becomes large enough, local density increases induced by the anharmonicity of the trapping potential are observed. In the second case, the oscillations are coupled to the centre-of-mass motion through the anharmonicity of the potential. This induces oscillations with even larger amplitudes, enhancing the temperature reduction effects and leading to nonisotropic expansion rates while expanding freely.

(Some figures in this article are in colour only in the electronic version)

1. Introduction

A trapped atomic cloud subjected to a sudden change in its trapping potential can exhibit a wide range of behaviour with many possible applications. It can be used as a model for studding fundamental phenomenon ranging from superfluidity to the generation of non-classical states of a matter wavepacket. For instance, a Bose–Einstein condensate can be reversibly created by suddenly changing the trapping potential [1]; sinusoidally moving a magnetic trap centre can be used to observe the excitation modes of a Bose–Einstein condensate [2]; the modulation of optical traps can be used for coherent control of the centre-of-mass wavepacket [3]; and the breathing mode oscillation of atomic clouds in 1D and 3D optical lattices can be realized by suddenly changing the lattice depth [4]. The later has also captured a great deal of theoretical interest because of the possibility of creating squeezed states of a matter wavepacket [5–11].

The oscillation of an atomic cloud after a sudden jump in the trapping frequency has also been proposed as a tool for optical cooling and hence controlling the onset of Bose–Einstein condensation [12, 13]. This cooling method can be categorized among the techniques that use geometrical manipulation of an external potential to reduce the temperature of atoms

0953-4075/06/051159+10$30.00

Figure B.1. Journal of Physics: Page 1.

or molecules. For example, Flories *et al* [14] used a spatially varying electric field to longitudinally cool a molecular beam to 250 nK, while Ketterle and coworkers achieved pico-Kelvin temperatures by adiabatically decompressing a gravito-magnetic trap [15]. Exposing a freely expanding cloud of cold atoms to a pulsed potential has also been considered as a method for temperature reduction [16].

In this paper, we use far-off resonant optical trap (FORT) to experimentally realize a potential with a sudden frequency jump so as to explore the cooling proposals of [12]. These traps have become versatile tools for atom optics research, with the observation of all-optical Bose–Einstein condensation as an example of their dramatic potential [17]. Early experiments on intensity modulation of the laser beam used to form an optical trap [4,18–20] were used to demonstrate the parametric excitation of an atomic cloud. In this paper we will discuss experiments with these traps, comparing the observations with theory, and presenting possible future applications. The format of this paper is as follows. In section 2, the experimental configuration is reviewed. In section 3, we first lay out the theory of non-adiabatic cooling of an atomic cloud, then follow by presenting experimental data for the case of a sudden frequency jump with a stationary centre of mass. This discussion is then repeated in section 4 for the case of a moving centre of mass.

2. Experimental configuration

Our experimental apparatus has been described previously [21, 22], so only a brief description is given here. We create a potential for Rb87 atoms using their interaction with 10.6 μm light from a CO_2 laser. The CO_2 laser radiation frequency is far enough below that of the resonances of the atoms that its electric field can be considered quasi-static. This induces a dipole moment proportional to the local electric field and a lowering of the atomic ground state energy given by, $U = -\frac{1}{2}\alpha_g|E|^2$, where α_g is the ground state static polarizability and $|E|^2$ is the time averaged square of the laser light's electric field.

Two CO_2 beams were directed into a vacuum chamber in a geometry such that they propagated orthogonally to each other. One of the beams propagated in the vertical direction (x direction) and the other in the horizontal direction (z direction). Crucially the position where the x beam intersected the z beam could be adjusted. That is, the foci of the two beams did not necessarily coincide. The light for these beams originated from a 50 W RF excited CO_2 laser whose total power was controlled by passing the output light through an acousto-optic modulator (AOM). The first-order beam of the modulator was then directed into another AOM which was used as a beamsplitter whose ratio could be changed by varying the input RF power. This ratio was used to control the time-dependent potential. In order to fulfil the conditions necessary for this experiment, the CO_2 beams were aligned such that the x beam was the first order of the second AOM and the z beam the zeroth order of the same AOM. The data were taken by destructively imaging the cloud using a resonant probe laser which passed through the atom cloud and was then incident on a CCD camera. A Gaussian fit to the optical density data determined the spatial extent of the atomic cloud.

3. Stationary centre of mass

We begin by theoretically considering the situation where the centre of mass of the atomic cloud remains stationary after a sudden change in the trapping potential. We take a sample of atoms in thermal equilibrium inside a harmonic potential of frequency ω_0 which is non-adiabatically changed to ω_1 at $t = 0$. Neglecting the effect of collisions and following

Figure B.2. Journal of Physics: Page 2.

Balatov *et al* [12], the momentum and position probability distribution widths are given by

$$\sigma_p^2(t) = \frac{1}{2}\sigma_p^2(0)\left[1 + \left(\frac{\omega_1}{\omega_0}\right)^2 + \left(1 - \left(\frac{\omega_1}{\omega_0}\right)^2\right)\cos(2\omega_1 t)\right] \tag{1}$$

$$\sigma_z^2(t) = \frac{1}{2}\sigma_z^2(0)\left[1 + \left(\frac{\omega_0}{\omega_1}\right)^2 + \left(1 - \left(\frac{\omega_0}{\omega_1}\right)^2\right)\cos(2\omega_1 t)\right] \tag{2}$$

where at $t = \frac{\pi}{2\omega_1}$ they reduce to

$$\sigma_p^2\left(\frac{\pi}{2\omega_1}\right) = \left(\frac{\omega_1}{\omega_0}\right)^2 \sigma_p^2(0) \tag{3}$$

$$\sigma_z^2\left(\frac{\pi}{2\omega_1}\right) = \left(\frac{\omega_0}{\omega_1}\right)^2 \sigma_z^2(0). \tag{4}$$

For $\omega_1 \ll \omega_0$, a narrow momentum distribution is produced corresponding to a lower effective temperature. In the case of a single Gaussian laser beam propagating in the z direction the average electric field can be expressed as

$$|E(x, y, z)|^2 = E_0^2 \frac{w_0^2}{w(z)^2} \exp\frac{-2(x^2 + y^2)}{w(z)^2} \tag{5}$$

where $w(z) = w_0\left(1 + \left(\frac{z}{z_R}\right)^2\right)^{\frac{1}{2}}$ and E_0 is the electric field amplitude. Here w_0 is the beam waist at the focus, and z_R is the Rayleigh length. By carrying out a series expansion around $x = y = z = 0$ and discarding terms of third order and higher, a harmonic approximation of the potential is obtained,

$$U(x, y, z) = U_0\left(\frac{2(x^2 + y^2)}{w_0^2} + \frac{z^2}{z_R^2}\right) \tag{6}$$

where $U_0 = -\frac{1}{2}\alpha_g E_0^2$. The oscillation frequencies in the three directions are $\omega_x^2 = \omega_y^2 \simeq 4U_0/mw_0^2, \omega_z^2 \simeq 2U_0/mz_R^2$. When the total laser power is shared with a second beam propagating in the x direction which crosses the first beam at its focus, these frequencies change to $\omega_y^2 \simeq 4U_0/mw_0^2, \omega_x^2 = \omega_z^2 \simeq 2U_0/mw_0^2$ at the intersection point. This assumes that the beams have identical properties and $z_R \gg w_0$. According to these results, an abrupt change from a two-beam to a one-beam geometry will produce a significant frequency change along the z direction. The ratio of one and two-beam frequencies is

$$\frac{\omega_{1\text{beam}}}{\omega_{2\text{beam}}} = \frac{w_0}{z_R} = \frac{\lambda}{\pi w_0} \tag{7}$$

which is independent of the total laser power and is determined by the beam waist at the focus. Since the temperature of the atomic cloud is proportional to the momentum distribution squared, combining equations (3) and (7) gives

$$\frac{T_{\text{final}}}{T_{\text{initial}}} = \left(\frac{\omega_1}{\omega_0}\right)^2 = \left(\frac{\lambda}{\pi w_0}\right)^2. \tag{8}$$

To explore this behaviour experimentally we aligned the CO_2 beams such that their foci overlapped. Atoms were loaded into the potential minimum created by the intensity maximum located at the intersection of the beams. The power in the x beam was transferred to the z beam by switching the RF power on the second AOM to zero. This abrupt transfer of power mostly produced a change in the effective frequency in the z direction and initiated the oscillation

Figure B.3. Journal of Physics: Page 3.

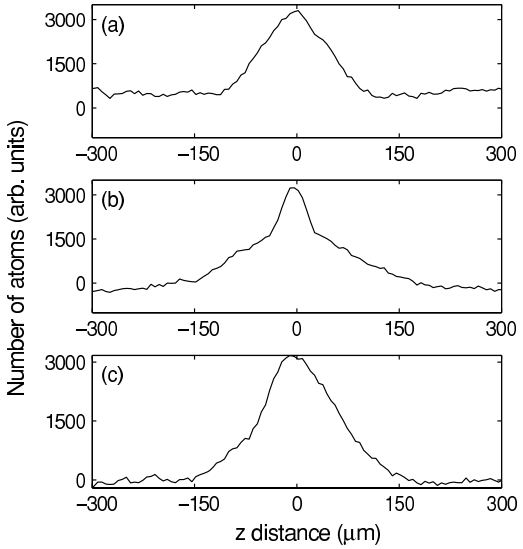

Figure 1. The accumulated intensity along the x-axis as a function of z distance. Two beams from a CO_2 laser crossed each other at right angles with overlapping foci and 5 W power. Parts (a), (b) and (c) were obtained 2, 5 and 10 ms after extinguishing the x beam. A denser component is obvious at the centre of the cloud in (b).

of the trapped cloud. If the shift of power to the z beam happens immediately after loading, the FORT will not produce the desired oscillation since the atomic density is approximately 10^{14} atoms cm^{-3} and cold binary scattering dramatically affects the evolution of the cloud. Therefore the collisionless approximation of the previous section cannot be used. To move into the collisionless regime it is necessary to decrease the atomic density by reducing the number of atoms before the power transfer. This is accomplished by reducing the total power in the CO_2 beams in order to carry out forced evaporation of hot atoms. This reduces both the density of atoms in the trap and their temperature. This process is carried out so that the atomic cloud which remains in the FORT has densities of around 10^{11} atoms cm^{-3}. This guarantees that the mean free path of the individual particles is bigger than the cloud size so that the evolution of the sample can be considered in the collisionless regime.

After evaporative cooling the total power was transferred to the z beam and the cloud size started to oscillate in the z direction. However, the time evolution of the cloud size did not obey the simple periodic form predicted by equation (2). Our observations show that a domain with a high atomic density appears at the centre of the trap periodically during the cloud's evolution. This structure is reminiscent of the two-component structure which appears at the onset of a degenerate Bose gas. Three cross sections of the cloud along the z-axis are shown in figure 1. Figures 1(a), (b) and (c) were taken 2, 5 and 10 ms after switching off the x beam respectively. The total power in the CO_2 beams was 5 W. A high-density region at the centre of figure 1(b) is clearly visible. It disappears later in the evolution as seen in figure 1(c). Creation of these high-density regions is a direct result of the strong anharmonic potential and is predicted in [13]. A Monte Carlo simulation of the anharmonic system can reproduce this behaviour for the cloud. Figure 2 presents the result of such a collisionless calculation at the moment where the two-component structure appears. The simulation was

Figure B.4. Journal of Physics: Page 4.

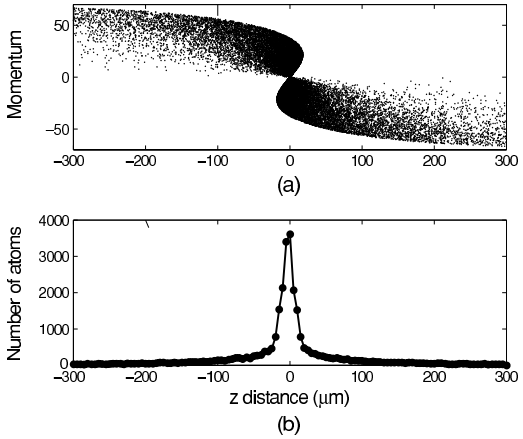

Figure 2. (a) Calculated z direction phase space distribution of the atoms at the moment where the two-component structure appears. The atoms were initially distributed uniformly throughout the phase space and physically located at the crossover of two beams with overlapping foci. The horizontal axis is the z-direction spread of the particles in units of the beam waist and the vertical axis is the z-momentum in units of the photon recoil from a 780 nm photon. (b) The corresponding histogram of the particles' distribution in the z direction.

carried out for 3×10^4 atoms initially at thermal equilibrium with a 25 μm initial cloud size. It is worth noting that the high-density regions never appeared when harmonic potentials were simulated.

The high-density region makes the observed optical density profiles complex enough that it is impossible to fit a Gaussian function to the data and infer the width of the cloud. Therefore to observe the oscillation of the cloud size, predicted by equation (2) we have reduced the total power in the CO_2 beams to 0.5 W. In this regime, the cloud temperature is low enough (below 2 μK) that the oscillation amplitude does not move the atoms away from the region where the harmonic approximation of the potential is valid. Furthermore, as mentioned above, the evaporative cooling also reduces the atomic density to $\approx 10^{11}$ atom cm^{-3}, suppressing the two-body collision rate. The time dependence of the cloud size for this condition is given in figure 3. This shows that the cloud does not collapse to its original extent during its evolution in the trap. We expect that this is the result of a small number of collisions. According to these data the size of the cloud in the z direction expands to about six times its initial value. From equation (3) this implies a factor of 6 reduction in the width of the momentum distribution or a factor of 36 in the effective z-direction temperature. This number in combination with equation (8) determines the beam waist at ≈ 20 μm, in a good agreement with the theoretically calculated value of ≈ 23 μm.

4. Moving center of mass

In contrast to most other works with FORTs, we also studied geometries where the centre of mass moves as a result of a change in the potential. This was achieved by offsetting the foci of the CO_2 beams from each other. In this configuration, when one of the beams was switched off, the atoms moved towards the new potential minimum located at the focus of the remaining beam. For a harmonic trap the centre of mass and internal dynamics of the atomic

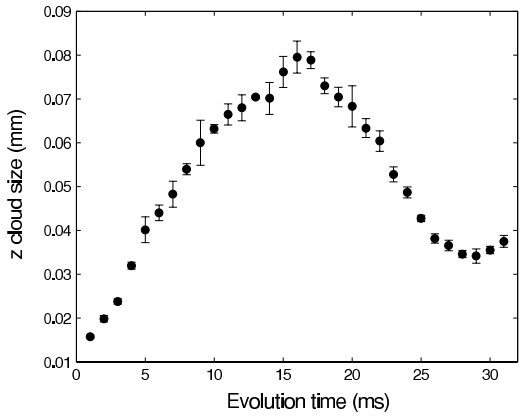

Figure 3. Evolution of the z cloud size inside the z beam for a stationary centre of mass. Two beams from a CO_2 laser crossed each other at right angles with overlapped foci. The power in the x beam was abruptly transferred to the z beam at $t = 0$ to initiate the cloud's oscillation.

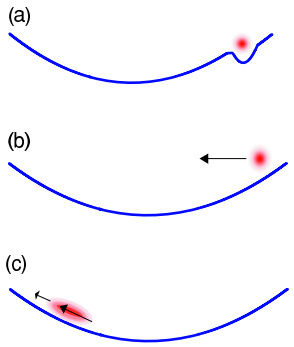

Figure 4. Schematic of the dipole potential (a) before and (b) after transferring the power of the x beam to the z beam. In (b) the centre of mass of the atomic cloud oscillates around the Gaussian focus of the remaining light. (c) Cloud size after evolving inside the z beam for approximately half a period. The difference in velocities at the two ends of the cloud gives rise to a collapse after the potential is switched off for a TOF experiment.

cloud are decoupled from one another. However, for an anharmonic trap the periodic motion of the centre of mass of the atoms couples to the internal dynamics. Figure 4 schematically displays the trapping potential before and after power is transferred to the z beam.

The observed z cloud size as a function of time for one period is presented in figure 5. As occurred in the previous section, the cloud size in this direction never shrinks to its initial value. Figure 5 also shows that the cloud undergoes a considerable increase in width by the time it reaches the focus of the z-beam at $t \approx 10$ ms. It can be seen that the cloud size increases by as much as ten times its initial value. This implies a compression in momentum spread by a similar factor and thus we expect a two order of magnitude reduction of the effective temperature in the z-direction. This is significantly more than was possible in the stationary centre of mass experiments.

Figure B.6. Journal of Physics: Page 6.

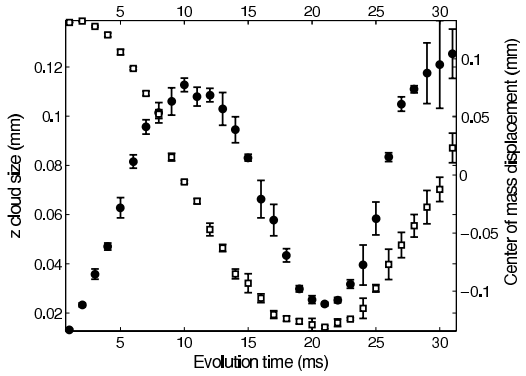

Figure 5. The cloud size (closed circles) and centre of mass position (open squares) in the z direction while evolving inside the z beam. Initially two beams from a CO_2 crossed each other at right angles with their foci displaced by $\approx$140 μm. The power in the x beam was abruptly transferred to the z beam at $t = 0$.

We also performed experiments in which the potential was switched off completely after the atoms had evolved for various times inside the z-beam. There are several features of the cloud's evolution after release from the z-beam that are worthy of note. Firstly, it is possible to tune the centre-of-mass velocity in the z-direction with high precision. This can be accomplished by changing the time span that the cloud evolves inside the z-beam before it is switched off. Such a property could be useful for quantum reflection experiments where a precise control of the impact velocity is required [23]. A second aspect of the free evolution is the observation of a collapse of the cloud in the z-direction during the first few milliseconds after the atoms are released. To observe this collapse the cloud is first allowed to evolve inside the z-beam for nearly half a period of the centre-of-mass motion. The collapse can be explained by the velocity difference between the atoms on either side of the cloud imprinted by the gradient of the trapping potential. This can be seen in figure 4(c). The exact time at which to switch the z-beam off to observe the maximum collapse is determined experimentally. This time is 16 ms for the experiment shown in figure 5. The resulting collapse or focusing can be used to transfer energy from the z to the x and y directions if the cloud has high enough densities such that the free expansion starts when the cloud is in the collisional regime. Under this condition, since at the release time the trap has become elongated in the z direction, the atoms moving along the z direction experience a larger number of collisions compared to the x and y directions and part of their z kinetic energy transfers into x and y while expanding [24]. To explore this possibility, unlike in the previous section, the evaporative cooling is carried out such that the cloud had a density of $\approx 10^{14}$ atoms cm^{-3} (this corresponds to a mean free path of 9 μm for our system). The velocity distribution should remain constant with time after the expansion makes the mean free path larger than the cloud size and the atoms reach the collisionless regime. Therefore, to determine the temperature the asymptotic expansion rate of the cloud data must be used [25] after it has reached the collisionless regime.

For comparison we have conducted another series of experiments in which the power in the CO_2 laser was switched off without transferring total power to the z beam. Figure 6(a) shows the size of the atomic cloud as a function of time after release from a crossed beam trap with 5 W of power. As can be seen, the expansion of the atoms is isotropic (x and z data overlap) and the corresponding temperature is about 3.7 (2) μK. In figure 6(b), the cloud size

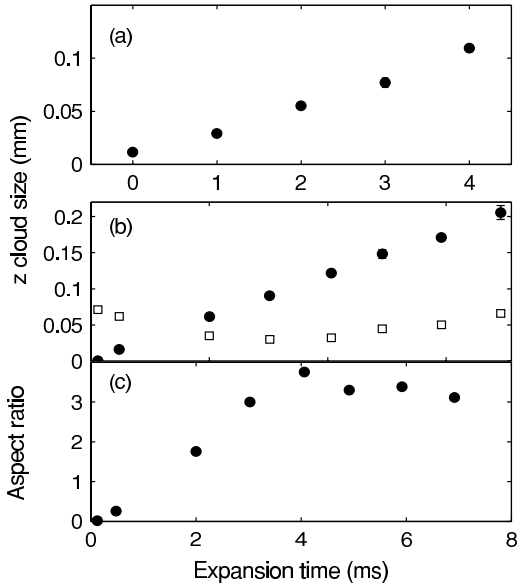

Figure 6. Experimental data showing the cloud size. The power was 5 W per CO_2 beam. The circular and square symbols represent the cloud size in the x and z directions, respectively. Part (a) shows the results after various expansion times for the case where the FORT has been directly released from the crossed beams. Note that the circle and square symbols overlap each other in this case. In (b) the x and z cloud sizes are shown for the condition where the power from the x beam was switched to the z beam 15 ms before releasing the FORT. In (c) the ratio of the x to z cloud sizes of (b) is presented.

as a function of time is given for an experiment in which the atoms were released from the crossed beam trap (off-set foci) and then allowed to evolve for 6 ms inside the z beam before all potentials were switched off and the free expansion began. The asymptotic velocity for the elongated trap extracted from the data given in figure 6(b) gives $T_z = 0.43(2)$ μK and $T_x = 4.4(2)$ μK. The higher temperature in the x direction is caused by the focusing of the cloud and the extra collisions atoms undergo in the z direction because of the compressed cloud. The ratio is $T_x/T_z = 10.2$ which is quite close to the square of the mean aspect ratio $= 3.3$ for the collisionless expansion. Figure 6(c) shows the ratio of the x to z size of the cloud at different times. Figure 7 shows the atomic cloud's image for four different times during the free expansion. Figure 7(a) shows the cloud at the crossed beam without expansion and figure 7(b) is the same cloud after 4 ms free expansion. Figure 7(c) is taken 6 ms after turning the vertical beam off and figure 7(d) is the same cloud after 4 ms of free expansion. The accurate simulation of the individual atomic trajectories for the free expansion is very time consuming because of the two-body cold collisions. In order to overcome this problem we employ the direct simulation Monte Carlo (DSMC) method which was initially developed by Bird [26] to simulate molecular gas dynamics. This method has been used for direct simulation of evaporative cooling [27] and free expansion of the cloud of atoms [24]. Using this method the behaviour of a cloud of atoms with 2 μK temperature initially displaced $0.5z_R$ from the potential minimum created by a Gaussian beam with 25 μm beam waist was simulated. Figure 8 shows the simulated momentum distribution in the z (narrow distribution) and x (broad distribution) directions after 5 ms free expansion. The initial density was taken

Figure B.8. Journal of Physics: Page 8.

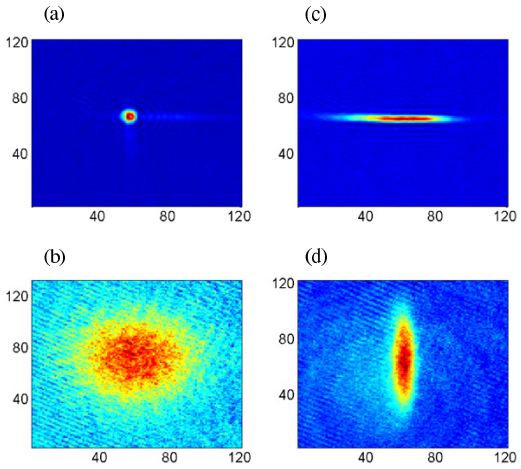

Figure 7. Images of the atomic cloud. Part (a) shows cloud at the beginning of the time of flight released from two crossed beams. In (b) the same cloud after 4 ms free expansion. (c) Released from the crossed beam FORT 6 ms after turning off the x beam and (d) is the same cloud imaged 4 ms after the x beam has been extinguished. Each pixel in the images is 6×6 μm.

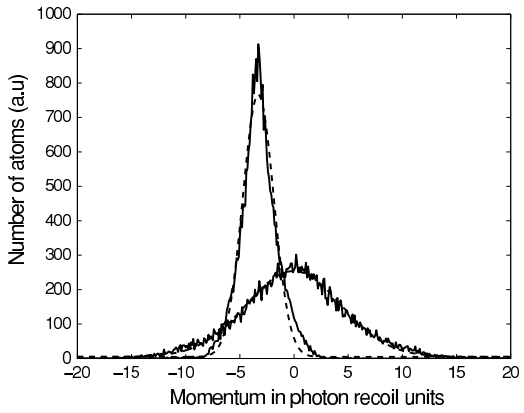

Figure 8. Simulated momentum distributions in z and x directions after 5 ms free expansion. The broken lines are the Gaussian fit to the data. The narrow and broad curves are the z and x distributions, respectively.

1.8×10^{14} atom cm^{-3}. As one can see the axial distribution deviates little from a perfect Gaussian. This has been reported previously for an expanding cloud [24].

5. Conclusion

In this paper, we have studied the effect of geometrical changes of the trap on the atomic cloud evolution. We experimented with two configurations of crossed laser beams. In the first set of experiments, the foci of two orthogonal beams were positioned to coincide. The foci of the

beams were subsequently offset for the second set of experiments. In each case, the behaviour of the cloud upon abruptly switching off the x beam was studied. In the overlapped foci experiment we observed high atomic density domains, due to the strong anharmonic trapping potential. To reach the collisionless regime the trap density was reduced by lowering the power in the beams. We observed oscillations in the axial z direction with an amplitude up to a factor of six times the original cloud size. This implies that the momentum had been reduced by a factor of 36. When the beams' foci were offset, cloud sizes as much as 10 times the initial cloud size were achieved. In this later case, we observed the atomic cloud to collapse in the z direction when released from certain positions in the trap. An energy transfer from the z to the x direction was observed for this release condition for clouds with high densities.

Considering the fact that the cloud's centre of mass gains a z velocity this system could be a useful tool in the study of quantum reflection of cold atoms from material surfaces [28–30]. Another possible avenue for further investigations would be subjecting a Bose–Einstein condensate to these potentials.

Acknowledgments

P Ahmadi was supported by an Oklahoma EPSCoR Nanonet grant and B P Timmons was supported by a NASA Space Grant Fellowship.

References

[1] Stamper-Kurn D M, Miesner H-J, Chikkatur A P, Inouye S, Stenger J and Ketterle W 1998 *Phys. Rev. Lett.* **81** 2194
[2] Stamper-Kurn D M, Miesner H-J, Inouye S, Andrews M R and Ketterle W 1998 *Phys. Rev. Lett.* **81** 500
[3] Rudy P, Ejnisman R and Bigelow N P 1997 *Phys. Rev. Lett.* **78** 4906
[4] Raithel G, Birkl G, Phillips W D and Rolston S L 1997 *Phys. Rev. Lett.* **78** 2928
[5] Janszky J and Yushin Y Y 1986 *Opt. Commun.* **59** 151
[6] Janszky J and Adam P 1989 *Phys. Rev.* A **39** 5445
[7] Aliga J, Grespo G and Proto N 1990 *Phys. Rev.* A **42** 618
[8] Lo C F 1990 *J. Phys. A: Math. Gen.* **23** 1155
[9] Agarwal G S and Kumar S A 1991 *Phys. Rev. Lett.* **67** 3665
[10] Janszky J and Yushin Y 1992 *Phys. Rev.* A **46** 6091
[11] Leibscher M and Averbukh I Sh 2002 *Phys. Rev.* A **65** 053816
[12] Balatov A, Vugmeister B, Burin A and Rabitz H 1998 *Phys. Rev.* A **58** 1346
[13] Balatov A, Vugmeister B and Rabitz H 1999 *Phys. Rev.* A **60** 4875
[14] Crompvoets Flories M H *et al* 2002 *Phys. Rev. Lett.* **89** 093004
[15] Ketterle W *et al* 2003 *Science* **301** 1513
[16] Hubert Ammann and Nelson Christensen 1997 *Phys. Rev. Lett.* **78** 2088
[17] Barrett M D, Sauer J A and Chapman M S 2001 *Phys. Rev. Lett.* **87** 010404
[18] Görlitz A, Weidemüller M, Hänsch T W and Hemmerich A 1997 *Phys. Rev. Lett.* **78** 2096
[19] Rudy R, Ejnisman R and Bigelow N P 1997 *Phys. Rev. Lett.* **78** 4906
[20] Monroe C 1997 *Nature* **388** 719
[21] Ahmadi P, Timmons B P and Summy G S 2005 *Phys. Rev.* A **72** 023411
[22] Ahmadi P, Ramareddy V and Summy G S 2005 *New J. Phys.* **5** 7
[23] Japha Y and Band Y B 2002 *J. Phys. B: At. Mol. Opt. Phys.* **35** 2383
[24] Wu H and Arimondo E 1998 *Europhys. Lett.* **43** 141
[25] Shvarchuk I *et al* 2003 *Phys. Rev.* A **68** 063603
[26] Bird G A 1994 *Molecular Gas Dynamics and the Direct Simulation of Gas Flow* (Oxford: Clarendon)
[27] Wu H and Foot C J 1996 *J. Phys. B: At. Mol. Opt. Phys.* **29** L321
[28] Anderson A *et al* 1986 *Phys. Rev.* A **34** 3513
[29] Berkhout J J *et al* 1989 *Phys. Rev. Lett.* **63** 1689
[30] Shimizu F 2001 *Phys. Rev. Lett.* **86** 987

Figure B.10. Journal of Physics: Page 10.

PHYSICAL REVIEW A **72,** 023411 (2005)

Geometrical effects in the loading of an optical atom trap

P. Ahmadi, B. P. Timmons, and G. S. Summy
Department of Physics, Oklahoma State University, Stillwater, Oklahoma 74078-3072, USA
(Received 14 March 2005; revised manuscript received 12 May 2005; published 15 August 2005)

Loading of atoms contained in a magneto-optic trap into an optical trap formed with the focused laser beam from a CO_2 laser is examined. We show that while the loading efficiency is very sensitive to the volume of the optical trap, it is insensitive to the total laser power once a certain threshold is reached. Based on these observations a time-averaged optical atom trap is realized to compensate for the small capture volume of tight traps which are required for efficient evaporative cooling. Up to a 100% increase in the trap population is observed for the time-averaged traps. We also study the effect on temperature and trap population of changing a time-averaged optical trap back to a static trap. Our results provide a basis for increasing the number of atoms in Bose-Einstein condensates produced using all-optical techniques and show that a high-power laser is not a prerequisite for such an increase.

DOI: 10.1103/PhysRevA.72.023411 PACS number(s): 32.80.Lg, 32.80.Pj

I. INTRODUCTION

The trapping of atoms using light that is far detuned to the red of an atomic resonance has been the subject of study for almost a decade now [1,2]. Recently a resurgence of interest in these far off-resonant optical traps (FORT's) has led to the all-optical production of Bose-Einstein condensates (BEC's) of rubidium [3], cesium [4], and ytterbium [5]. A FORT has been used to produce a degenerate Fermi gas of lithium [6] and has even formed the basis for the first all-optical atom laser [7]. These optical traps offer several advantages over the traditional magnetic traps that are used to produce BEC's: the trapping is not limited to a particular Zeeman substate, and the geometry of the trap can be readily adjusted. Furthermore, the tight confinement that is possible in a FORT produces high initial elastic collision rates, leading to the possibility of rapid evaporative cooling. However, the efficient loading of a FORT with atoms still remains a challenge.

Typically, in rubidium FORT experiments, a far-off-resonant laser beam from a CO_2 laser is focused into a collection of atoms that accumulate in a magneto-optical trap (MOT). Although there has been previous work on the mechanisms important in the loading of a FORT [8], there are still many aspects of this process that are not well understood. In particular the role of the FORT geometry has received scant attention. As we will see, the FORT volume plays a critical role in determining the number of atoms loaded. However, increasing this volume can lead to reductions in the density and consequently a less useful trap for evaporative cooling. We suggest a way around this problem using a time-averaged potential [9,10].

In this paper we begin by examining the background to trapping atoms by far-off-resonant laser light, giving a simple theory which allows us to understand the key parameters affecting the loading efficiency of the FORT from a MOT. We proceed to present a detailed experimental study of the loading process, looking at the effect of the FORT depth and spatial extent in Sec. III. In Sec. IV the concept of time-averaged potentials is introduced and we report the results of our initial experiments.

II. THEORETICAL MODEL

In our experiment, rubidium atoms in a MOT are exposed to a focused CO_2 laser beam. Since the wavelength of this light (10.6 μm) is far to the red of the rubidium $D2$ transition (780 nm), the interaction of the atoms with the laser light is quasielectrostatic. This produces an energy shift of the atomic ground state given by, $U=-\frac{1}{2}\alpha_g|E|^2$, where α_g is the ground-state static polarizability and $|E|^2$ is the time average of the square of the laser light's electric field. For a Gaussian laser beam propagating in the z direction this quantity can be expressed as

$$|E(x,y,z)|^2 = E_0^2 \frac{w_0^2}{w^2(z)} \exp\left(\frac{-2(x^2+y^2)}{w^2(z)}\right), \qquad (1)$$

where $w(z)=w_0[1+(z/z_R)^2]^{1/2}$. Here w_0 is the beam waist, z_R is the Rayleigh length, and E_0 is the electric field amplitude. The atoms experience a potential minimum at the focus of the laser beam and can become trapped. Unfortunately, the capture range and depth of such a trap are rather limited, so it is necessary to load the optical trap from a MOT. Clearly the efficiency of such a process is of great interest since it is highly desirable that the FORT contain as many atoms as possible. This loading process has been theoretically investigated from several different perspectives. For example, O'Hara and co-workers solved a Fokker-Planck equation (see [8] and references therein), while Kuppens *et al.* [11] used a phenomenological approach to investigate the process. In the present work we build on the simple model introduced in [12] rather than engaging in a full three-dimensional dynamical treatment of the problem. As will be seen, this straightforward approach helps us to understand the effect of the geometrical configuration on the FORT population.

We assume that the atomic cloud of the MOT has a Maxwell-Boltzman distribution and that the atoms in the dipole trap eventually come into thermal equilibrium with the MOT [12,13]. Therefore the FORT population is given by

Figure B.11. Physical Review A: Page 1.

$$N = \int nf(\mathbf{r},\mathbf{p})d\mathbf{r}d\mathbf{p}g(\epsilon), \tag{2}$$

where n is the particle density and $f(\mathbf{r},\mathbf{p})$ is the distribution function for the atoms with $\mathbf{r}$ and $\mathbf{p}$ their spatial and momentum vectors. In Eq. (2) the ratio of the density of states for the Gaussian potential created by the CO_2 laser to the density of states of the MOT potential is represented by $g(\epsilon)$, where ϵ is the energy. Atoms with energy less than the maximum potential U_0 can be trapped in the FORT, and therefore the integration is truncated over all $(\mathbf{r},\mathbf{p})$, for which

$$U(\mathbf{r}) + \frac{|\mathbf{p}|^2}{2m} > U_0, \tag{3}$$

where m is the mass of an atom. Hence the integration boundaries of $\mathbf{r}$ and $\mathbf{p}$ are coupled together through Eq. (3) and the evaluation of N involves a complicated integration. Perhaps the most critical parameter in this equation is $g(\epsilon)$ which varies between zero (for a δ-function-like potential) and one (for a very shallow FORT potential). To study Eq. (2) we assume that in the overlap region between the MOT and the FORT the particle density is constant and is equal to the MOT peak density. To further simplify the equations we also treat $g(\epsilon)$ as a constant, g_0, over the overlap region. These assumptions transform Eq. (2) into

$$\begin{aligned} N &= n_0 V_0 \frac{4g_0}{\sqrt{\pi}} \int_0^{\sqrt{q}} u^2 \exp(-u^2) du \\ &= n_0 V_0 g_0 \left(\frac{4}{\sqrt{\pi}} Erf(\sqrt{q}) - \frac{8}{\pi} \sqrt{q} e^{-q} \right), \end{aligned} \tag{4}$$

where $u = |\mathbf{p}|/\sqrt{k_B T}$ and $q = U_0/k_B T$. In Eq. (4), n_0 and V_0 are the MOT peak density and the overlap volume between the MOT and FORT, respectively. Therefore $n_0 V_0$ is the total number of atoms in the overlap region and the remainder of the parameters define the loading efficiency. The integral in Eq. (4) saturates when q approaches infinity which corresponds to an infinite well depth. In fact, evaluation of this integral shows that for $q > 4$ the FORT population is approximately independent of the value of q. Therefore we introduce the concept of a saturation power, beyond which any increase in the CO_2 laser power does not appreciably affect the FORT population. For a MOT containing ^{87}Rb atoms with a typical temperature of 0.2mK, the saturation power for a CO_2 laser beam focused to a 35-μm waist is expected to be about 25 W. To achieve a higher FORT population, increasing the overlap volume V_0 would seem to be a sensible step. However, larger V_0 leads to a shallower potential well which can reduce the intensity and hence the loading efficiency. This should not present a problem provided that the intensity in the trap remains greater than the saturation level. In this paper we will present the results from experiments in which we varied this volume in two different ways.

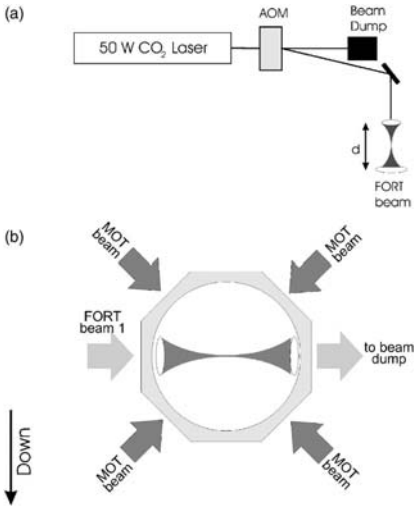

FIG. 1. Experimental schematic. The optical arrangement used to create the CO_2 FORT beams is depicted in (a). In (b) the geometry of the FORT and MOT beams with respect to the vacuum chamber is illustrated. Additional MOT beams which propagate into and out of the plane of the paper are not shown.

III. EXPERIMENT

A. Experimental setup

Our experimental apparatus consists of a stainless steel, octagonal vacuum chamber which is maintained at a pressure of approximately 5×10^{-10} torr by an ion pump. Two 2.5-cm-diam ZnSe viewports allow us to transmit the 10.6-μm light from a CO_2 laser into this chamber. The focusing arrangement for the CO_2 beam consists of a beam expander followed by a 3.75-cm-focal-length lens which is placed within the vacuum. As shown in Fig. 1(b), the beam is directed into the chamber horizontally. The light for this beam originates from a 50-W rf-excited CO_2 laser. The total laser power is controlled by passing the output light through an acousto-optic modulator (AOM). This reduces the laser power to roughly 36 W. The first order of the modulator is then directed to the vacuum chamber. The AOM is driven by an amplified 40-MHz rf signal.

The MOT is formed with a 20-G/cm magnetic field gradient and by two 2.5-cm-diam, 20-mW beams. Each beam makes three passes through the chamber and is detuned 15 MHz below the $F=2 \rightarrow F'=3$ transition of the $D2$ line. Repumping light tuned to the $F=1 \rightarrow F'=2$ transition propagates with one of the trapping beams. Normally, about 2×10^7 atoms are trapped in the MOT with this arrangement. The FORT and MOT alignment is accomplished using the method in Ref. [14]. The following procedure is used to load the FORT from the MOT. First the MOT is loaded for 25 s from the background vapor while at the same time the CO_2 laser remains switched on. Then, as a key step in efficiently loading the FORT, the repump intensity is reduced to make a

Figure B.12. Physical Review A: Page 2.

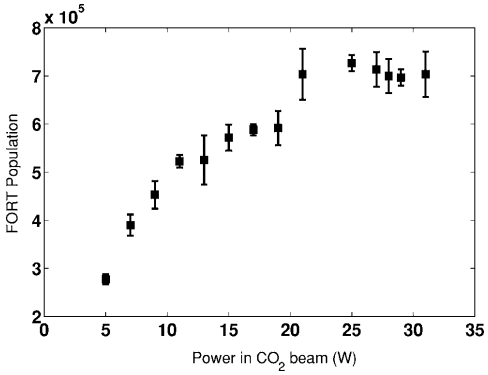

FIG. 2. Experimental data showing the number of atoms contained in the FORT vs power in the CO_2 beam. The power is focused to a 35±5 μm waist.

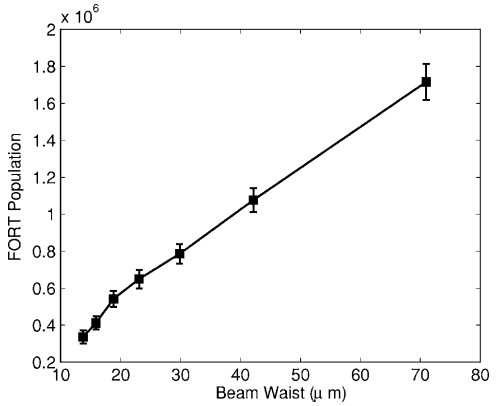

FIG. 3. Experimental data showing the number of atoms vs beam waist. The total power in CO_2 beam was 36 W.

temporal dark MOT [11,15]. This reduction in the repump power occurs 20–30 ms before switching off the MOT trapping beams. Alongside reducing the repump power, the trapping beam detuning is changed to −80 MHz for further laser cooling. This also ensures that our atoms always see the MOT beams as negatively detuned even after considering the differential ac-Stark shift between the ground and excited states [11,16,17]. Finally, the main MOT beams are extinguished and the MOT magnetic field is switched off. The earliest time that we can image the FORT is 100 ms after releasing the MOT. This ensures that any untrapped atoms have sufficient time to fall away from the FORT under the influence of gravity. Both the MOT and FORT are destructively imaged using a resonant probe laser which passes through the atom cloud and is incident on a CCD camera. The number of trapped atoms is determined by integrating the optical density across the atom cloud. When imaging the FORT, the CO_2 laser beam is switched off at least 1 ms before the image is taken to allow the cloud of atoms to expand to a size which is above the resolution of the optical system.

B. Saturation power

We investigated the sensitivity of the FORT's loading efficiency to the total power in the optical trap. We began by focusing the CO_2 laser beam into a 35±5 μm waist which coincided with the MOT center. Several experiments were performed in which the FORT was loaded using different CO_2 powers. The results of these experiments are shown in Fig. 2. These data clearly show that the number of atoms trapped in the FORT increases slowly as the power becomes larger until about the 20-W level. Above this power very little change in the number of atoms can be seen, since U_0 is much larger than the mean energy of the atomic cloud. Considering the growing interest in optical trapping and making BEC's using all optical methods, it is useful to note that if one is developing a cost-effective setup for an experiment that will be used for evaporative cooling (and consequently needs a beam waist of around 30 μm), it is unnecessary to invest in a laser with a power of more than about 50 W (25 W per beam).

C. Effect of FORT volume on FORT population

In Sec. II we theoretically considered the effect of the overlap volume on the FORT population. To experimentally observe this dependence we have performed an experiment in which the number of atoms in the FORT was measured as a function of the beam waist of the laser beam. This was achieved by passing the CO_2 laser beam through a beam expander before the vacuum chamber. The beam expander consisted of two lenses with 6.35 and 12.7 cm focal lengths whose separation could be varied. The *ABCD* matrix method [18] was used to calculate the beam waist corresponding to a specific separation of the lenses. Figure 3 shows the result of this experiment. It is clear that there is a significant reduction in the number of atoms trapped in the FORT for smaller beam waists. Note that the increase in FORT population in principle should increase with w^3. However, this is likely not observed because the saturation power also increases with w. For example, the saturation power is about 71 W at a 70-μm beam waist.

IV. TIME-AVERAGED OPTICAL TRAP

The theory of Sec. II and the experimental results of Sec. III both emphasize the sensitivity of the optical trap's population to its volume. In the following section we introduce a dynamical technique to increase this volume. This method is based on sweeping the FORT beam back and forth while it is overlapped with the MOT. Provided the motion of the beam is rapid enough, such an oscillatory trap creates a time-averaged potential with a large volume. This can capture atoms which are out of reach of a static FORT. Hence, these oscillations are expected to produce a considerable increase in the number of atoms that can be loaded.

Figure B.13. Physical Review A: Page 3.

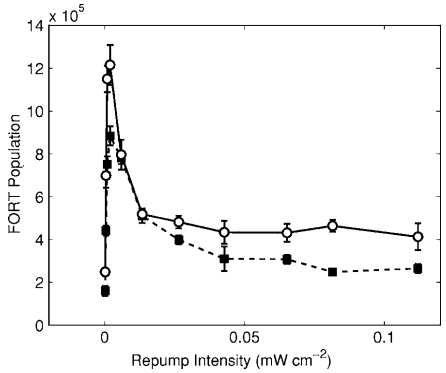

FIG. 4. Experimental data representing the number of atoms trapped in the FORT vs the intensity of the repump light during the FORT loading. The beam waist was 35±5 μm and power in the FORT beam was 36 W. The initial repump intensity used to make the MOT was 0.16 mW/cm^2. The square and open circle symbols represent the data for $\Delta\nu$=0 and 2 MHz, respectively.

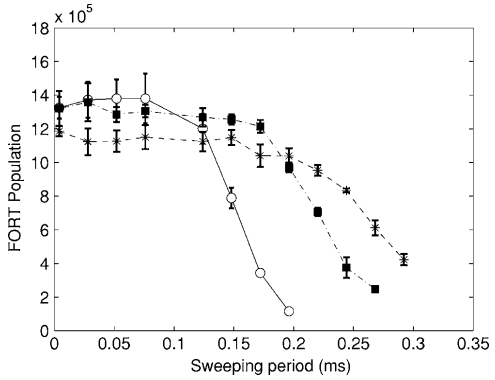

FIG. 5. Experimental data showing the number of atoms vs sweeping period. The beam waist was 35±5 μm and power in the FORT beam was 36 W. The open circle, square, and star symbols represent the data for $\Delta\nu$=1, 2, and 3 MHz, respectively.

In order to create a time-averaged potential we have used the fact that the angular position of the first order AOM beam is proportional to the rf frequency supplied to the AOM. Therefore a frequency change $\Delta\nu$ from the original 40 MHz will produce an angular deviation of the beam given by $\Delta\theta = \lambda\Delta\nu/v_a$, where λ is the wavelength of the light and v_a is the velocity of the acoustic wave in the AOM. The 40-MHz signal from the function generator is modulated with a triangle function which changes the frequency with a period T and amplitude $\Delta\nu$. Such a technique may be helpful in situations where a trap is loaded with a large volume and then adiabatically transformed to a tighter geometry for efficient evaporative cooling. It is worthy of note that even though this procedure increases the time-averaged size of the CO_2 beam on the final lens, the size of the beam focus also increases. This is opposite to what would be expected for a real increase in beam size on the final lens. In the following we study the properties of the time-averaged optical traps.

A. Repump light intensity

A well-established part of the procedure for loading an optical trap is the strong reduction in the repump power a few milliseconds before turning the MOT beams off. The reduction in the power of the repump laser, together with the energy shift induced by the electric field of the CO_2 laser, means that atoms trapped in the FORT have a significantly reduced probability of being kicked out of the FORT by the primary MOT light. We performed a series of measurements in order to study the correlation between the trap loading and repump light power for different FORT potentials. Figure 4 represents the experimental results for two different traps. Data points with a square symbol represent observations for no frequency sweep; open circles are for time-averaged traps with $\Delta\nu$=2 MHz. As expected, the population of the time-averaged potentials has a similar correlation with repump light power as a FORT, where the population maximum is reached at a specific repump power and then falls to some saturated level for higher powers. The maximum loading of the time-averaged potentials also occurs at the same repump power as for the stationary beam. This behavior was observed for all of the other sweeping frequencies which were examined.

B. Sweeping period

We now study the effect of the sweeping period on N. The experiment is carried out by changing the period, T, of the triangle modulation function applied to the AOM by the function generator. The data in Fig. 5 show N for three different $\Delta\nu$'s taken at different sweeping periods. This figure shows that N saturates at different periods for different sweeping frequencies, $\Delta\nu$. Furthermore, the FORT population rapidly falls for slow sweeping. These results indicate that the shoulder of the N curves (the edge of the saturation region) is inversely proportional to $\Delta\nu$. Such behavior can be explained by noting that the longer the period and the smaller $\Delta\nu$ becomes, the more the atoms are placed in a regime where they can adiabatically follow the motion of the laser beam. This effectively negates the time averaging effect and prevents a larger volume FORT being realized.

C. Sweeping amplitude

The number of atoms trapped in the FORT for different $\Delta\nu$ is given in Fig. 6. All data were taken with a sweeping period of T=30 μs. Since we ultimately wish to use this procedure to capture as many atoms as possible in order to do evaporative cooling, we switched to an experiment with a much smaller CO_2 beam waist. The beam waist was 20±5 μm and the CO_2 beam had 20 W power. Figure 6 shows that the FORT population reaches a maximum at $\Delta\nu$ =1 MHz with approximately a 100% improvement in the population compared to the stationary FORT. For sweeping

Figure B.14. Physical Review A: Page 4.

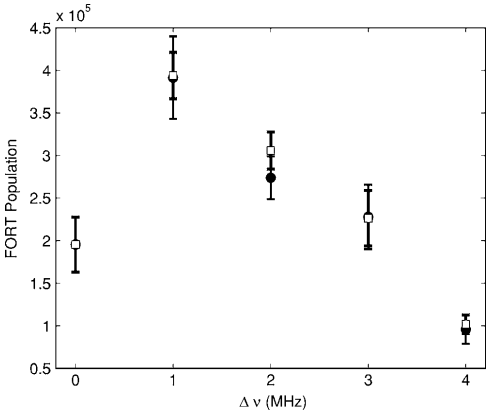

FIG. 6. Experimental data showing the number of atoms vs $\Delta\nu$. The beam waist was 20 ± 5 μm and power in the FORT beam was 20 W. The square and circle symbols are the FORT population before and after damping, respectively.

frequencies more than $\Delta\nu$=3 MHz, the number of atoms falls even below the static trap ($\Delta\nu$=0 MHz) population. This decrease is a result of the reduction of the average well depth below the saturation level, which is inversely proportional to the sweeping amplitude. Consequently only very cold atoms should stay in the trap. This has been confirmed by the experiment that will be discussed in the next section.

After switching off the MOT beams, the sweeping amplitude was linearly damped to zero over 6 ms. The FORT population at the end of the damping is shown by solid circles in Fig. 6. The data indicate that almost none of the atoms are lost from the FORT during the damping process. Effectively this damping is a realization of an acousto-optically controlled 1D zoom lens for the optical trap. We note that recently Kinoshita *et al.* have achieved an all optical BEC using a mechanical 2D zoom lens [19].

D. Trap temperature

The ballistic expansion rate of the atomic cloud was used to deduce its thermal temperature. The experiment was carried out by abruptly turning off the FORT beam. The expanding cloud was destructively imaged after several different expansion times at different sweeping amplitudes. We found that the cloud trapped by sweeping potentials with a bigger $\Delta\nu$ had a slower expansion rate, indicating that the cloud had a lower temperature. These temperatures are given by the open circles in Fig. 7 and indicate that the time-averaged traps confine colder samples of atoms. In another series of experiments the cloud temperature was measured after damping the sweeping amplitude. The final temperature for each $\Delta\nu$ is shown by square symbols in Fig. 7. The data show a rise in the cloud's temperature after damping. However, the final temperature is still lower than the temperature of atoms loaded into a static FORT.

Comparing the results of Figs. 6 and 7 we conclude that the phase-space density after damping the sweeping should

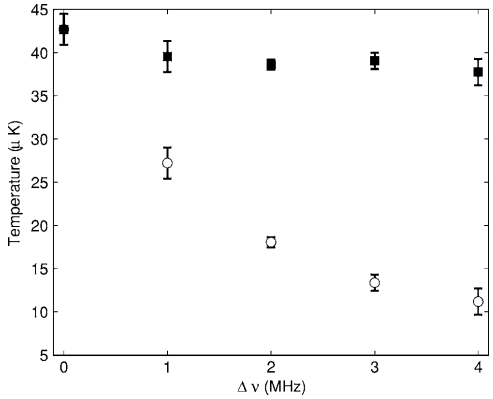

FIG. 7. Temperature of the atomic cloud vs frequency sweep. The open circle and square symbols are the cloud temperature before and after damping the sweeping amplitude.

increase at least in proportion to the number of atoms gained over the static beam case. This increase could be critically important for reaching the BEC transition.

V. CONCLUSION

In this paper we have found that the volume of an optical dipole-force trap is one of the most important factors in determining the number of atoms loaded into such a trap. To increase this volume a time-averaged optical trap was realized. Our observations show that the time-averaged traps cannot only capture more atoms compared to their static counterparts, but that the atomic clouds trapped within them have a considerably lower temperature. By slowly damping the sweeping amplitude almost all of the atoms were transported to a static trap. Although damping raised the cloud temperature, interestingly, it was always lower than the temperature of the cloud loaded directly into a static trap. Therefore, the ratio of the phase-space densities of a damped time-averaged potential and a static trap was increased by a factor given approximately by the ratio of the trap populations. We have also experimentally confirmed that above a certain laser power (which will depend upon the volume of the trap) there is very little increase in the number of atoms that can be loaded in a FORT. One possible avenue for future investigation is the realization of a crossed-beam time-averaged trap. This would allow for the loading of atoms using even larger-volume FORT's while still maintaining a tight trap for efficient evaporation. This may be important for creating Bose-Einstein condensates using rapid evaporation from a highly focused, near-resonant laser trap.

ACKNOWLEDGMENTS

P.A. was supported by an Oklahoma EPSCoR Nanonet grant, and B.P.T. was supported by a NASA Space grant. We acknowledge helpful contributions from G. Behin-Aein and V. Ramareddy.

Figure B.15. Physical Review A: Page 5.

[1] C. S. Adams, H. J. Lee, N. Davidson, M. Kasevich, and S. Chu, Phys. Rev. Lett. **74**, 3577 (1995).
[2] S. Friebel, C. D'Andrea, J. Walz, M. Weitz, and T. W. Hänsch, Phys. Rev. A **57**, R20 (1998).
[3] M. D. Barrett, J. A. Sauer, and M. S. Chapman, Phys. Rev. Lett. **87**, 010404 (2001).
[4] T. Weber *et al.*, Science **299**, 232 (2003).
[5] Y. Takasu, K. Maki, K. Komori, T. Takano, K. Honda, M. Kumakura, T. Yabuzaki, and Y. Takahashi, Phys. Rev. Lett. **91**, 040404 (2003).
[6] S. R. Granade, M. E. Gehm, K. M. O'Hara, and J. E. Thomas, Phys. Rev. Lett. **88**, 120405 (2002).
[7] G. Cennini, G. Ritt, C. Geckeler, and M. Weitz, Phys. Rev. Lett. **91**, 240408 (2003).
[8] K. M. O'Hara, S. R. Granade, M. E. Gehm, and J. E. Thomas, Phys. Rev. A **63**, 043403 (2002).
[9] N. Friedman, L. Khaykovich, R. Ozeri, and N. Davidson, Phys. Rev. A **61**, 031403(R) (2000).
[10] V. Milner, J. L. Hanssen, W. C. Campbell, and M. G. Raizen, Phys. Rev. Lett. **86**, 1514 (2001).
[11] S. J. M. Kuppens, K. L. Corwin, K. W. Miller, T. E. Chupp, and C. E. Wieman, Phys. Rev. A **62**, 013406 (2000).
[12] K. M. O'Hara, S. R. Granade, M. E. Gehm, T. A. Savard, S. Bali, C. Freed, and J. E. Thomas, Phys. Rev. Lett. **82**, 4204 (1999).
[13] H. Engler, T. Weber, M. Mudrich, R. Grimm, and M. Weidemüller, Phys. Rev. A **62**, 031402(R) (2000).
[14] P. Ahmadi, V. Ramareddy, and G. S. Summy, New J. Phys. **7**, 4 (2005).
[15] W. Ketterle, K. B. Davis, M. A. Joffe, A. Martin, and D. E. Pritchard, Phys. Rev. Lett. **70**, 2253 (1993).
[16] R. Scheunemann, F. S. Cataliotti, T. W. Häsch, and M. Weitz, J. Opt. B: Quantum Semiclassical Opt. **2**, 645 (2000).
[17] P. F. Griffin, K. J. Weatherill, S. G. MacLeod, R. M. Potvliege, and C. S. Adams, e-print physics/0504113.
[18] O. Svelto, *Principles of Lasers* (Plenum Press, New York, 1998).
[19] Toshiya Kinoshita, Trevore Wenger, and David S. Weiss, Phys. Rev. A **71**, 011602(R) (2005).

Figure B.16. Physical Review A: Page 6.

VITA

Brian P. Timmons

Candidate for the Degree of

Doctor of Philosophy

Thesis: DYNAMICS OF KICKED LASER COOLED RUBIDIUM ATOMS

Major Field: Physics

Biographical:

Personal Data:Born in Muskogee, Oklahoma on May 1, 1971, the son of Paul and Patsy Timmons.

Education:Graduated from Muskogee High School, Muskogee, Oklahoma in May 1989; received Bachelor of Science degree in Engineering Physics and Mathematics from Northeastern State University, Tahlequah, Oklahoma in May 2000. Completed the requirements for the Doctor of Philosophy degree with a major in Physics at Oklahoma State University in July 2006.

Professional Memberships:American Physical Society, Society of Physics Students

Name: Brian P. Timmons Date of Degree: July, 2006

Institution: Oklahoma State University Location: Stillwater, Oklahoma

Title of Study: DYNAMICS OF KICKED LASER COOLED RUBIDIUM ATOMS

Pages in Study: 125 Candidate for the Degree of Doctor of Philosophy

Major Field: Physics

Scope and Method of Study: The purpose of this research was to use laser cooling techniques to cool a sample of rubidium 87 atoms and pulse the cold atoms with an off-resonant standing wave of light. Among the objectives of the study was to understand the parameters needed to place the cold atoms in a quantum accelerator mode and to compare with experiments performed with cesium 133 atoms. A vacuum system and optical system were designed and built to produce a sample of laser cooled rubidium 87 atoms.

Findings and Conclusions: With the proper parameters, such as initial velocity of the atoms, time between each pulse, and gravitational potential, a linear gain in momentum of the atoms with each pulse was observed. This defined a quantum accelerator mode. Experiments performed by changing the parameters of initial atom velocity and time between each pulse are compared to those of previous experiments with cesium 133. A major difference in the two species, rubidium 87 and cesium 133, was the effect of the pulsing light's polarization. The pulsing light's polarization had little effect on the efficiency of the rubidium quantum accelerator mode. Whereas, cesium 133 requires linear polarization of the pulsed light. Higher order accelerator modes were observed and matched with theory.

ADVISOR'S APPROVAL Dr. Gil Summy